Automatic Registration of Visible-Band and SAR Satellite and Aerial Remotely Sensed Images

by

Mohamed Ahmed Hussein Ali

A thesis

presented to the University of Waterloo

in fulfilment of the

thesis requirement for the degree of

Doctor of Philosophy

in

Systems Design Engineering

Waterloo, Ontario, Canada, 2003

I hereby declare that I am the sole author of this thesis.

I authorize the University of Waterloo to lend this thesis to other institutions or individuals for the purpose of scholarly research.

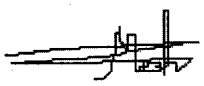

I further authorize the University of Waterloo to reproduce this thesis by photocopying or by other means, in total or in part, at the request of other institutions or individuals for the purpose of scholarly research.

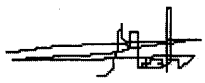

The University of Waterloo requires the signatures of all persons using or photocopying this thesis. Please sign below, and give address and date.

Abstract

Image registration is an essential and difficult task where dealing with remotely sensed images. There exist different registration techniques that work with different data. However, no algorithm is known that can accurately register different type sensor's images consistently. This thesis addresses this problem by investigating the development of a fully automatic registration system for synthetic aperture radar (SAR) and optical remotely sensed images. This novel automatic image registration method is based on the extraction and matching of common features that are visible in the image pairs. The algorithm involves the following five steps: noise removal, edge extraction, edge linking, object extraction, and object matching. The application of the proposed automatic image registration model to SAR and visible-band image pairs shows that accurate ground control points (GCPs) can be identified automatically.

Acknowledgement

Humble thanks to ALLAH THE ALMIGHTY who gave me the strength and the power so I can accomplish this work.

I wish to express my sincere thanks to my advisors professor David Clausi and Professor Ed. jernigan for their endless support, their helpful suggestion, their expert advice, their assistance and their guidance throughout the entire milestone. Their valuable comments were vital to the quality of this research. I would not have even reached this stage without their active support and encouragement.

Highly gratitude to professor Kamel, professor Basir and professor Soulis for their great support.

"Thank you" seems to be inadequate to show how very much patient and supportive my wife, Amany. I would like to deeply thank my parent for being patient and continuously giving me their special warmth and encouragement.

To my many friends and colleagues at Waterloo, I thank you all for having made these years enjoyable. I will miss you all.

Contents

List of Tables

List of Figures

Table 1: TERMS and ABBREVIATION

Term	Definition
Accuracy	Accuracy access the relationship between a set of features and a well defined reference set and is represented by the RMS error of derived set of points.
AIM	Affine Invariant Moments
ARTSO	Automatic Registration Technique for SAR and Optical images
ARVS	Automatic Registration of Visible band and SAR / InSAR images
Centroid	Centroid is the graphical mean of X and Y coordinates
ETM	Enhanced Thematic Mapper
ENL	Equivalent Number of Looks
Feature	Feature, in this thesis, is any two-dimension region that represents an object
FFT	Fast Fourier Transform
Ground control point (GCP)	A well-defined ground coordinate of a point is called ground control point (GCP) which can be used to correct the geometric distortion of an image to a reference image that has these GCPs
LoG	Laplacian of Gaussian
MHN	Most Homogeneous Neighbour
MUM	Merging Using Moments
Pixel size	Distance which can represent each pixel in an image in X and Y coordinates. This distance can be expressed as a ground distance or a distance on scanned image
RGCE	Region Growing Controlled by Edge Map
RMSE	Root Mean Square Error
SAR	Synthetic Aperture Radar
SLAR	Side Looking Aperture Radar
SNR	Signal to Noise Ratio
SPOT	(Systeme Pour l'Observation de la Terre)
TM	Thematic Mapper

Chapter 1

Introduction

1.1 Digital Image Registration

Image registration is a technique using to correct the geometric difference between two or more images, one of them is the reference image and the others are the input images of the same scene. The image registration process generally consists of four main steps. The first step is the selection of corresponding features from both reference and input images. Example of such feature are gray-level intensities, contours, edges, line intersections, and statistical features such as centroids [18]. Secondly, feature matching is obtained between the image pair to evaluate the degree of the match between the input image and the reference image. Techniques used for this purpose include in general: the cross correlation, the sum of absolute differences between the pixels, or other statistical measures. Thirdly, applying the appropriate transformation function to obtain the transformation coefficients. Such transformations are rigid (rotation, translation, and scaling); affine transformation, more

general than the rigid transformation and tolerant of complex distortion (shear and stretching); and polynomial transformation which is used when objects in the input image are curved. The last step of image registration is using the transformation coefficients to resampling the input image to the reference image grid to obtain the registered image.

In general, image registration can be defined as follows: given a pair of images M_1 and M_2 and need to find a similarity measure $S(M_1, M_2)$ to determine the optimal transformation T, such that $S(T(M_1, M_2))$ is maximized.

In case the reference image and the input image are acquired from the same sensor type, then the appropriate image registration approach is using the gray level intensities of the image pair as the features and the cross-correlation as a similarity measure. An example of this image registration approach is the registration of optical remotely sensed images of the same spectral band.

Images from different acquiring systems such as from microwaves and visible-band have different characteristics, because the image pairs come from different platforms, different sensors, different angles and different noise models. Some objects exist in one image but not in the other image and the same object appears differently in each image. This is due to the acquiring systems using different bands of the electro-magnetic spectrum. Different gray-level intensities is an image registration challenge in multi-acquisition systems in remote sensing. In dealing with this problem, point features will not be considered in registration of microwaves and visible-band images [35]. To handle image registration of microwave systems especially synthetic aperture radar (SAR) images and visible-band images, structural features should be considered.

1.2 Motivation

Image registration can be performed manually or automatically. In manual image registration the tie points between the image pair are collected using visually clear features in both images such as road intersections and corners. This tie points should be well distributed across the entire image. The manual image registration depends mainly on the accuracy of the operator and accurate registration is time consuming. In some cases, these techniques are subject to the lack of available reference data for locating the tie pints. Therefore, there is a crucial need to develop an automated technique to register multi-sensor images that deals with different-sensor remotely sensed images. Automatic image registration has been under investigation in research for a number of years [50].

The efficiency of any image registration system can be measured by the time and accuracy. This can be achieved by either reducing the number of features to be compared, or developing a more efficient registration strategy, or combining the two approaches.

While reducing the number of features is one of the important tasks that need to be solved to reduce the computational cost of the similarity measure, this is not the only main goal of our registration system. The main goal is selecting accurate corresponding points automatically to registered the image pair.

The accuracy of the registration relies on selecting accurate corresponding points and transformation function. To decide which transformation to apply on given data to produce reasonable results is very important. Different transformations and degree of these transformations exist, and need to choose between them to

obtain the suitable one to the given data.

One motivation of this research is the broad areas that use multi-sensor remotely sensed data. These applications include: data fusion (or multi-modal registration), which enables the integration of complementary information from different sensors; change detection [51][140] (or temporal registration) which is performed to monitor and measure geological, agricultural, or land cover features extracted from data obtained from one or several sensors over a certain period of time, landmark navigation which is a viewing angles registration, and a content identification [29], that search for the correspondence between two or more images. All of these examples indicate that image registration in remote sensing is an important and essential process and need to handle automatically due the large volume of data.

1.3 Thesis Objectives

The main goal of this thesis is to design and develop fast and accurate techniques for the automatic registration of microwave-based (synthetic aperture radar, (SAR) and interferometric SAR), and visible-band remotely sensed images. This is achieved by the automatic selection of the corresponding control points. To achieve this goal some other objectives were considered.

- Investigate noise removing filters to enhance the feature extraction process for the given data.
- Edge extraction algorithms is considered to obtain accurate edge map for the given data.

- Object extraction techniques is essential to develop an accurate registration to be used with different data.

1.4 Thesis Organization

The organization of the remaining chapters of this thesis is as follows. Chapter 2 presents the background for this research and various image registration approaches. The Chapter addresses the shortcomings of the existing automatic image registration systems and defines the developed methodology for the automatic registration of different sensor types images. Data properties, different preprocessing methods, and the selected data are discussed in Chapter 3. Chapter 4 exhibits different techniques of feature extraction that are applied to the data, and proposes a new technique for feature extraction. Feature matching by using evaluation functions is illustrated in Chapter 5. Chapter 6 introduces a new method for the automatic registration of high resolution aerial images and interferometric SAR data and its applications. In Chapter 7, thesis conclusions, findings and contributions are provided.

Chapter 2

Background and Proposed Work

2.1 Two-Dimensional Image Registration

Algorithms for image registration can be classified into two categories: feature-based and area-based algorithms. The feature-based approach extracts common features such as areas, curves, lines or patches from each image and uses them to perform an accurate registration. Such an approach has proved to be more suitable for problems of multi-sensor image registration [18] since most of those features do not depend on the gray-level characteristics.

The area-based registration approach uses a statistical measures to judge if one area in the input image has a correspondence in the reference image and vice-versa. The image pair is divided into small equal areas which are compared pairwise, depending on the gray level intensities of these areas [18]. The areas which have similarity are considered to be matched and from these matched areas control points can be extracted.

The determination of the corresponding control points in the images is a difficult process. At the same time it is the main step that can determine the accuracy of the registration process. Therefore, most researchers have focused on determining methods to locate control points in the images with the highest possible accuracy, as well as finding the correspondence between these control points [18]. The automation of image registration will be discussed in the next two sections.

2.2 Manual Image Registration

Manual image registration is characterized by the manual selection of the corresponding control points. In the field of remote sensing these control points are called ground control points (GCPs). The processing chain of such a registration is summarized by the following four steps: visually selecting the corresponding GCPs from each image, selecting the transformation function, determining the parameters of the transformation function by using the GCPs, and using the different resampling approaches to resample the input image to the reference image by employing the transformation coefficients.

2.2.1 Transformation Functions

Rotation, translation, and scaling represent the rigid-body transformations which are used for rigid-body registration. These transformations can be represented as follows:

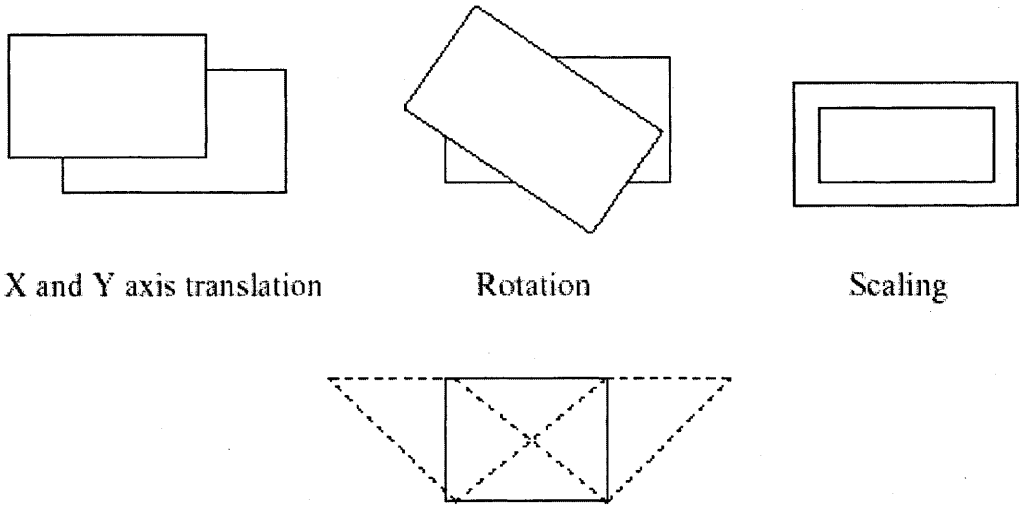

Figure 2.1: Example of image registration that finds transformations (rotation r, x and y translation) between input and reference images

$$\begin{bmatrix} u_2 \\ v_2 \end{bmatrix} = \begin{bmatrix} t_u \\ t_v \end{bmatrix} + s \begin{bmatrix} cos\theta & -sin\theta \\ sin\theta & cos\theta \end{bmatrix} \begin{bmatrix} u_1 \\ v_1 \end{bmatrix} \tag{2.1}$$

where (u_2,v_2) are the newly transformed coordinates of (u_1,v_1), t_u and t_v are the u-axis and the v-axis translations, respectively, and s is a scale factor. Translation and rotation transforms are usually caused by the different orientation of the sensor. The scaling transform is also affected by a change in the altitude of the sensor. Stretching and shearing can be the result of the sensor distortion or the viewing angle [18].

According to some a priori knowledge about the given data such as the objects in the input images used in this research are unchanged, but the images are distorted by some combination of translation, rotation, scaling and shearing. Affine

transformation is the most suitable one to apply in this case. An affine transformation is a linear coordinate transformation that consists of the elementary operations as demonstrated in Figure 2.1. These elementary operator transformations are required for registration. The general two-dimensional affine transformation can be expressed as shown in the following way:

$$\begin{bmatrix} u_2 \\ v_2 \end{bmatrix} = \begin{bmatrix} t_u \\ t_v \end{bmatrix} + \begin{bmatrix} a_{11} & a_{12} \\ a_{21} & a_{22} \end{bmatrix} \begin{bmatrix} u_1 \\ v_1 \end{bmatrix} \tag{2.2}$$

The matrix $\begin{bmatrix} a_{11} & a_{12} \\ a_{21} & a_{22} \end{bmatrix}$ can represent rotation, scale, or shear. The scale and shear for both u and v axis can be expressed as

$$\begin{bmatrix} S_u & 0 \\ 0 & S_v \end{bmatrix} \tag{2.3}$$

and

$$Shear_u = \begin{bmatrix} 1 & a \\ 0 & 1 \end{bmatrix} \qquad Shear_v = \begin{bmatrix} 1 & 0 \\ b & 1 \end{bmatrix} \tag{2.4}$$

The control points are used to identify the transformation coefficients that represent the geometric differences values between the input image and the reference image. The reference image is assumed to be geometrically correct [109] to relate the GCPs in the input image to the grid in the reference image.

2.2.2 Resampling

Finally, to obtain the registered image, a resampling operation should be performed; the input image is resampled to the reference image. A number of different resampling schemes can be used to determine the pixel value of the input image in the reference grid. These include: the nearest neighbour, bilinear interpolation and cubic convolution.

Nearest Neighbour: This method works by selecting the pixel whose centre is the nearest point located in the image. This pixel is then transferred to the corresponding grid location. This method is preferred if the new image is to be classified since the original pixel brightness values are retained, but, simply rearranged in a position to give the correct image geometry. The disadvantage of using the nearest neighbour method is that it produces a visually "choppy" effect. Although some values are duplicated by using the nearest neighbour scheme, others may be lost. This may lead to the output image having a rougher appearance than that of the unregistered input image.

Bilinear Interpolation: This approach represents the output pixel as the weighted average of the nearest four pixels. This reduces the choppy effect caused by the nearest neighbour approach. However, this method reduces the contrast and the frequency components of the image by averaging the neighbouring values.

Cubic Convolution This technique calculates the output pixel value by calculating the weighted average of the closest 16 input pixels. Cubic convolution usually gives the smoothest result, but is the most computationally expensive method.

2.3 Automatic Image Registration

Very few automatic image registration algorithms have been developed by researchers in remote sensing. An optimal solution to multi-modal automatic image registration has not been designed. This is due to the difficulties in determining the best way for generating accurate GCPs automatically.

To perform image registration automatically, it is necessary to divide the first step of manual image registration into two steps during the registration process: feature extraction and feature matching.

2.3.1 Feature Extraction

The quality of the extracted features is the key to a successful feature-based image registration technique. Therefore, the feature extraction step is pivotal to all registration systems. However, for the feature extraction process, not every single feature, which in this thesis represent a two dimension objects, needs to be extracted from each of the images. Similar objects have to be extracted from each image but it is not necessary that all extracted objects match. A high number of extracted objects is not necessary for feature-based image registration. However, to ensure the quality of the registration, the extracting of as many objects as possible is preferred and these objects should be well distributed in the image.

2.3.2 Feature Matching

The matching process takes the objects that have been extracted from the images and generates a set of GCPs. There has to be a one-to-one correspondence between

the GCPs, so that each point in the reference image can be matched with only one point in the input image, and vice-versa. The objects are matched according to some or all of their parameters, such as size, shape or radiometry. When two corresponding objects are matched, they can generate one pair of GCPs.

When the transformation function has been selected, the parameters are determined by employing the GCPs extracted from the images. The final steps of the automatic registration procedure (image transformation, and resampling) are performed automatically using standard methods.

The next section is a review of the literature of the related work.

2.4 Related Automatic Registration Work

Image registration can be divided into two classes: same-sensor types and different-sensor types. In the first class, the images differ in their relative orientation, acquiring date and/or viewing angle. In the second class, the images could also have all the differences identified in the first class beside the differences in the gray-level characteristics, such as Landsat and RADARSAT which are optical and microwave bands, and the registration of images with maps or vector data. The related image registration schemes will be discussed in this section to determine the shortcomings and drawbacks of these methods. The related method will be introduced according to the time of development.

Goshtasby et al.(1988) [56] developed a registration algorithm to register Landsat stereo images (Landsat MSS (multispectral scanner) and Landsat TM (thematic

mapper)). This technique depends on extraction of patches from each image using image segmentation. The matching process uses a clustering technique to obtain the correspondence between the patches. There is a refinement operation following the approximate matching which uses the edges of approximate matched patches. The centroid of matched patches are considered to be the GCPs. A polynomial transformation is applied to obtain the geometric difference between the input image and the reference image.

An algorithm for image registration using extracted structures (ellipticity, inclination and thinness) from input image and reference images was proposed by Rampini et al. (1990) [131]. The proposed algorithm was developed to register Landsat TM and SPOT (systeme pour l'observation de la terre) satellite images. This method begins by extracting possible objects from each image using a segmentation technique. The matching process uses a fuzzy logic algorithm to obtain the similarities between extracted objects. A 2.5 pixels root mean square error was established for the test data.

An algorithm for registering Landsat TM and SPOT images acquired at different years was proposed by Flusser and Suk (1994)[48]. The extracted features were polygons. There was a limitation or a threshold value on the polygon size, such that the too small insignificant size of the polygons were not counted in the matching process. The algorithm uses affine invariant moments (AIMs) to match these polygons. Among the matched polygons, the best three matches are used for generating the control points. The affine transformation is applied using the

generated control points to obtain the transformation coefficients. The input image is resampled using these transformation coefficients to obtain the registered image.

To register two visible-band SPOT images, Abbasi-Dezfouli and Freeman (1994) [1] utilized polygons as matching features. The matched polygons were approximately having the same gray levels. The control points were collected from the significant points on matched polygon contours. The accuracy of collected control points were low due to the difference in the contours shape of the same polygon in the image pair. The matching method was the correlation between the polygons gray level intensities.

Manjunath and Mitra (1995) [86] proposed an algorithm for registering visible-band images (Landsat and SPOT images) as well as registering SAR and visible-band images (Seasat SAR and Landsat). In the first case the extracted features to be matched were the boundaries of the polygonal objects and curves. For closed boundaries, the matching process used invariant moments and chain coding, while for curves, significant points such as corners were used for the matching. The control points were generalized from the centroid of closed polygons and curves's significant points. The affine transformation is applied to obtain the registered image. In the second case, due to the difficulty they found in detecting contours or edges from the SAR images, manual selected control points and assistance from the corresponding optical data are used. The matching and registration followed the same procedure as before.

Li and Zhou [81] developed a feature based technique for registering visual/IR sensor image. The developed technique extracts the image contours using wavelet. For each contour, an interest score is computed for all points on the contour. The contour points with high interest scores are selected. The matching process is carried onto two parts:initial matching and refined matching. The matching process mainly depends on point matching using normalized correlation function. While this approach is efficient with the given data, it has some limitations such as large rotation with significant scaling is a problem and the rotation should be compensated first. Also, there several adjustable parameters which reduce the degree of automation. The reported matching root mean square error was 1.12 pixels.

Morgado and Dowman (1997) [92] developed a technique to register aerial photographs to a map using polygons. From the map and the optical image, polygonal objects are extracted. The geometric attributes of each polygon are determined. The registration process is carried out in two steps referred to as coarse and refine registration. The coarse registration was performed by polygon attributes comparison and the refine process used edge points comparison using dynamic programming. The affine transformation is used to obtain the transformation coefficient The final stage of registration which is the resampling was carried to obtain the registered image .

Dai and Khorram (1999) [33] proposed an approach for registering two visible-band images (Landsat TM). The algorithm depends on extracting and matching the common features from both input and reference images. The algorithm is most

likely as the one developed in [48]. Closed boundaries were extracted using a segmentation technique based on LoG (Laplacian of Gaussian) [53] edge detector. The false and true closed contours are extracted using the LoG operator for segmentation. An edge refinement stage was added to detect contours. The matching process was carried out in two steps. The first step was applying the Hu invariant moments (IMs) [68] for establishing the first matching by comparing the IMs values of extracted contours. Next, chain code is applied on the matched boundaries from the first step to obtain the best match. The centroid of the three most robust matches are considered the GCPs. Applying the affine transformation, the registered image was obtained.

A registration technique for SAR and SPOT image pair was introduced by Paul Dare et al. [34] [35]. The registration operation can be summarized as follows. First, the two images should be approximately registered by selecting manual control points. The registration technique depends on extracting and matching the common patches in both images. The patches were extracted by using a combination of segmentation techniques of an existing software package called N. A. software [21]. A modified cost function was proposed for patch matching. The centroids of matched patches were considered as the ground control points. A refinement step is used to enhance the matching accuracy. This refinement step matches the edge points of the matched patches contours to increase the number of ground control points. Also to increase the number of correct matching, multiple of feature extraction techniques were used.

This developed technique is deeply considered the problem of registering SAR

and optical remotely sensed images. However, there are some comments such as the patch extraction process is performed in two stages First, set the segmentation parameters manually by trial and error until geting the best extracted patch result. Second, for each used segmentation technique a range of segmentation parameters distributed around the values which were set to produce the best batch extraction results were selected. Different combinations of parameter values of different patch extraction algorithms were performed to measure the maximum number of corrected matches. From these different parameters combinations, the one that produce maximum number of corrected matching are obtained automatically. This method proved that it is time consuming and can be applicable if the applied segmentation algorithm has only one parameter to be selected. For the given data a 1.5 pixels root mean square error has been achieved.

From this review, a comparison between these various registration methods can be obtained based on the following information:

- Images under registration were from the same sensor or from different sensors.
- Type of sensors used for experiments.
- Restrictions assumed between the image pair.
- Type of feature extracted from the image pair.
- Matching technique used.
- Transformation function used to determine the geometric difference between the image pair.

Table 2.1: Comparison Between Related Image registration Algorithms (a)

Reference	Extracted feature	Transformation function	Matching function
Rampini et al.(1990)	Patch	Polynomial	Structural matching
Flusser and Suk (1994)	Closed boundary	Affine	Cost function based on shape similarity
Abbasi-Dezfouli et al.(1994)	Polygon	Cross-correlation	Shape similarities
Manjunath and Mitra (1995)	-Closed boundary -Salient contours	Affine	-Chain code correlation -Shape similarity
Li and Zhou (1996)	Points on contour	Affine/polynomial	Normalized correlation
Morgado and Dowman (1997)	Polygon	Affine	Cost function based on shape similarities
Dai and Khorram (1999)	Closed boundary	Affine	Affine invariant moments comparison
Paul Dare et al. (2000)	Patch	Affine	Cost function based on shape similarities

- Shortcomings observed from the registration method.

Tables 2.1 and 2.2 demonstrate a comparison between the reviewed registration methods based on the previous points. It can be recognized that from this review that much more work is done on image registration of the same type of sensor images such as LANDSAT and SPOT, than on the different sensor images such as visible-band and SAR.

The following shortcomings could be found in the reviewed algorithms:

- The research area of automatic registration of microwave and visible-band

Table 2.2: Comparison Between Related Image registration Algorithms (b)

Reference	Image-pair	Major shortcoming(s)
Goshtasby) et al. (1988	Two Landsat (TM)	Only images with very well defined patches are used
Rampini et al. (1990)	Landsat (TM) and SPOT	Mainly depend on expert's intervention
Flusser and Suk (1994)	Landsat(TM) and SPOT	Only images with very well defined patches are used
Abbasi-Dezfouli et al.(1994)	Two SPOT	Mainly depends on gray level comparison
Manjunath and Mitra (1995)	-Landsat (TM) and SPOT -SAR and Landsat	Works only if the extracted objects have very well defined closed contours
Li and Zhou (1996)	SPOT and IR	-Large rotation limitation -Tested only on visual/IR data -Refinement step needed -Several adjustable parameters
Morgado and Dowman (1997)	Aerial photo and map	-Complex to understand -Approximate alignment is needed first(not more 5 pixels) -Too slow
Dai and Khorram (1999)	Two Landsat (TM)	Can be used only with visible band images
Paul Dare et al. (2000)	SAR and SPOT	-Approximate alignment first using manual GCPs -Patch extraction process has two stages -Refinement step is necessary

images is not addressed very well, since most of existing algorithms deal with the registration of visible-band images.

- Some algorithms use manual selection of GCPs for first approximate alignment.
- Noise reduction is not considered in most of the reviewed method since the images come from visible-band which have low noise compared to SAR images.
- The feature extraction procedure mainly using segmentation techniques based on the gray level intensities to extract the objects from the image pairs. This cannot be applied to SAR and visible-band images registration due to the difference in the gray level characteristics of the image pairs.
- Some algorithms use segmentation techniques that are based on homogeneous regions which can not be applied to SAR images due to the noise which makes extraction of accurate boundaries very difficult and not accurate.

From this discussion, it is not clear that any of these registration methods can produce reliable results when applied to images acquired from RADARSAT SAR and Landsat.

The principle of image registration with regard to remote sensing have been reviewed. Also, the classification of different image registration techniques has been introduced. The problems associated with the automatic registration of different types of sensors have been investigated, and demonstrate the need for automatic registration systems that can tackle these problems. The reviewing of related registration work has indicated that only a few researchers have addressed the problem

of the automatic registration of SAR and visible-band remotely sensed images.

2.5 Problem Statement and Proposed Techniques

The techniques for automated multi-sensor image registration are still in their infancy. The SAR and visible-band images of the same scene appear to be quite different. These differences may occur because of the characteristics of the sensors (stretching and shearing) or their positions (the translation, rotation, and scaling of the scenes).

As mentioned in Section 2.4, few researchers have addressed the automatic image registration of visible-band and SAR images, but cannot attain full automation. In this thesis, two automatic image registration systems are proposed for visible-band and SAR images to overcome some of the drawbacks of existing models. The domains of the images under consideration are visible-band images and SAR images obtained from either satellite or aerial platforms; however, the proposed technique is also suitable for other types of images.

The new methods are based on the extraction and matching of common features that are visible in both images. The first technique is an automatic registration technique for SAR and optical remotely sensed images (ARTSO) that depends on the extraction of common polygons from both images, which are often found in the remotely sensed images. The second technique is the automatic registration of high resolution interferometric SAR (InSAR) or SAR images and high resolution visible-band aerial images (ARVS) by using affine invariant moments (AIMs) . This ARVS technique is developed to promote the ARTSO technique for covering most

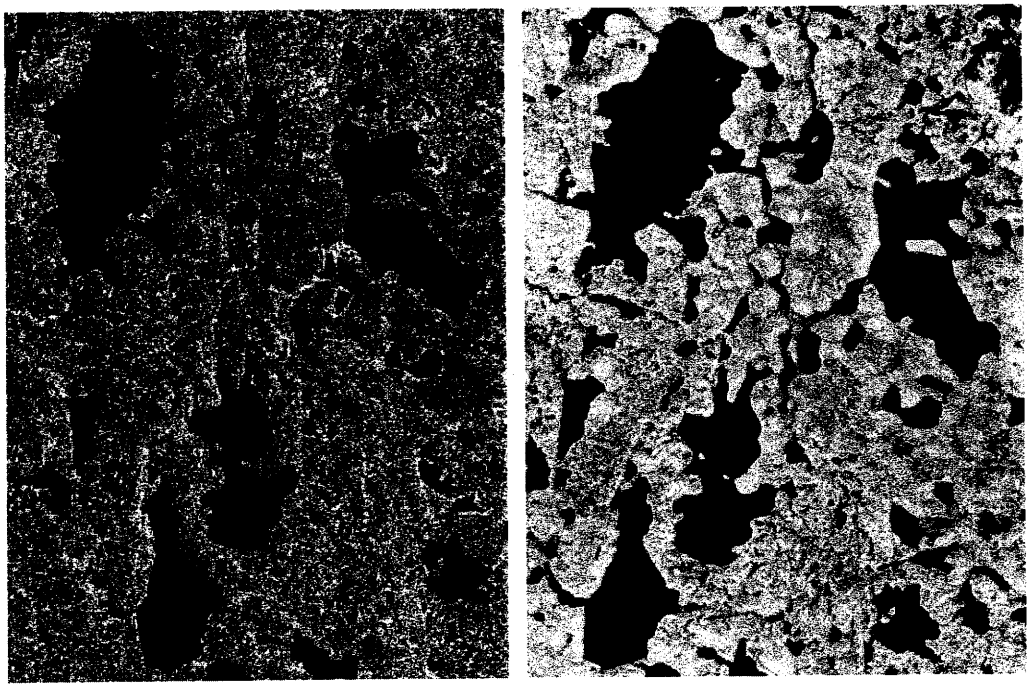

(a) RADARSAT image (b)Landsat image

Figure 2.2: SAR and optical images of the same scene appear quite different

real cases.

2.6 New Automatic Registration Technique for SAR and Optical Remote Sensing Images (ARTSO)

The newly developed automatic registration for SAR and visible-band remotely sensed images (ARTSO) has several steps. Each step of the ARTSO technique needs to be thoroughly examined. Figure 2.3 illustrates the proposed ARTSO model. Developing the ARTSO algorithm involves investigating the following processing steps:

- Noise removal: The main objective of this step is to reduce noise characteristics without significantly modifying the pertinent features. For a number of reasons, noise removal in SAR imagery is different from that of optical imagery, motivating different approaches for each. A number of existing standard algorithms and three modifications are compared.

- Edge extraction: A number of different edge extraction schemes are considered. The edge detector should provide consistent identification of high contrast boundaries. A modified Canny edge detector is considered to be suitable.

- Edge linking: Due to the incomplete contours within the edge map, edge linking is performed.

- Region growing: Region growing is performed to create the necessary ob-

jects. Region growing is a method proposed to accomplish accurate region boundaries. This method requires the following steps: the elimination of insignificant objects, obtaining the minimum homogeneous region within the closed contours, and finally, growing the region within the closed contours. This method is called region growing controlled by edge map (RGCE).

- Object matching: This is achieved by using the differences in the attributes of the objects in SAR and visible-band images to determine an evaluation function which is minimized to give the best match. The evaluation function is used for comparing an object in one image to all the objects in the other image to find the best match. This function is also used to remove multiple matches.

The centroids (centre of gravity) of the matched objects are considered to be the GCPs. The centroid of polygon as GCP can achieve sub-pixel accuracy. However, if two images suffering from locally significant geometric distortion, then the centroid of corresponding polygons may not correspond to each other and in this case they can not selected as control points. An affine transformation, by using the automated selected GCPs and resampling, is applied to obtain the registered image.

2.7 Discussion

The image registration challenges, especially if automated, have been introduced as a motivation for this research. This main objective of the research is to develop an automatic image registration technique that can be applied to SAR and visible-band remotely senses images. To satisfy this objective, many aspects such as feature

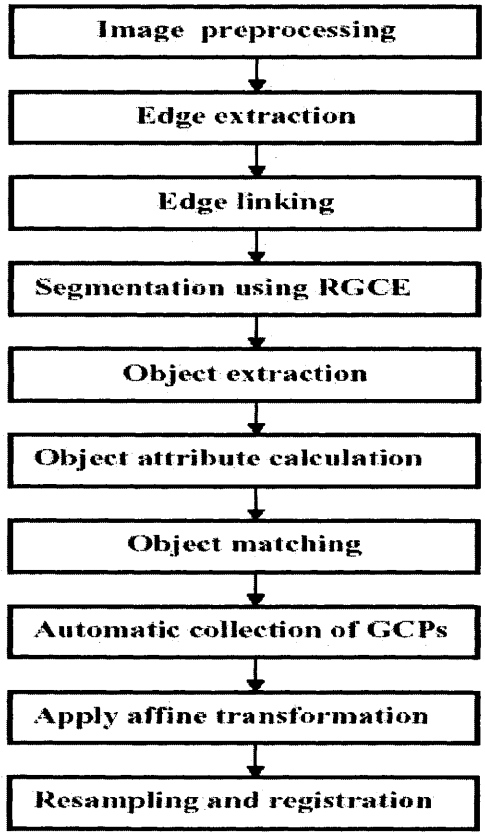

Figure 2.3: Automatic registration technique for SAR and optical remote sensing images ARTSO algorithm

extraction and feature matching should be examined. The proposed model ARTSO objectives have been presented. Then next chapter will introduce SAR and visible-band data acquisition systems and their preprocessing.

Chapter 3

Acquired Data and Preprocessing

3.1 Introduction

Knowing how the images are generated is important for accurate processing. Image formation, for example, is essential to understand the geometric properties of the image and, accordingly, apply geometric correction algorithms. Also, details of the imaging system are necessary to determine the radiometric properties of an image. Without knowing the imaging system information, it becomes more difficult to understand the exact geometric and radiometric properties of an image such as the objects boundaries and the different noise models.

This chapter describes the systems that are used to acquire the data used throughout this study. These systems include: the SAR sensor onboard the RADARSAT satellite as well as thematic mapper (TM) and enhanced thematic mapper (ETM) on board the Landsat platform. Also, the pre-processing approaches for noise removal and enhancement are presented along with examples and applications [91].

3.2 SAR Data Properties

3.2.1 Basic Concepts and Principles of SAR

Microwave sensors are either active or passive. An active radar system transmits a microwave beam and receives the wave reflected by the objects, while the passive sensors just measure the microwave radiation emitted by objects. The SAR is an active sensor that is not dependent on natural illumination and is capable of penetrating cloud cover. This gives SAR a unique all weather, day and night capability which has definite advantages over other sensors [66]. The SAR system can be mounted on aircraft or satellite. examples of civilian SAR are Seasat and one mounted on the RADARSAT platform.

The SAR is a valuable source of data. However, it has a very important phenomenon that makes its image signal to noise ratio low, namely, speckle noise. This speckle makes the objects harder to resolve in SAR images than in visible-band images [75]. A comprehensive description of the theory of radar imaging is beyond the scope of this thesis, however a brief description of how radar imaging works follows.

As shown in Figure 3.1, the platform is carrying a SAR sensor above the ground and perpendicular to the ground in a point called the "nadir". SAR transmits a beam of microwaves towards a certain area in the ground. The width of this area is called the "range". A narrow range cause fine resolution and vice-versa. The time elapsed between the transmitted beam and received echoes is used for measuring the distance between the platform and the objects. The azimuth range also is one of the important factors in a SAR imaging system. The azimuth dimension is

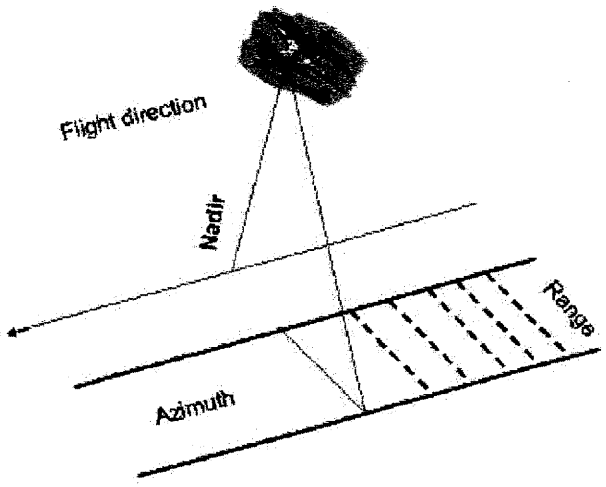

Figure 3.1: Radar imaging geometry

perpendicular to the range and parallel to the flight direction.

3.2.2 SAR Resolution

The SAR system is a kind of side looking airborne radar (SLAR). To better understand the resolution concept in the SAR imaging system, it is helpful to begin with the SLAR system. For SLAR the individual backscattered pulse of radiation consists of a number of echoes that are reflected from different objects to the antenna. Three different resolutions are determined from SLAR: slant range resolution, ground resolution, and azimuth resolution [66] .

Slant range resolution

The ability to distinguish between objects in the cross-track direction is known as the range resolution. Two objects can be resolved if the pulse of radiation backscattered from each object is received at the antenna separately. This is called slant

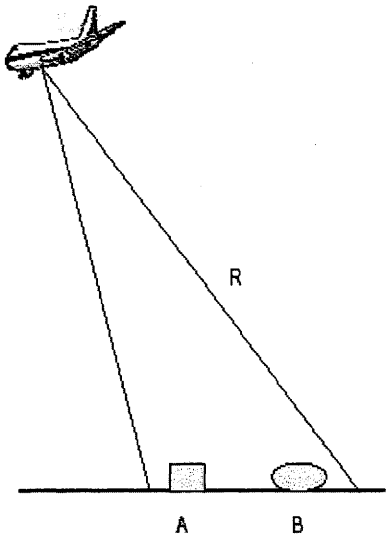

Figure 3.2: Slant resolution

resolution, If there are two objects A and B, (Figure 3.2), the slant range resolution can be determined as follows. The round trip time to object A is $T = 2R/c$, and the round trip time to object B is $T + \triangle t = 2(R + \triangle r)/c$. The time difference is $\triangle t = 2\triangle r/c$, such that $\triangle t$ must be greater than the pulse duration τ for resolution or $\tau < 2\triangle r/c$. Then the slant range resolution is defined as:

$$\triangle r = \frac{c\tau}{2} \tag{3.1}$$

where c is the speed of the light.

Ground resolution

In terms of ground range, the ground range resolution is dependent on the look

angle of the sensor θ. The ground range resolution $\triangle g$, can be expressed as:

$$\triangle g = \frac{\triangle r}{2 \sin \theta} \tag{3.2}$$

Azimuth resolution

The azimuth resolution of the SLAR sensor depends on the beam-width of the antenna and the ground range, (Figure 3.3). Two objects A and B can be resolved if their separation is greater than the beam-width β. Thus, azimuth resolution can be expressed as:

$$\triangle z = R\beta \tag{3.3}$$

where R is the slant range. The beam-width is proportional to the wavelength of the radiation λ and inversely proportional to the antenna length l.

$$\beta = \frac{\lambda}{l} \tag{3.4}$$

Then:

$$\triangle z = \frac{R\lambda}{l} \tag{3.5}$$

Therefore, high azimuth resolution can be achieved with a large antenna. While a large physical antenna is not realistic, a solution can be achieved with a synthesized length of the antenna. SAR system synthesizes the size of antenna, such that

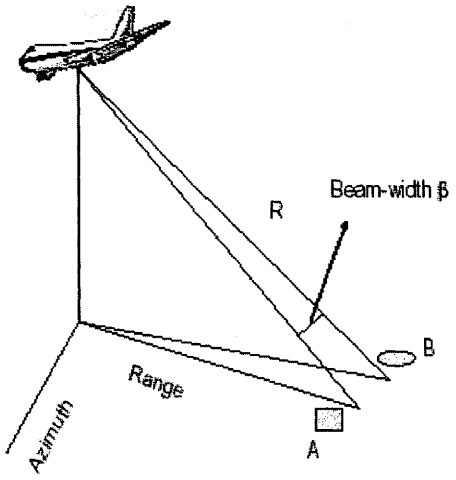

Figure 3.3: Azimuth resolution

SAR azimuth resolution only depends on its length as [130]:

$$\triangle z_{SAR} = \frac{l}{2} \tag{3.6}$$

Very small resolution cells can be achieved with the azimuth resolution because it is directly proportional to the length of the actual antenna [130]. However, it is very difficult to get sufficient power from very small antenna.

3.3 Interferometric SAR

An interferometric SAR (InSAR) image is a combination of two SAR images for the same scene acquired by two different antennas separated in the range dimension by a small distance [88]. These two antennas can be mounted on the same platform

or the data can be acquired by the same sensor with two different passes. The phase difference between the two backscattered returns is used for calculating the path length. The information of the antennas position with respect to the ground helps for determining the location of the resolution cell and its elevation. The phase difference between the adjacent cells is in the form of an interferogram. The interferogram contours represent the elevation variations. This contour information can be used for three-dimensional reconstructions of terrain. Each InSAR pixel is a combination of two components: amplitude and phase [88]. The amplitude is the product of the two SAR amplitudes. Figure 3.4 shows the geometry of the InSAR system. The InSAR amplitude component is distorted by speckle multiplicative noise, while the phase component is distorted by additive noise [79]. From the complex InSAR signal, the real A and imaginary J contain information about the amplitude D and the phase θ. These real and imaginary parts can be expressed as follows:

$\theta = arctan\frac{J}{A}$

$D = \sqrt{J^2 + A^2}$

Three main techniques are used for acquiring data for InSAR. These techniques are across-track, along-track and repeat-pass interferometry. Across-track and along-track use two physical antennas for acquiring the data, while the repeat-track technique uses one antenna with two passes. InSAR has different important applications, such as topographic mapping, digital elevation models and monitoring, for example, ocean currents.

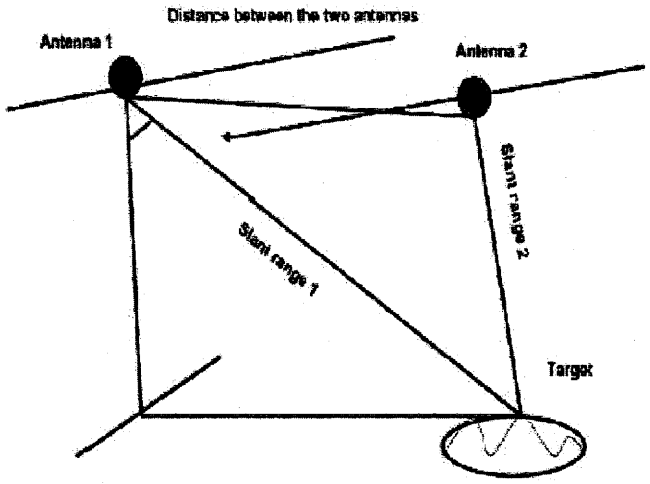

Figure 3.4: Interferometric SAR imaging geometry

3.4 Sources of Geometric Distortions

SAR imagery displays different geometric distortions. The three main geometric distortions are layover, foreshortening, and shadow,(Figure 3.5). Layover occurs when high geographic target such as mountains have steep faces and captured with different slant ranges. As a result, the SAR pulse reaches the top of the target before the base. Then the backscatter from the top returns to the antenna prior to that from the base of the feature. As a consequence the feature will appear in the image leaning towards the position of the sensor.

Foreshortening occurs when slopes of the steep faces of the high geometric target are long and gradual, the pulse reaches the base *ab* of the target prior to the top *c* and the distance between two points is mapped shorter in the image and the affected area on the image appears brighter.

Table 3.1: RADARSAT SAR Characteristics

Frequency	5.3 GHz C-band
RF Band Width	11.6, 17.3 or 30.0 MHz
Wavelength	56 mm
Incidence Angle	10 - 59 deg
Ground Resolution	10 - 100 metres
Swath Width	50 - 500 km

Shadow in radar means no backscattered information is received. The shadow areas appear as black regions on the image. The length of the shadow depends on its position in range direction. Shadow occurs where a target blocks the emitted pulse, resulting in the loss of information behind that target . Therefore, the shadow in far range is longer than in the near range.

3.5 The RADARSAT Satellite

RADARSAT is an advanced Earth observation satellite. It is used to observe Earth and the planet's natural resources. RADARSAT uses SAR as an active microwave sensor as described in Section 3.2. The SAR sensor operates with a 5.6 cm wavelength (C-band) with an HH polarization (horizontal transmit and horizontal receive). The RADARSAT uses different viewing angles that allow a wide range of applications. RADARSAT imaging has several modes include Standard,Wide, Fine, ScanSAR (narrow and wide), and Extended Beam (high and low incidence angles). The RADARSAT SAR characteristics are summarized in Table 3.1; the RADARSAT beam modes are illustrated in Figure 3.6.

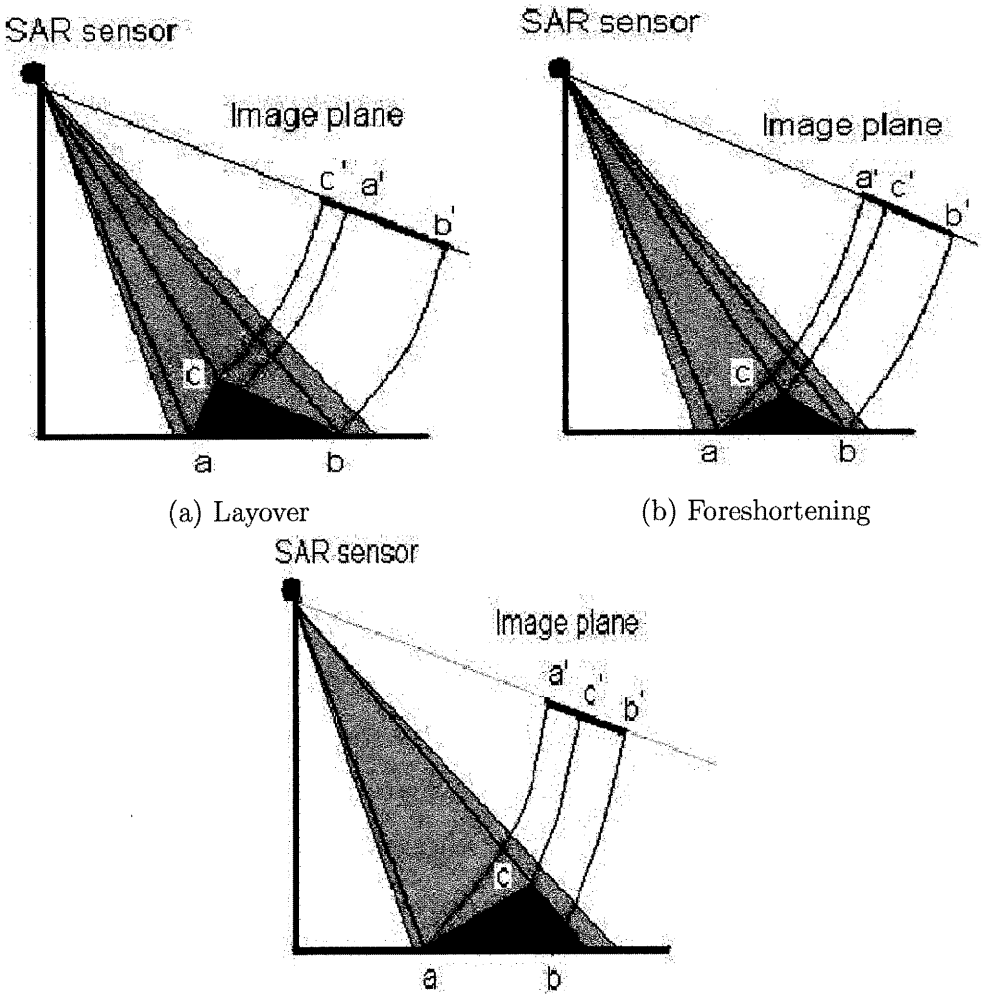

(a) Layover

(b) Foreshortening

(c) Shadowing

Figure 3.5: SAR geometric distortions [70]

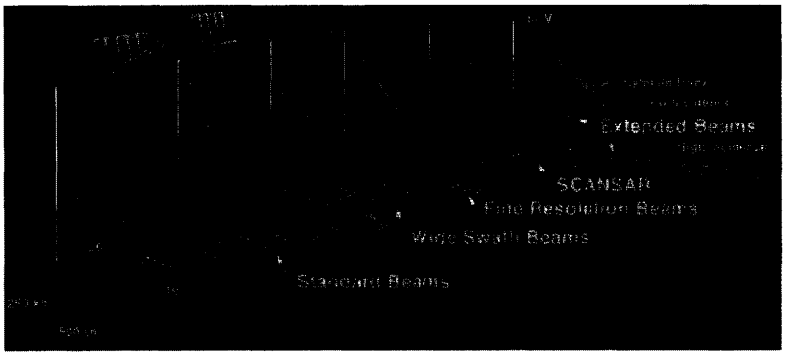

Figure 3.6: The RADARSAT beam modes [22]

3.6 Acquisition of Landsat Data

Since 1972, the United States of America has launched six Landsat missions. The main objective was to provide high resolution multispectral images of the earth's surface. Over nearly a 30 years, Landsat satellites have provided a huge amount of information that has been used in a wide variety of applications.

Landsat 7, was launched in April 1999. Landsat 7 is placed in a near-polar orbit at altitude of around 700km. It has a revisit period of 16 days. What makes this particular satellite interesting is its Enhanced Thematic Mapper Plus (ETM+) instrument. The ETM+ instrument has a high resolution thermal band of 60 metres. Bands 1 to 5 and band 7 have 30 metre resolution. It has also a panchromatic band with 15 meter resolution.

The ETM+ instrument has a set of sensors that detect earth scene radiation in three specific bands; Visible and Near Infrared (bands 1, 2, 3, 4, and 8), Short Wavelength Infrared (bands 5 and 7), and Thermal Long Wavelength Infrared (band 6). The spectral ranges for each band can be found in Table 3.2 [96]. Figure 3.7

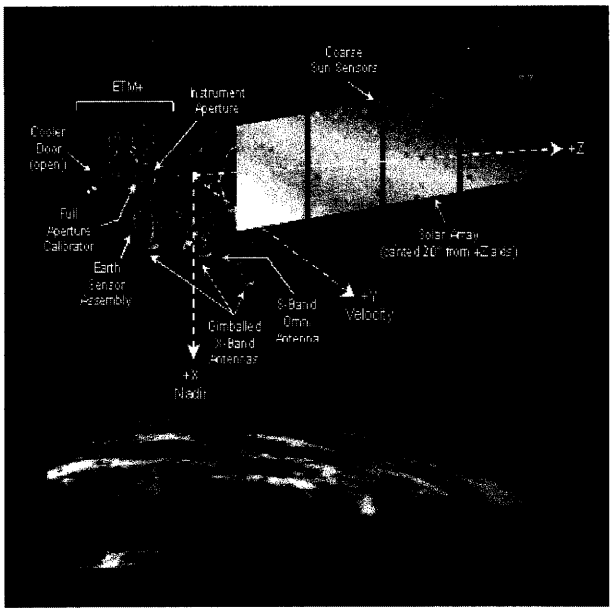

Figure 3.7: The diagram of Landsat7 satellite [96]

shows a diagram of the Landsat 7 satellite.

The Landsat 7 Enhanced Thematic Mapper (ETM) provides information on the Earth's surface in the visible, near, middle, and thermal infrared regions of the electromagnetic spectrum.

The geometric correction for the Landsat images is done using parametric models not polynomial method since the later method does not correct distortions that are introduced during image acquisition. The polynomial method also does not take into account distortions caused by terrain relief . The polynomial method requires several ground control points (GCPs), and only corrects locally around these GCPs [96].

Table 3.2: Landsat TM and ETM Bands

Channel	Wavelength Range (μm)	Resolution	Application
TM1	0.45 - 0.52 (blue)	30m	soil, vegetation and urban
TM2	0.52 - 0.60 (green	30m	green vegetation mapping
TM3	0.63 - 0.69 (red)	30m	vegetated vs. non-vegetated
TM4	0.76 - 0.90 (near IR)	30m	identification of plant/vegetation types
TM5	1.55 - 1.75 (short wave IR)	30m	sensitive to moisture in soil and vegetation
TM6	10.4 - 12.5 (thermal IR)	60m	vegetation stress and soil moisture discrimination
TM7	2.08 - 2.35 (Middle IR)	30m	Thermal mapping
TM8	0.52 - 0.90 (Green, Visible red, Near IR)	15m	Urban change studies. Panchromatic

3.7 Study Area

This research uses different types of images: RADARSAT, Landsat, aerial InSAR, and aerial photo images.

There are two study areas that have been chosen for this research. The first area is Kitimeot, Nunavut, Canada, and the second study area is Hilands Ranch, Colorado, USA.

3.7.1 Landsat Data

The visible-band satellite data used in this thesis was acquired by Landsat 7 panchromatic band and the acquisition date was August 2001. The Landsat image has 15 metre resolution panchromatic band. The set of images covers the areas of Kitimeot, Nunavut, Canada. The complete information about the full scene data is

Table 3.3: Landsat Full Scene Image

Geographical area	Kitimeot, Nunavut, Canada
Scene acquired time	August 04 2001
Number of image lines	10201
Number of image pixels	9521
Pixel spacing	15.500 m
Earth model	UTM 12
Upper left	43777.000 E 739628.000 N
Lower right	692797.000 E 7154603.00 N

given in Table 3.3. An example of one of the Landsat 7 panchromatic band images used in this study, reduced in size, is given in Figure 3.8.

3.7.2 SAR Data

The SAR data that is used was acquired by RADARSAT standard mode and the acquisition date was August 2000. The images resolution is 12.5 metre. The set of images covers the same area as Landsat. The full image has 8502 x 8991 pixels. Four full resolution SAR images cover Kitimeot, Nunavut, Canada area and an example of one of these images, reduced in size, is shown in Figure 3.9 and the complete data information is given in Table 3.4.

3.7.3 Aerial InSAR and Visible-Band Data

The aerial and InSAR images used for this research are provided by Intermap Technologies Corp. using STAR-3i airborne (InSAR) system mounted in a LearJet 36A aircraft . The set of images covers the areas of Highlands Ranch. The aerial photo image is a one metre resolution with full size of 3772 x 3010 pixels. The aerial

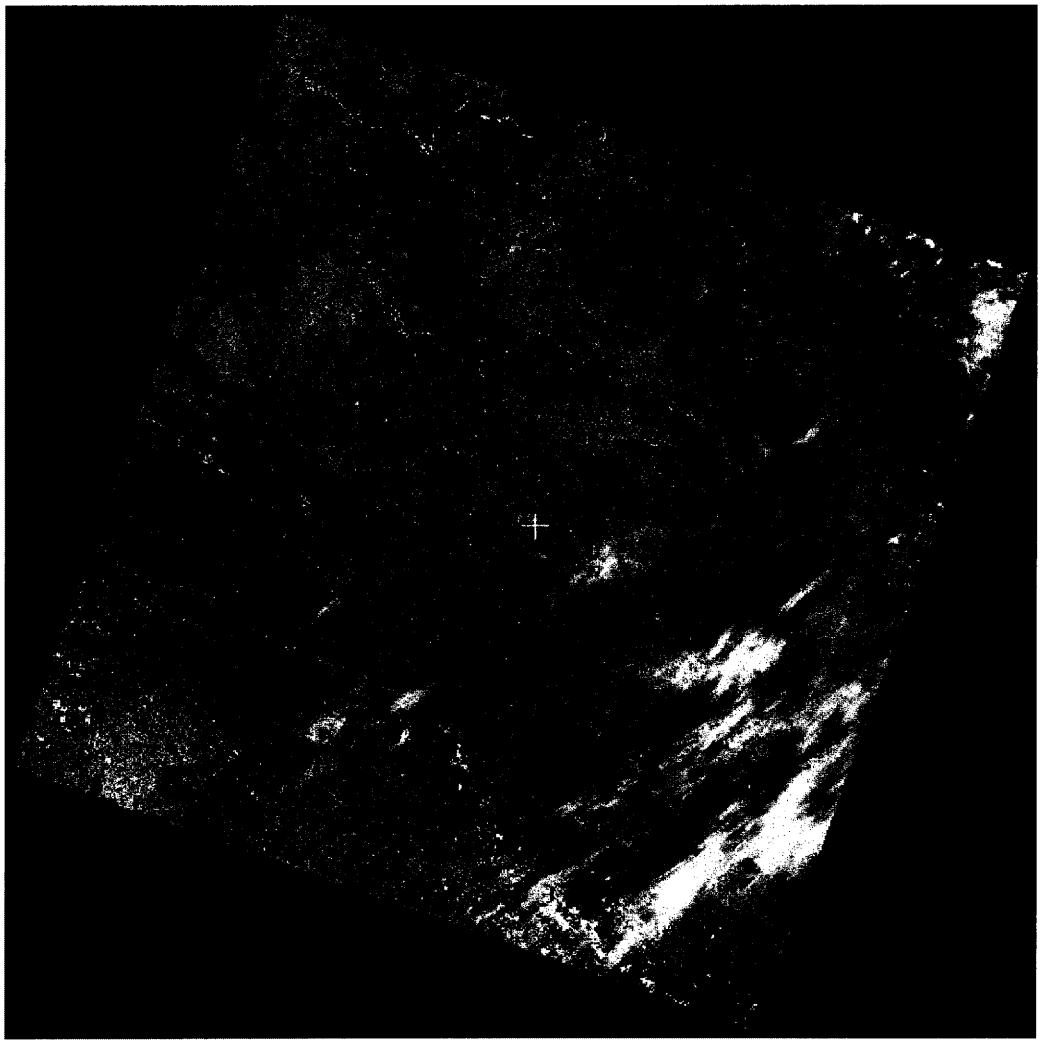

Figure 3.8: Landsat full scene image high resolution with reduced size

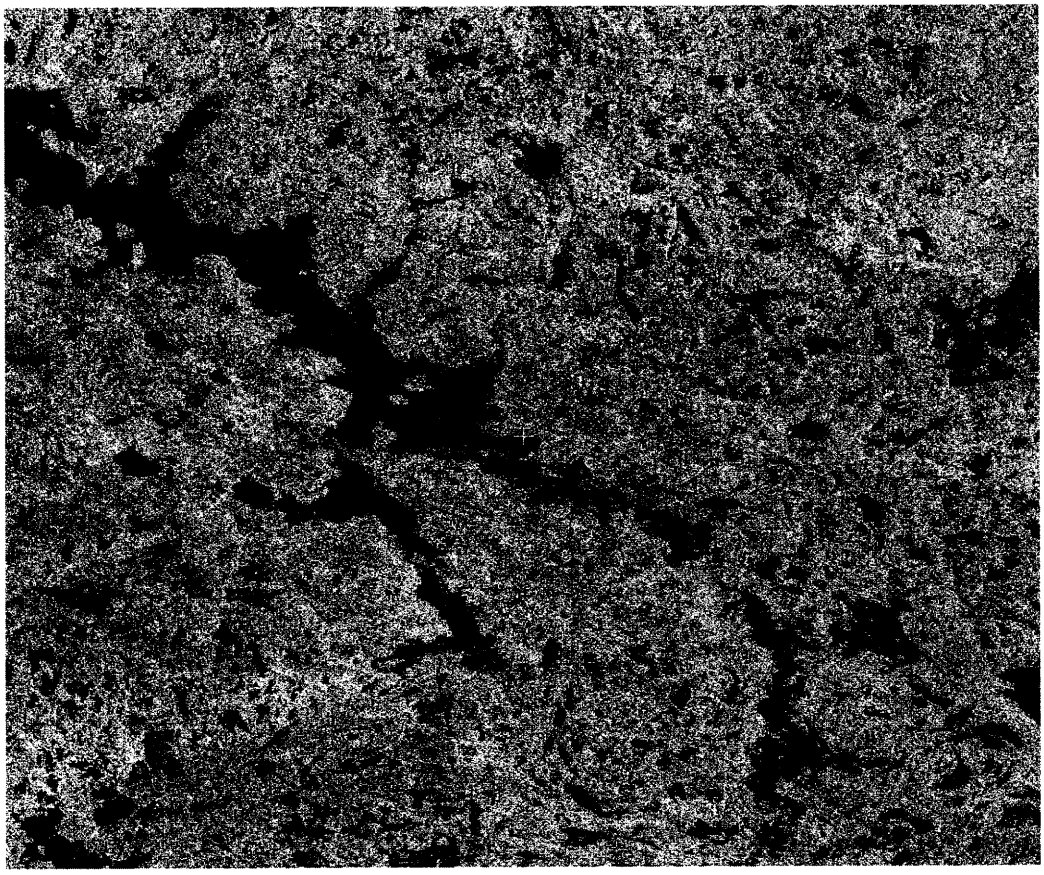

Figure 3.9: RADARSAT image high resolution with reduced size

Table 3.4: RADARSAT Image Full Scene

Scene ID	M0296663
Geographical area	Kitimeot, Nunavut, Canada
Scene start time	July 31 2000
Scene stop time	July 31 2000
Orbit	24739 Descending
Number of image lines	8502
Number of image pixels	8991
Pixel spacing	12.500 m
Scene centre	$66^{o}03^{'}N \quad 108^{o}43^{'}$
Corner coordinates	$66^{o}37^{'}11.12^{''}N \quad 66^{o}24^{'}09.95^{''}W$ $109^{o}42^{'}25.02^{''}N \quad 107^{o}14^{'}23.91^{''}W$ $65^{o}41^{'}12.99^{''}N \quad 65^{o}28^{'}28.30^{''}W$ $110^{o}10^{'}03.25^{''}N \quad 107^{o}47^{'}15.95^{''}W$

InSAR image is 2.5 metre resolution with full size of 2900 x 2480 pixels. Figure 3.10 (a) and (b) shows a full scene of the aerial photo and InSAR images, respectively.

3.7.4 Selected Test Images

A number of small sub-images with full resolution regions have been cut from the RADARSAT, Landsat, aerial photo and InSAR images to be used as test sites for investigating the object extracting and object matching algorithms. The test images are shown in Figure 3.11 to Figure 3.15.

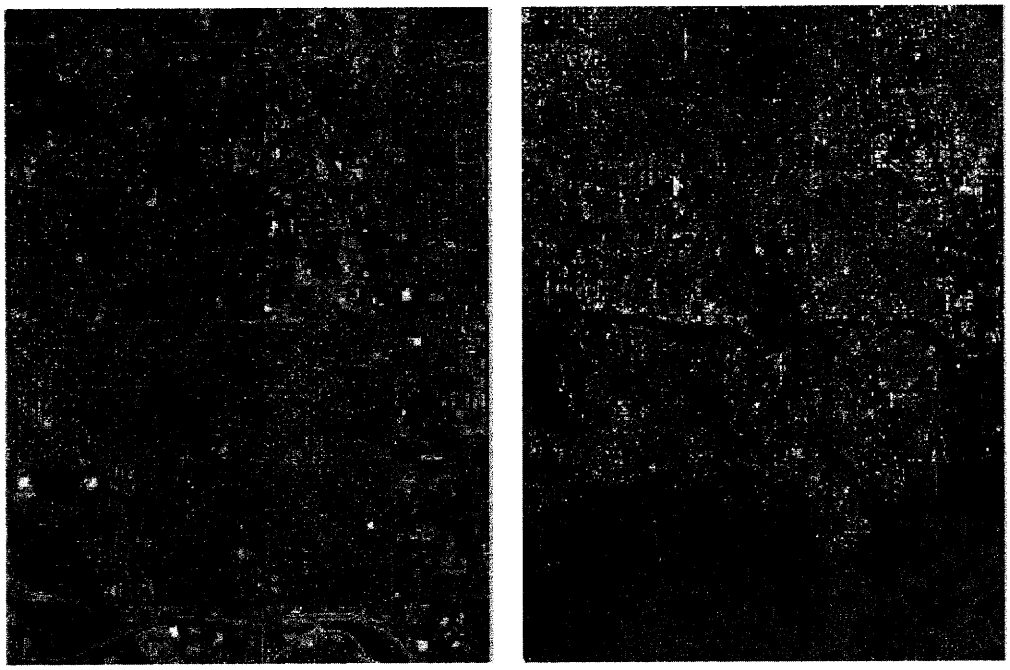

(a) Aerial image (b)InSAR image

Figure 3.10: Aerial and InSAR full scene full resolution images

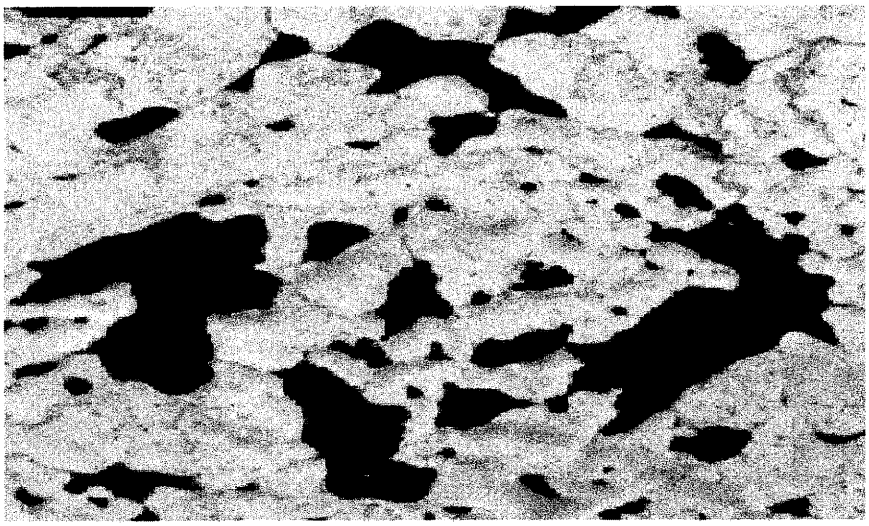

(a)Original Landsat image LS1

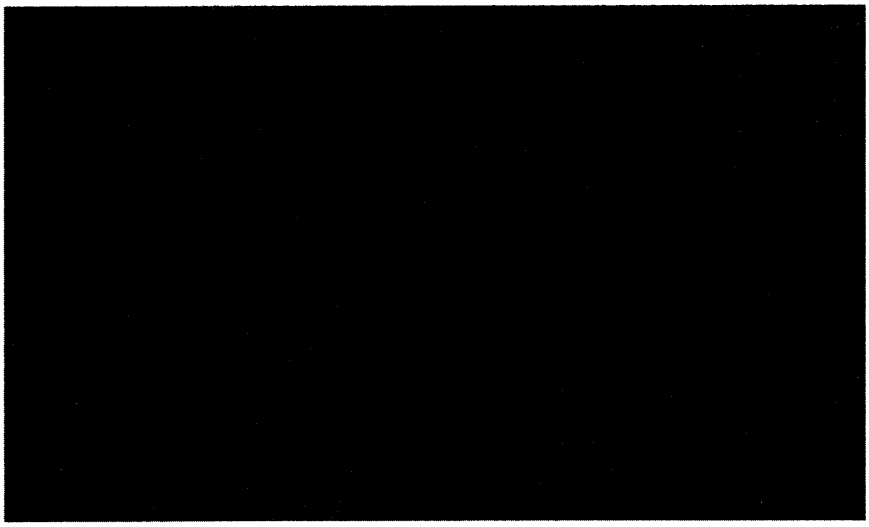

(b)Original RADARSAT image RS1

Figure 3.11: Landsat image1 (LS1) and RADARSAT image1 (RS1)

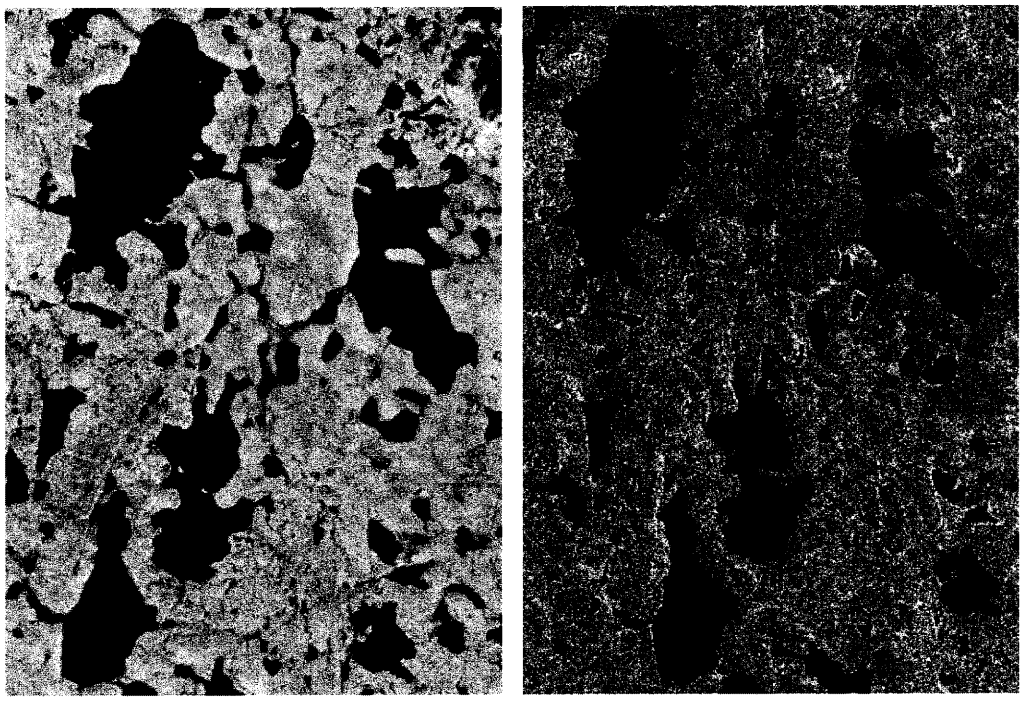

Figure 3.12: Landsat image2 (LS2) and RADARSAT image1 (RS2)

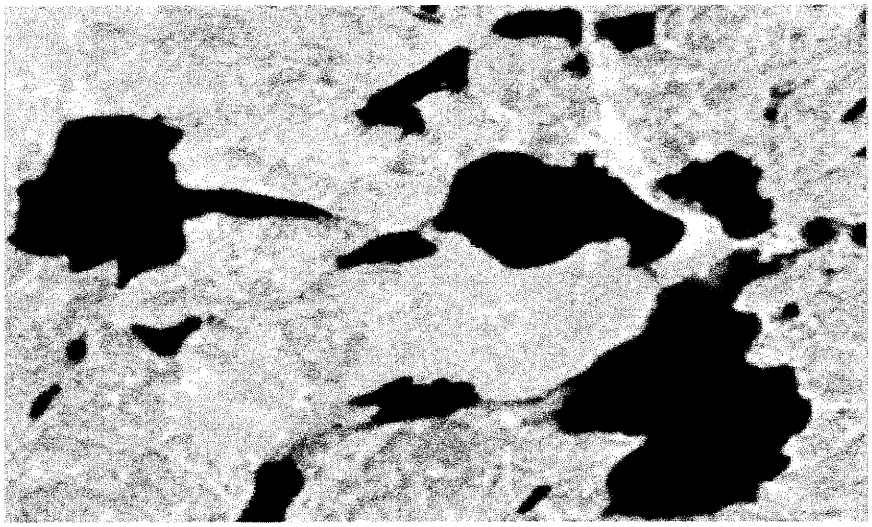

(a) Original Landsat image LS3

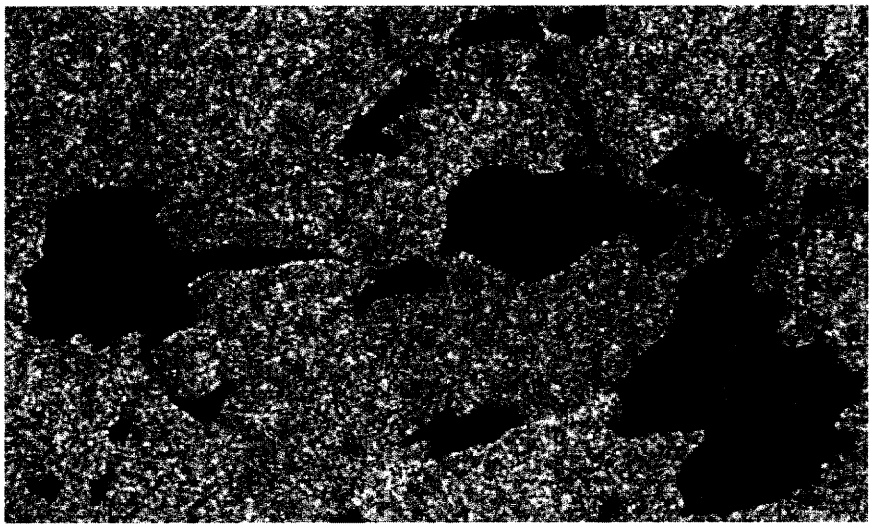

(b) Original RADARSAT image RS3

Figure 3.13: Landsat image3 (LS3) and RADARSAT image3 (RS3)

(a)Original Landsat image LS4

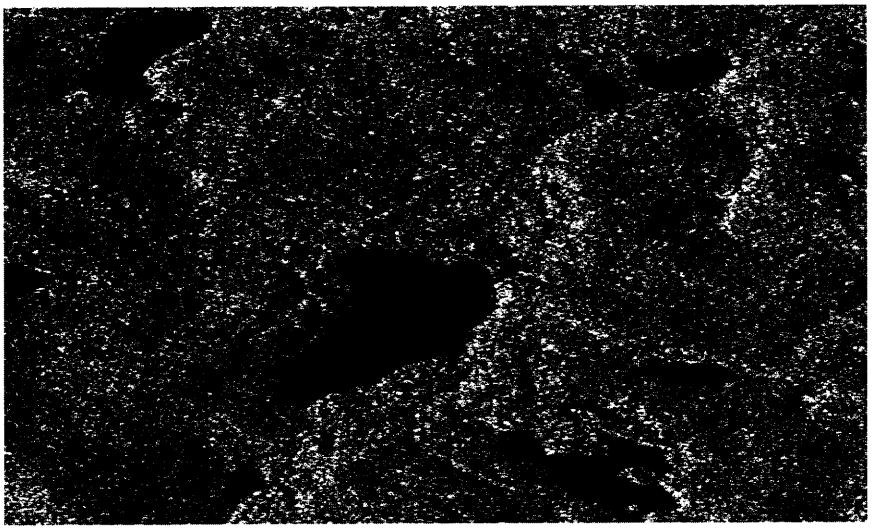

(b)Original RADARSAT image RS4

Figure 3.14: Landsat image4 (LS4) and RADARSAT image4 (RS4)

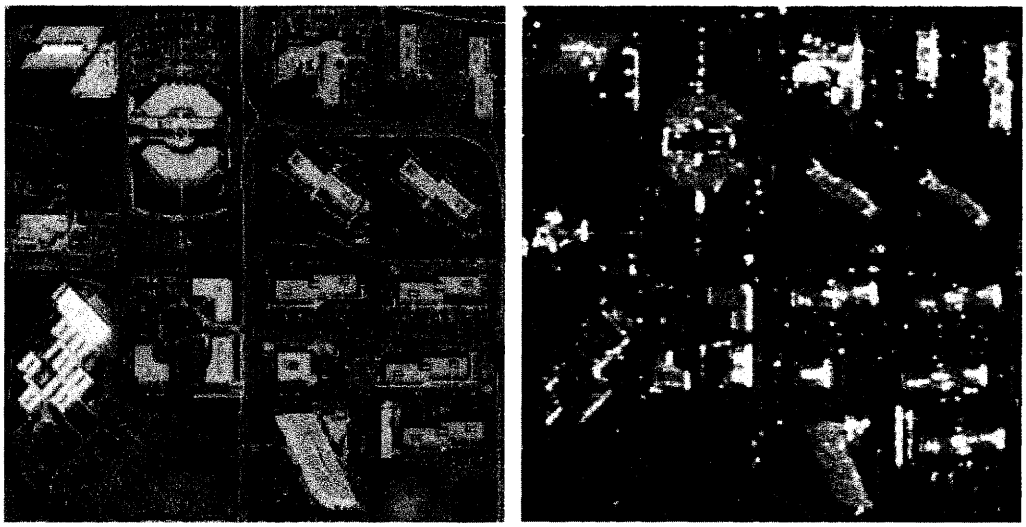

Figure 3.15: Aerial image (AE1) and InSAR (Star-3)image (INS1)

3.8 Preprocessing of SAR Data

In this section, the common SAR filters are applied on the SAR images to reduce the effect of the speckle noise. This speckle filters should reduce the effect of the speckle noise to increase the interpretability and usability of the SAR images. The next subsections address this issue with results and solutions.

3.8.1 Speckle Noise Reduction

Speckle occurs due to random constructive and destructive interference from the multiple scattering returns that occurs within each resolution cell. The speckle noise is considered to be multiplicative noise that expresses the observed intensity as a product of the scene's signal intensity and speckle noise intensity:

$$I = S \cdot u \tag{3.7}$$

where I is the observed intensity of the pixel, S is the terrain reflectivity, and u is the intensity of the fully developed speckle noise.

The reduction of speckle can be obtained by one of two ways: multi-look processing and spatial filters. The multi-look processing divide the radar beam into (n) narrower sub-beams. Each sub-beam provides an independent "look" at the target. These sub-beams are summed and averaged to produce the final image, so the amount of speckle will be reduced since the speckle variance is reduced by a factor of n. At the same time, the resolution is degraded by a factor of n. The multi-look should be used with care because of the trade-off between the number of looks and the image resolution in the SAR preprocessing.

The second way to reduce speckle is to apply spatial filters to the produced SAR image. The Lee adaptive filter is a common speckle reduction technique [76] [77]. Other adaptive filters that have been proposed include the Frost filter [54], Kuan filter [74], GMAP filter [128], Enhanced Lee filter [83], and Enhanced Frost filter [83]. The speckle adaptive filters attempt to reduce the effect of speckle noise while preserving the image details. All known speckle filters only reduce rather than eliminate the effect of speckle.

With respect to InSAR images, the InSAR amplitude speckle is reduced using the speckle adaptive filters, since the speckle nature is multiplicative. The phase noise can be reduce by simple filters such as mean filter, since it is additive in its

nature [79]. This thesis deals with the InSAR phase components, so the simple noise reduction filters can be applied.

3.8.2 Recognized Speckle Reduction Filters

The standard speckle filters such as Statistical Lee, Kuan, Gamma or MAP, Standard Frost, and Enhanced Frost are primarily used on radar data to remove speckle effect. Each of these filters has a unique speckle reduction approach, while these filters as adaptive filters have a common aspect. This aspect is no smoothing near edges to preserve the details. The filtering is based on the statistical relationship between the central pixel and its surrounding pixels. The larger the window size, the more the smoothing and vice-versa. There is a trade-off between smoothing to reduce the effect of speckle noise and losing the feature details. The filtering that these algorithms perform is based on either local statistical data which is given in the filter window to determine the noise variance, or the local noise variance which is estimated by using the effective equivalent number of looks (ENL) of a SAR image. In the filtered image, if the intensity of an area is constant, then the noise variance, determined from the local filter window, is more applicable, but ENL is used if it is difficult to determine if the area of the image has constant intensity.

3.8.3 Median Filter

Median filters were found to be effective with impulsive noise. They replace the filtered pixel by the median value of surrounding neighbouring pixel values. The median is a more robust than the mean such that a single noise pixel in a neigh-

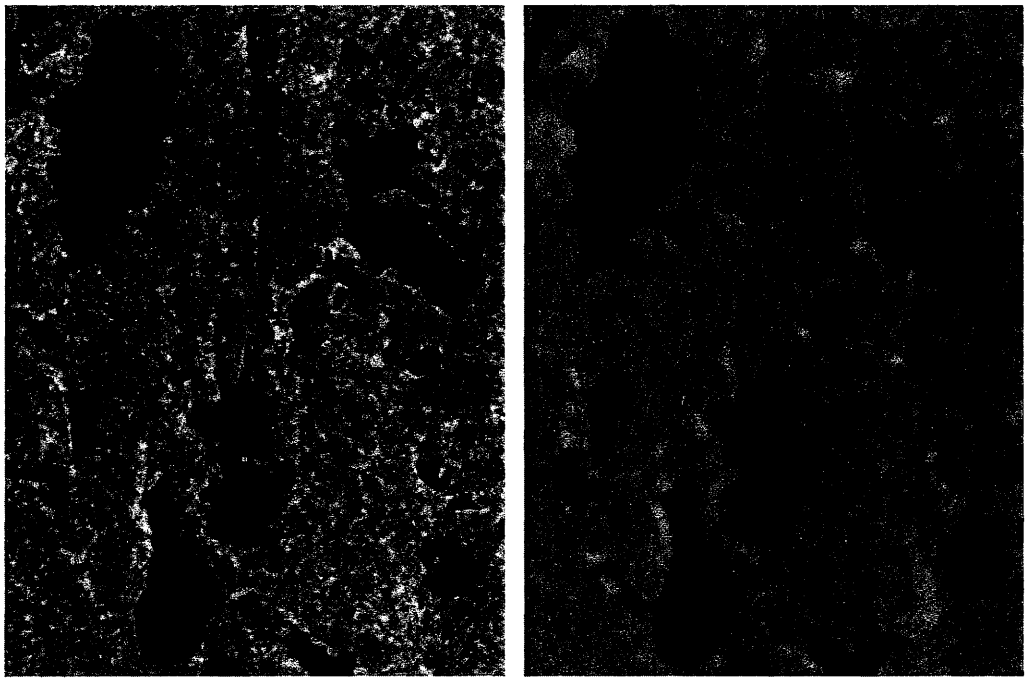

Figure 3.16: Median filter results, left (3x3), right (9x9)

bourhood will not affect the median value significantly. Since the median value must actually be one of the pixel values in the neighbourhood, the median filter does not create new pixel values like the mean filter. For this reason, the median filter is much better at preserving sharp edges than the mean filter. Figure 3.16 exhibits the application of the median filter on the RADARSAT image with different kernels. The main disadvantages of the median filter are eroding corners and the extra computation time needed to sort the intensity value of each set.

3.8.4 Statistical Lee Filter

The Lee filter [78] mainly works with constant intensity areas in the images. It smooths away noise in these constant areas, while preserving fine details with minimum change. The Lee filter works using a scanning window, sometimes called the kernel. For each window, the local mean and variance are estimated. The basic theory of Lee filter is that if the variance over an area is low or constant, then the smoothing will be performed. Otherwise, if the variance is high the smoothing will not be performed. This is very important for preserving edges because the variance near the edges is very high. The Lee filter assumes that the speckle noise is multiplicative; then the SAR image can be approximated by the following linear model:

$$f(i,j) = m + W * (C_p - m_w) \tag{3.8}$$

where $f(i,j)$ is the gray scale value of the pixel at indices i and j after filtering and m_w is the mean of pixel values within a window. The weighting function W is given in Equation 3.9

$$W = \sigma^2/(\sigma^2 + \rho^2) \tag{3.9}$$

and

$$\sigma^2 = [\frac{1}{N}\sum_{j=0}^{N-1}(X_j - m_w)^2] \tag{3.10}$$

where σ^2 is the variance of the pixels values within the filter window given in Equation 3.10, N is the size of the filter window, and X_j is the pixel value within the filter window at indices j.

The parameter ρ^2 is the additive noise variance of the image given in Equation 3.11. M is the size of the image, m_i is the image mean, and X_i is the value of each pixel in the image.

$$\rho^2 = [\frac{1}{M}\sum_{i=0}^{N-1}(X_i - m_i)^2] \tag{3.11}$$

The general form of Lee can be written as:

$$\hat{x} = m_w + [\frac{\sigma_x^2}{\sigma_x^2 + \sigma^{v2}m_w^2}](x - m_w)(3.12)$$

where

$\hat{x} =$ *new value pixel assigned to central pixel in window*

$x =$ *original value of central pixel in window*

The main disadvantage of the Lee filter as adaptive filter is that it tends to ignore speckle noise in the areas closest to edges and lines to preserve edges.

3.8.5 Kuan Filter

The Kuan filter [74] does not make an approximation on the noise variance within the filter window. The Kuan filter models the multiplicative nature of speckle into an additive linear form, but it relies on the equivalent number of looks ENL from a SAR image to determine a different weighting function W given in the following Equation to perform the filtering:

$$W = (1 - C_u/C_i)(1 + C_u) \tag{3.13}$$

The weighting function is computed from the estimated noise variation coefficient of the image. C_u, is given by

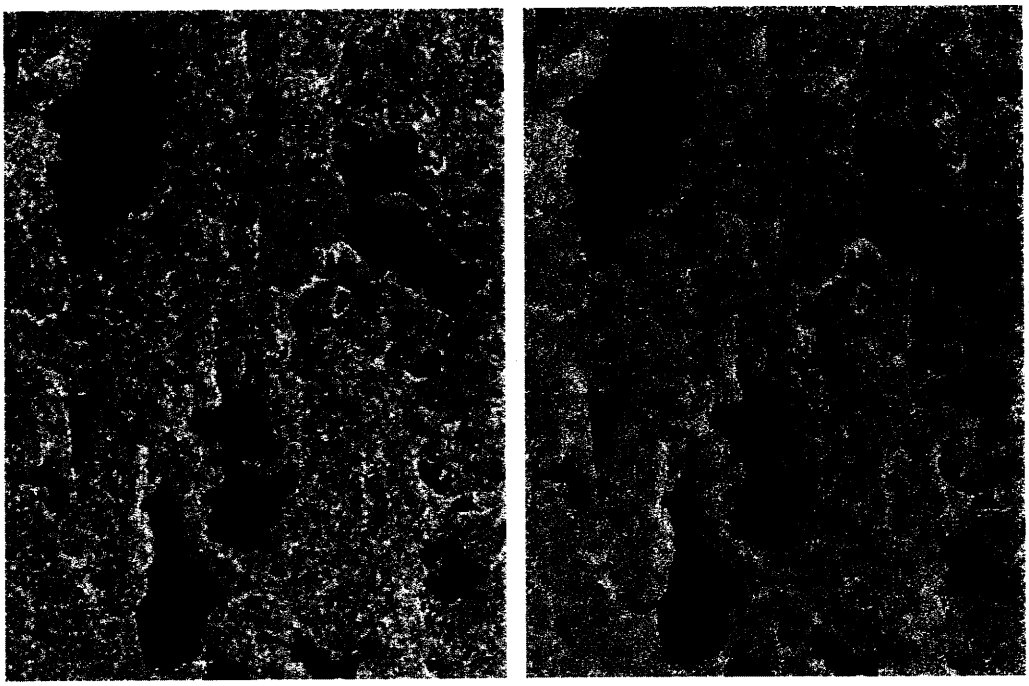

Figure 3.17: Lee filter results, left (3x3), right (9x9)

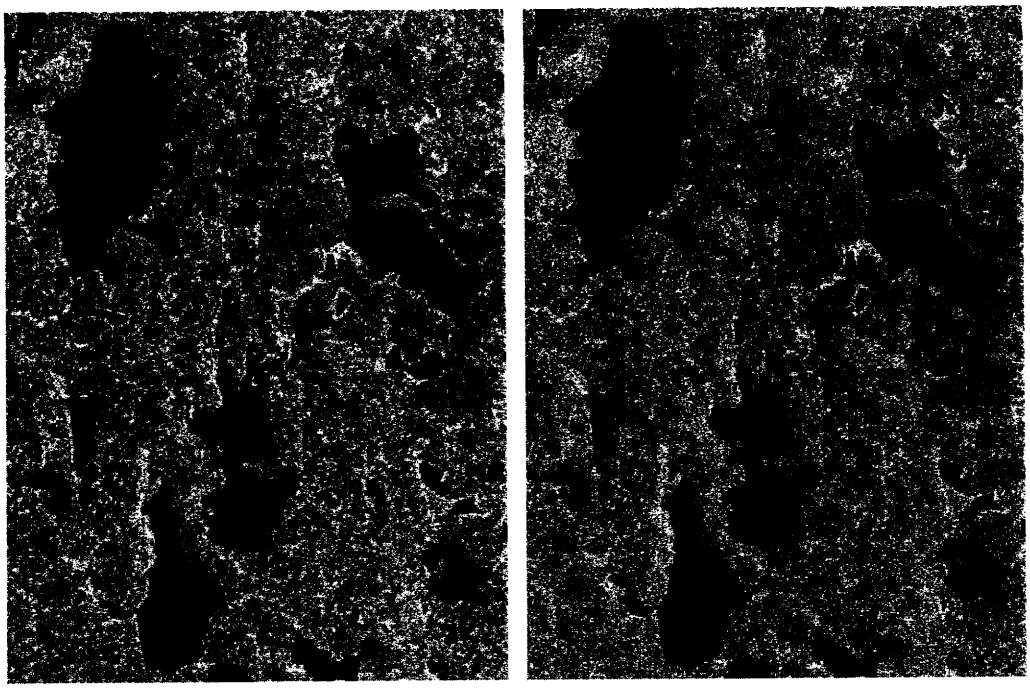

Figure 3.18: Kuan filter results, left (3x3), right (9x9))

$$C_u = \sqrt{1/ENL} \tag{3.14}$$

$$ENL = \frac{m_i^2}{\sigma_i^2} \tag{3.15}$$

and C_i is the variation coefficient of the image given in

$$C_i = \sigma / m_w \tag{3.16}$$

The general form of Kuan filter can be written as

$$\hat{x} = m_w + [\frac{\sigma_x^2}{\sigma_x^2 + \sigma_v^2(m_w^2 + \sigma_x^2)}](x - m_w) \tag{3.17}$$

3.8.6 Frost Filter

A Frost filter [54] adapts to the noise variance within the filter window by applying exponential weighting factors M as given in

$$M_n = exp(-(DP * (\sigma/m_w)^2) * T) \tag{3.18}$$

These weighting factors decrease as the variance within the filter windows reduces. DP is a factor that determines the extent of the exponential damping for the image. The larger the damping value, the heavier the damping effect. Typically the value is set to 1. T is the absolute value of the pixel distance between the centre pixel to its surrounding pixels in the filter window. The value of the filtered pixel is replaced with a value calculated from the weighted sum of each pixel value P_n and the weights of each pixel M_n in the filter window over the total weighted value of the image as follows:

$$f(i,j) = \frac{\sum P_n * M_n}{\sum M_n} \tag{3.19}$$

The parameters in the Frost filter are adjusted according to the local variance in each area. If the variance is low, then the filtering will cause extensive smoothing, but in high variance areas, little smoothing occurs and the edges are retained.

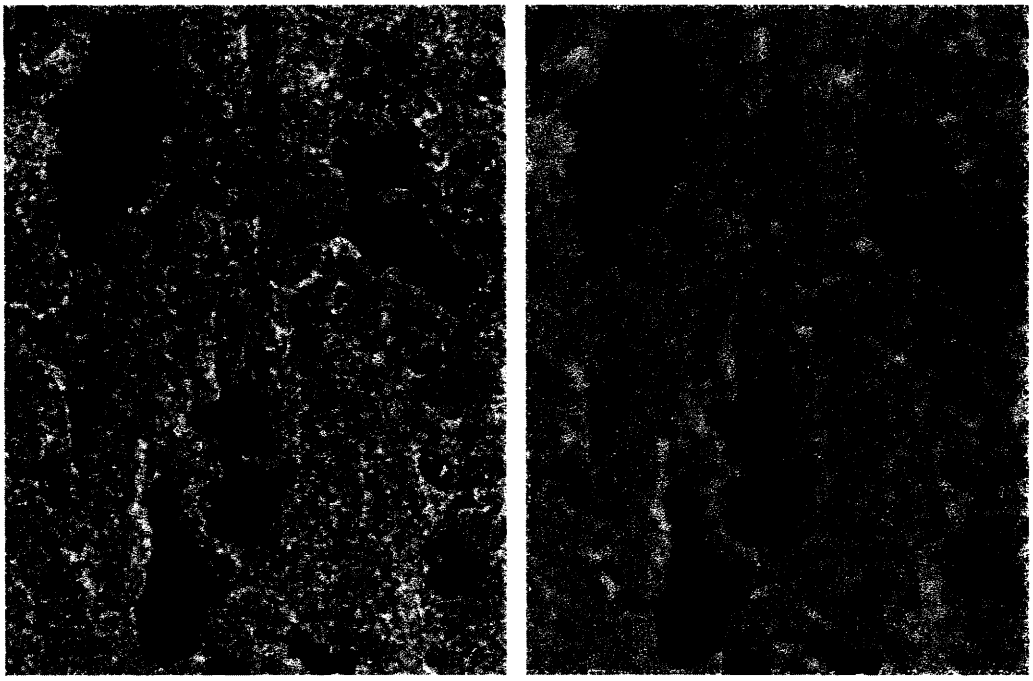

Figure 3.19: Frost filter results, left (3x3), right (7x7)

3.9 Proposed Improved Speckle Filters

The Lee, Kuan, and Frost speckle reduction filters perform some form of averaging on the pixels surrounding the pixel being processed. On account of median filter simplicity, edge preservation property, and robustness to impulsive noise, the median filter remains the most popular for image processing applications [11]. The median filter, however, often has some drawbacks including removing fine detail such as thin lines and corners [11]. In recent years, a variety of median-type filters [11] such as stack filters, multi-stage median, weighted median, and relaxed median [134] have been designed to overcome this drawbacks.

In [34], the authors felt that the replacing of mean algorithm by the median algorithm can lead for better retention using certain filters such as the Sigma filter, the most homogeneous neighbour (MHN) filter and the k-averaging filter. It was difficult to judge on these modified filters from there visual results compared to the corresponding original filters. A speckle index and edge retention measures proved better performance than the original filters while the original images faced much smoothing.

In this thesis, since Lee, Kuan and Frost filters are the most used speckle reduction filters in the SAR community, the concept of replacing the average algorithm by the median algorithm is applied to these speckle reduction filters. The modified speckle reduction filters are called the MLee, MKuan and MFrost.

The difference between the application of original Lee and MLee filters are reflected in Figures 3.20 and 3.21. Figures 3.22 and 3.23 show the application of the original Kuan filter and MKuan filter with different kernels. Finally, application

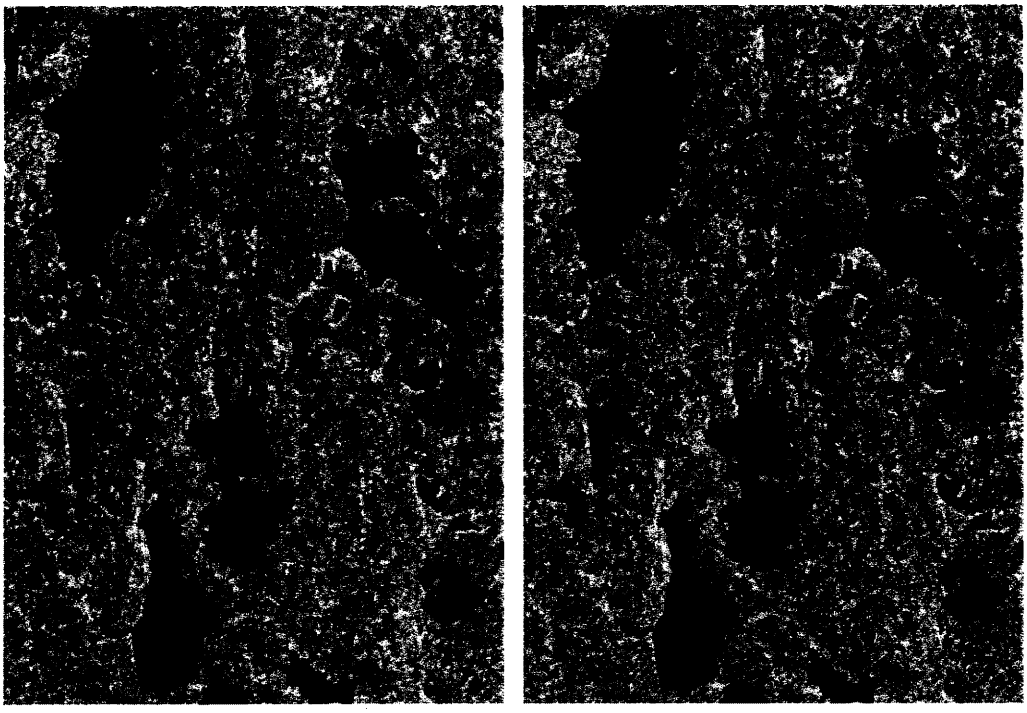

(a) (b)

Figure 3.20: (3x3) mask: (a)Lee filter result (b)MLee filter result

of Frost filter and MFrost filter are shown in Figures 3.24 and 3.25.

The general form of MLee can be written as

$$\hat{x} = med + [\frac{V_x}{V_x + V_v * m^2}](x - med) \tag{3.20}$$

The general form of MKuan can be written as

$$\hat{x} = med + [\frac{\sigma_x^2}{\sigma_x^2 + \sigma_v^2(m^2 + \sigma_x^2)}](x - med) \tag{3.21}$$

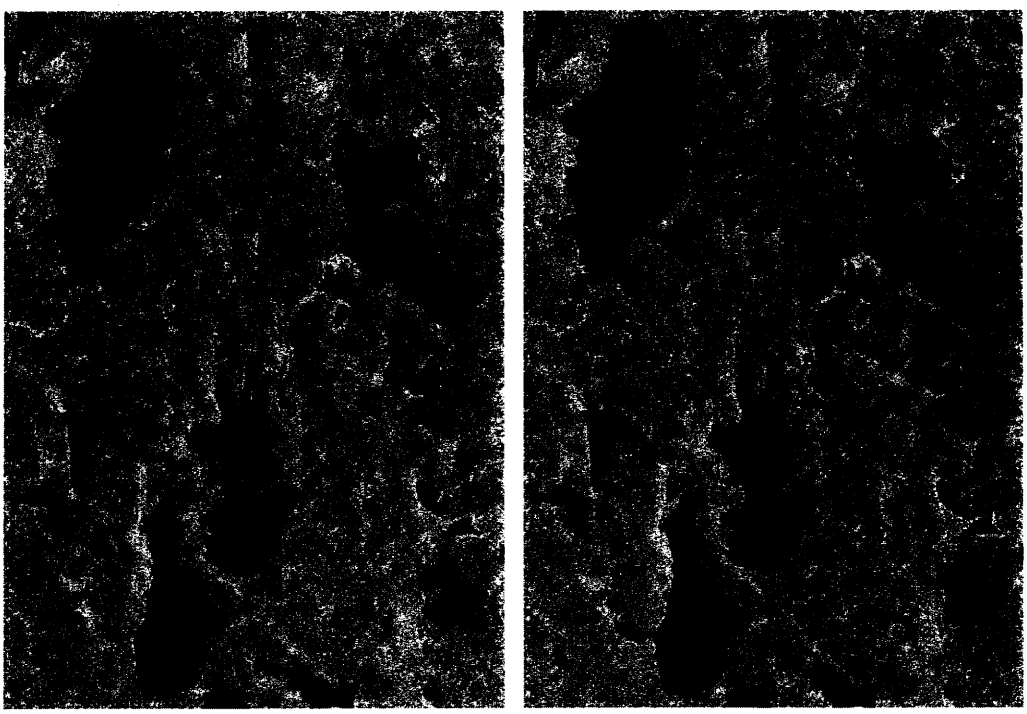

(a) (b)

Figure 3.21: (9x9) mask:(a)Lee filter result, (b)MLee filter result

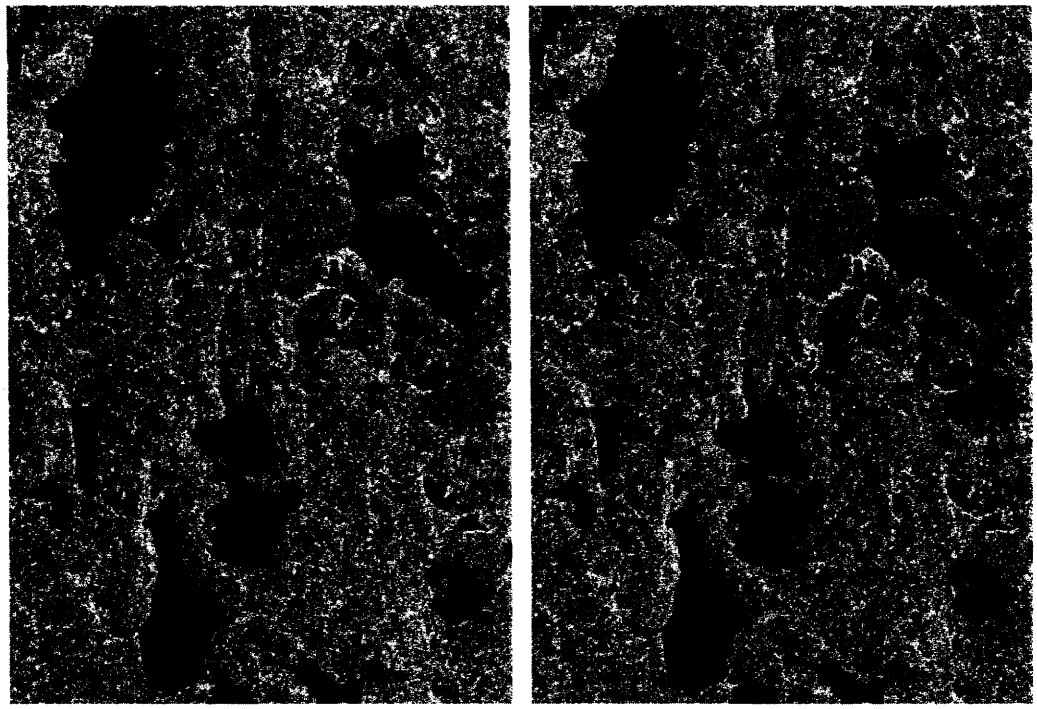

(a) (b)

Figure 3.22: (3x3) mask: (a)Kuan filter result, (b)MKuan filter result

where *med* represents the median value within the filter window.

From Figure 3.22 to Figure 3.25, the application of the MLee, MKaun and MFrost filters do not give much an improved visual results compared to Lee, Kuan and Frost speckle reduction filters. A quantitative comparison between the Lee, Kuan and Frost filters and the modified filters are given in Section 3.10.

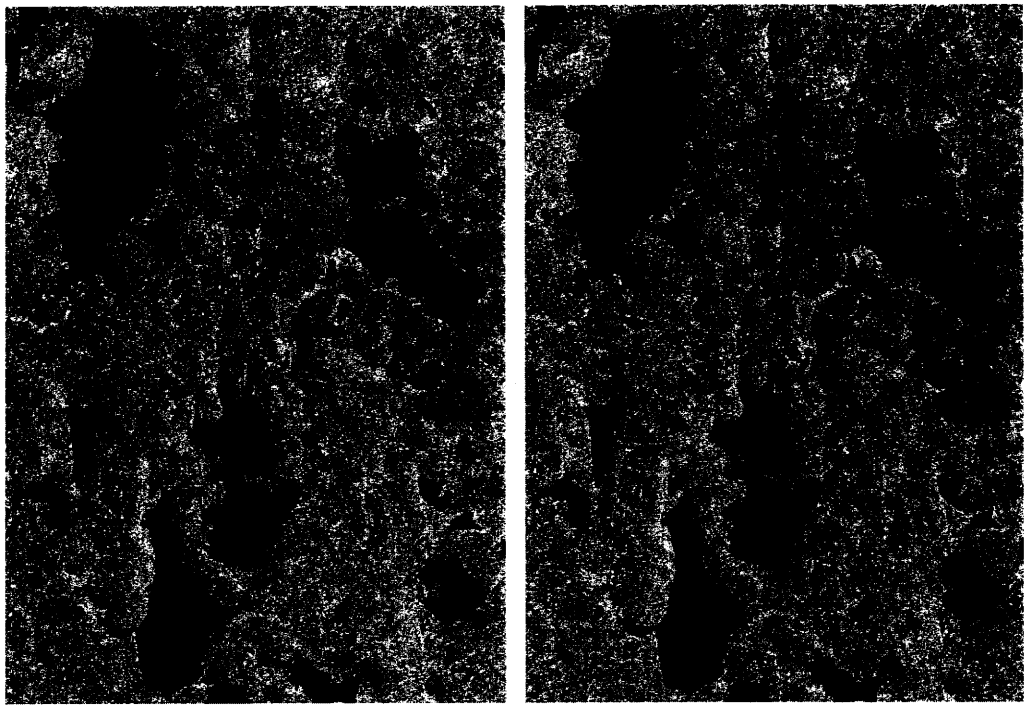

(a) (b)

Figure 3.23: (9x9) mask: (a)Kuan filter result, (b)MKuan filter result

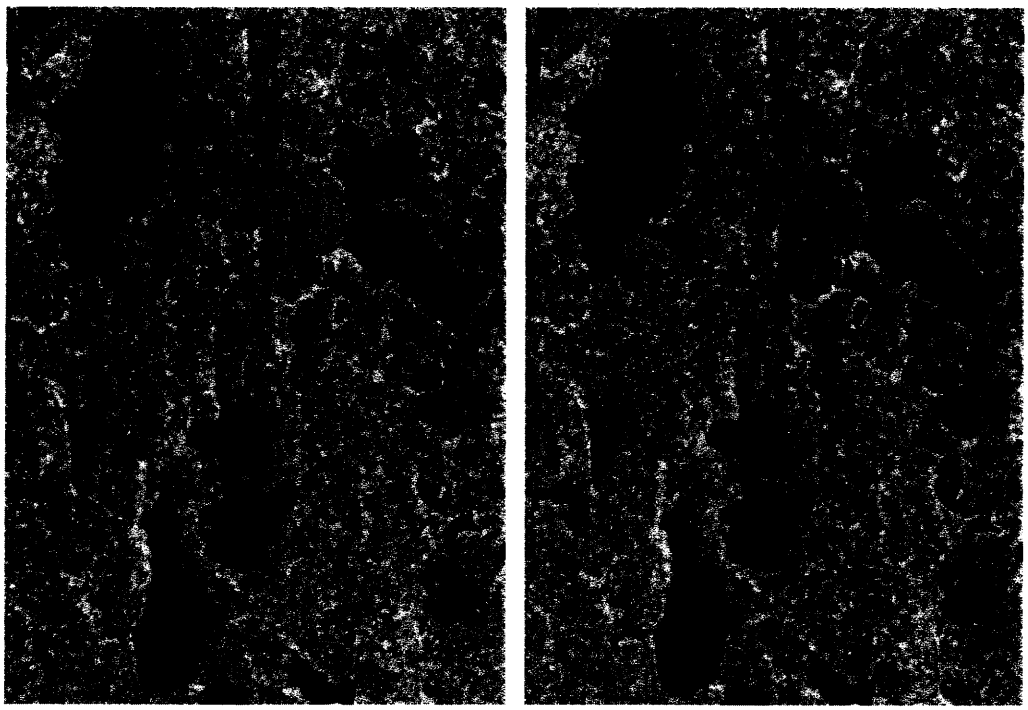

Figure 3.24: Applying Frost filter left, Applying MFrost right (3x3)

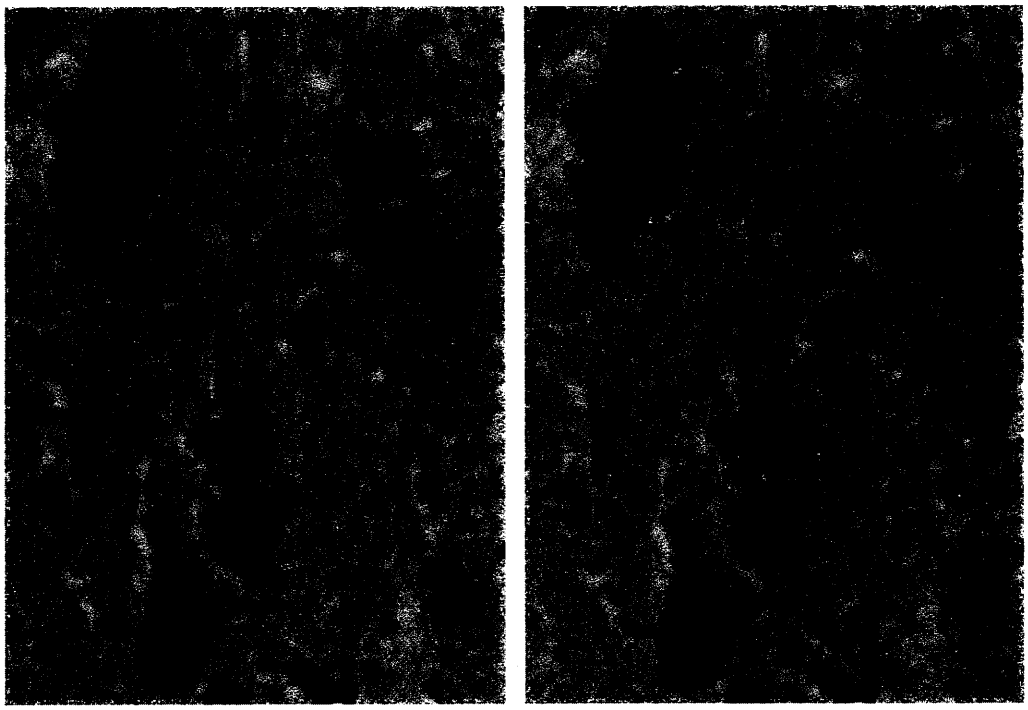

(a) (b)

Figure 3.25: (7x7) mask:(a)Frost filter result, (b)MFrost filter result

3.10 Comparison Between the Modified and the Original Speckle Reduction Filters

The rating of speckle filter performance by using objective criteria is quite difficult, since the behavior of the adaptive filters used is extremely sensitive to the image contents. The requirements of filter algorithms should be analyzed, and comparison rules derived in order to create rating criteria that are useful for practical applications.

To quantify the speckle noise reduction, the speckle index is computed [28]. The speckle index is defined by

$$Speckle\ index = \frac{1}{MN} \sum_{m=1}^{M} \sum_{n=1}^{N} \frac{\sigma^2(m,n)}{\mu(m,n)} \tag{3.22}$$

where σ^2 and μ are the local variance and mean. The speckle index determines the amount of speckle in a SAR image. This speckle index should be measured before and after applying a filter. The ratio can give an indication of the speckle filter performance. A low speckle index does not necessarily indicate the best results, but it may represent high smoothing.

A measure of the retention of features during speckle filtering is hard to quantify. Edge retention is one of the performance measures of speckle reduction filters. By measuring the gradient of step edges before and after applying the speckle reduction filter, the filter edge retention could be assessed.

For the edge retention indicator, a value close to 1 represents a high degree of

retention of the features, whereas a value close to zero represents a poor retention of the features. All of the filters are applied by using a 3x3 sliding window on given SAR images. One application of filters on RS2 image is grouped together in Table 3.5, according to the type of filter. It can be seen from this table that the three modified filters are superior to the original filters in edge retention. As for the speckle index, the filter groups performed almost identically. The slight difference observed can be attributed to the less smoothing performed by the modified filters due to using the median algorithm rather than the mean algorithm.

A synthesized step edge image (200 x 200 pixels) is created for evaluation purposes and the modified filters are applied to this step edge image. In the original synthesized image, the step edge is at value 100. After applying a filter, the closer the step edge to 100 the better job the filter does in preserving edges. The step edge image and the speckled step image are given in Figure 3.26. The results of applying the original and the modified filters to the synthetic image are illustrated in Figures 3.27 and 3.28. From the Figure, it is obvious the application of the improved filters to the step edge retained the step edge. The modified filters were also applied to speckled step edge. The results are shown in Figures 3.29, 3.30, and 3.31. From Figure 3.29, the step edge is apparently highly smoothed after applying Lee filter (started near 92), while the Mlee filter kept the step edge near to 100 and preserved the sharp edge. The same observation could be made with Kuan and Mkuan, and Frost and Mfrost filters. there is one comment that when applying the original Kuan filter to the noisy step edge, the resulted smoothed step edge had many high repels which was unexpected (Figure 3.30). From the results above, it is clear that Lee, Kuan, and Frost resulted in much more smoothing of the step edge

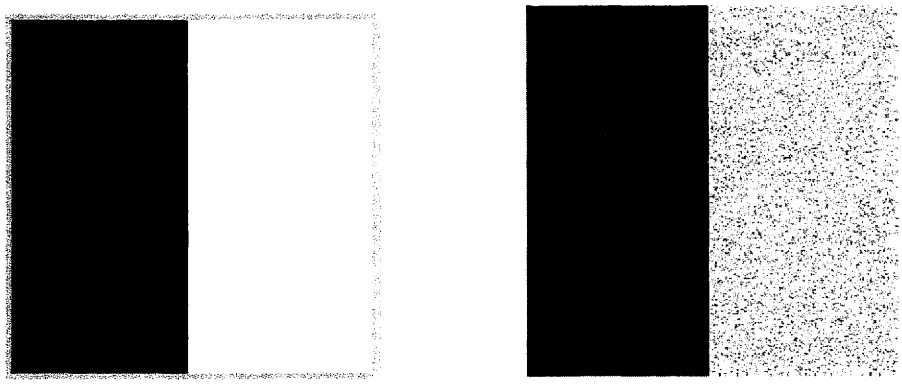

Figure 3.26: A step edge and speckled step edge

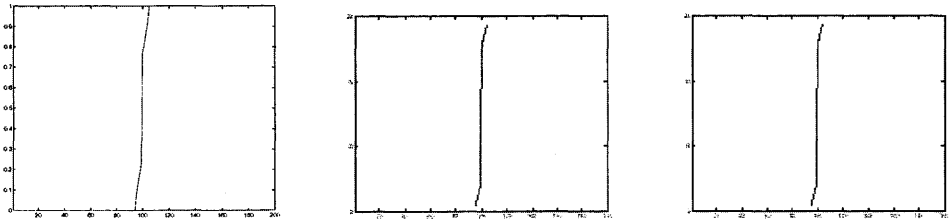

Figure 3.27: Applying Lee, Kuan, Frost on step edge

due to the use of the mean algorithm rather than the median algorithm.

Another quantitative measure that can test the efficiency of the modified filters is the signal to noise ratio (SNR). A synthesized checkerboard image was speckled and shown in Figure 3.32. The two filter sets, (Kuan, Lee, and Frost) and (MKuan, Mlee, and Mfrost) were tested by measuring SNR before and after applying the filters. The modified filters proved high SNR while reducing the speckle effect. Table 3.6 summarizes the result of the test.

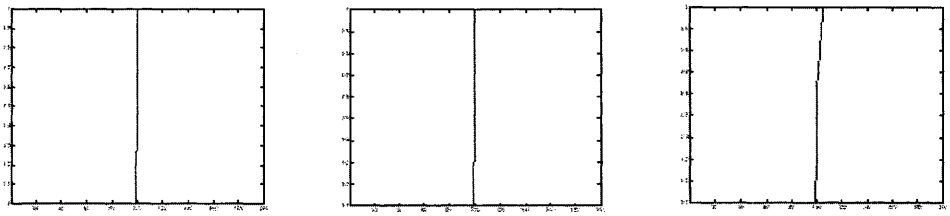

Figure 3.28: Applying MLee, MKuan, MFrost on step edge

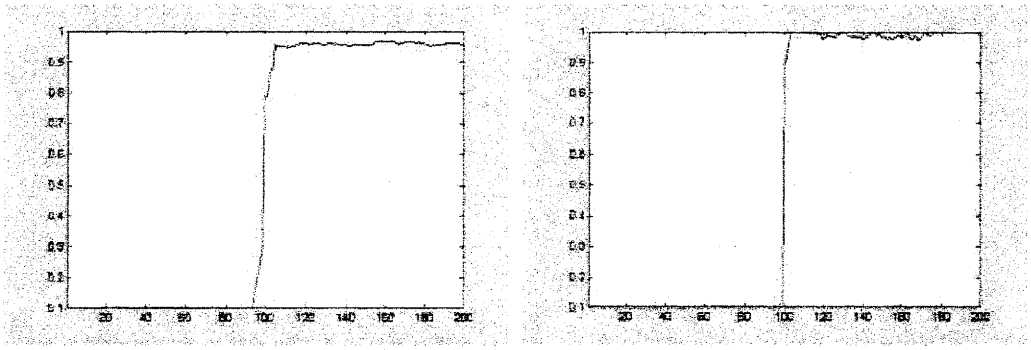

Figure 3.29: Applying Lee and MLee to a noisy step edge

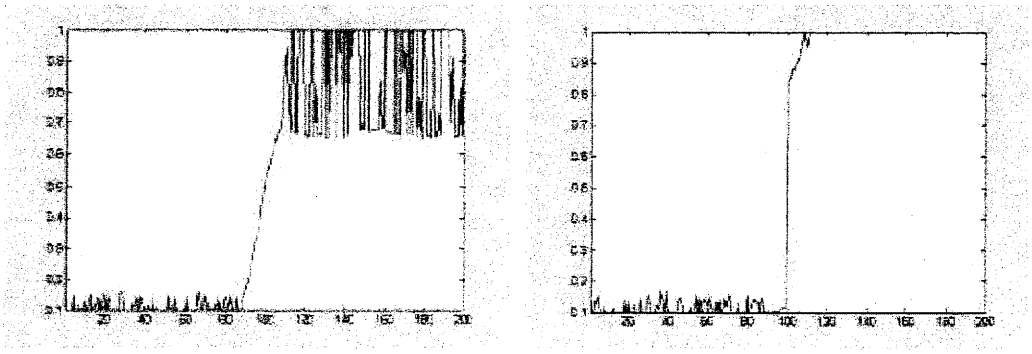

Figure 3.30: Applying Kuan and MKuan to a noisy step edge

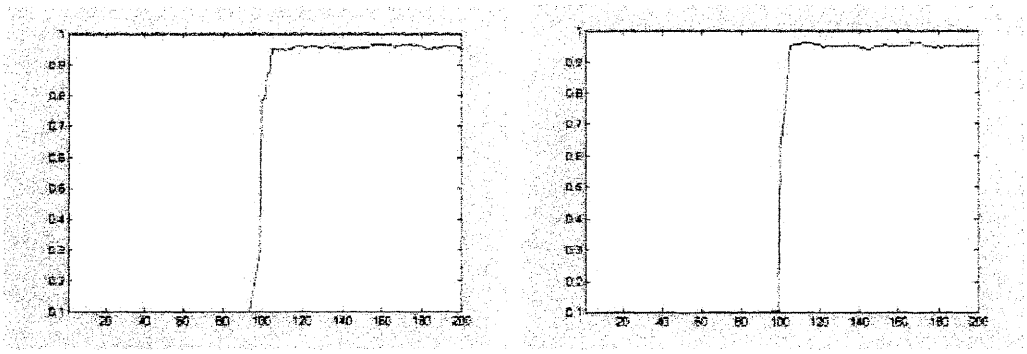

Figure 3.31: Applying Frost and MFrost to a noisy step edge

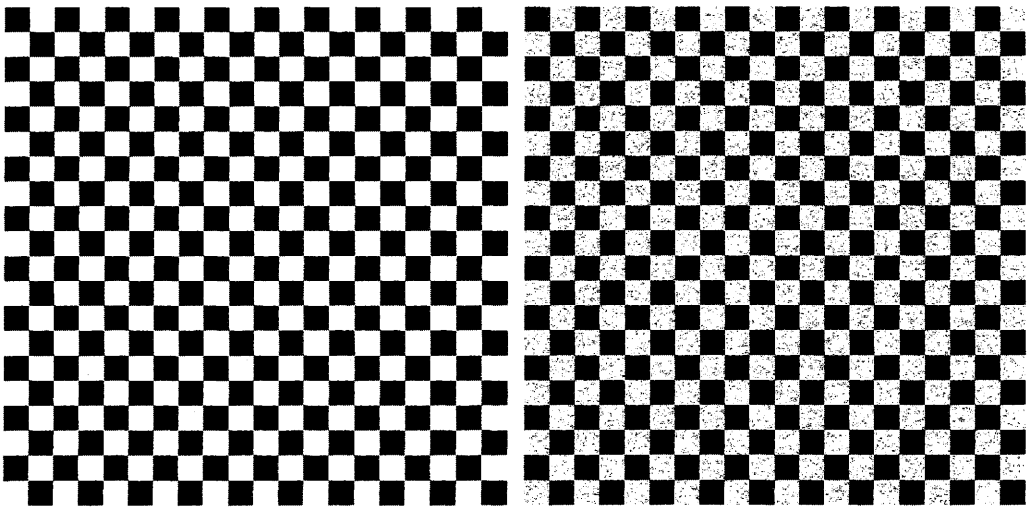

Figure 3.32: A synthesized checkerboard and its speckled version

Table 3.5: A Comparison between Speckle Reduction Filters

Speckle Reduction Filter	Speckle Index	Edge Retention
Kuan	0.063	74 %
MKuan	0.068	82 %
Lee	0.048	59 %
MLee	0.05	71 %
Frost	0.045	31 %
MFrost	0.046	49 %

Table 3.6: Signal to Noise Ratio Test

Speckle Reduction filter	Signal to noise ratio
Original speckled image	38.2145
Kuan	38.12
MKuan	51.31
Lee	38.18
MLee	44.77
Frost	40.90
MFrost	56.95

3.11 Preprocessing of Visible-Band Data

Due to the high signal to noise ratio of optical images, very little radiometric preprocessing is required. Noise does not influence the objects, so no much smoothing is required. However, sometimes to aid the feature extraction algorithms, sharpening filters may be used.

Enhancement is used to bring fine details to the front of the image and to sharpen the edges of objects. The well known sharpening filters un-sharp masking and (1-Laplacian) are applied for this purpose [112]. The results of one of these

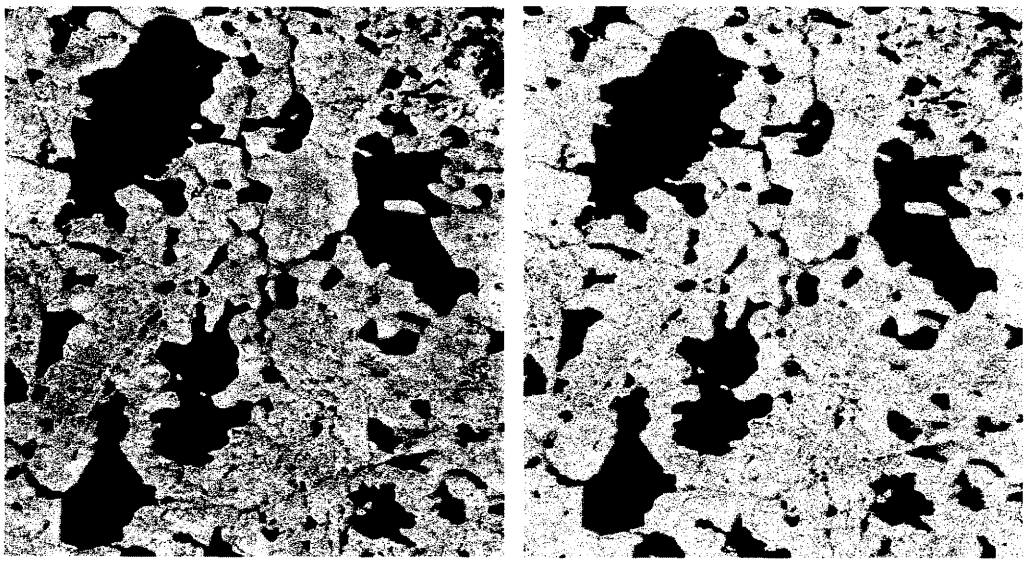

Figure 3.33: Original Landsat image left, Applying un-sharp filter right

filters are shown in Figure 3.33.

3.12 Discussion

In this chapter, different SAR data properties, basic concepts, and the sources of geometric distortion have been introduced. Speckle reduction is not an easy operation, and many researchers have addressed this problem. The existing noise reduction filters and their application to the test data have been presented. The application of the existing speckle reduction filters indicates the need for certain improvements. As a result, three modified speckle reduction filters have been discussed. The modified filters have shown speckle reduction, while preserving the image details. At the end of this chapter, the enhancement of visible band images

has been considered. Chapter 3 has also mentioned different data sets for testing the developed techniques (ARTSO) and (ARVS). All the algorithms will be integrated with the feature extraction algorithms later in the thesis.

Chapter 4

ARTSO Object Extraction

4.1 Feature Extraction

This chapter details the principles behind the feature extraction used in the proposed ARTSO model. Feature extraction is pivotal to feature-based image registration. Automatic feature based image registration of different types of images involves two main challenges: feature extraction and feature matching. The success of the matching process depends mainly on the accuracy of the feature extraction process. Therefore, researchers continue to concentrate on developing feature extraction algorithms that enable the extraction of suitable features from each image to be matched.

Any two-dimensional patch in an image is simply called an object. Although it is easy for the human visual system to detect the extent of an object, it is much more difficult for a computer to perform the same task. To extract the object features from a given image, a segmentation technique should be applied.

4.2 Image Segmentation Techniques

Effective image segmentation is not only one of the most difficult tasks in image processing but also the key to the successful solution to feature extraction. There are two principal approaches to the segmentation of gray level images: partitioning based on abrupt gray level changes and grouping according to the gray level similarities. The principal techniques in the former approach depend on edge detection, whereas the latter approach depends on region growing techniques.

4.2.1 Segmentation Methods Based on Thresholding

Thresholding is one of the most commonly used segmentation methods because of simplicity [63] [114]. The resulting image from thresholding is a binary image which has black and white regions corresponding to the different gray-level values using certain threshold value [62]. All the pixels in the image $f(x, y)$ that have a gray-level value less than the threshold value T are labelled black and the rest of the pixels are labelled white, such that:

$$f(x,y) = 1 \text{ if } f(x,y) \geq T$$
$$= 0 \text{ if } f(x,y) < T$$

If the gray level histogram of the image is bimodal, then in this case, the manual threshold can be easily determined by taking the value that is in the valley of the histogram. Figure 4.1 exemplifies this type of image and its corresponding histogram. Finding an optimal threshold value for an image automatically can be

a challenging task.

Determining an optimal threshold is inherently difficult due to the fact that there are usually variations within scenes. Optimal thresholding can be achieved but tends to be computationally intensive. An approximate value for the threshold can be obtained by using numerical methods such as in entropy-based thresholding [73]. The threshold-based approaches often lack the sensitivity and specificity needed for accurate segmentation.

The most appropriate level for the threshold can be determined from the shape of the histogram. The fact that the shape of the histogram depends on the content of the image makes the success of automatic thresholding heavily dependent on the image content as well. Consequently, automatic thresholding is not appropriate for all types of images. In this thesis, the thresholding technique for feature extraction is not used in remotely sensed applications since these images are not always bimodal and thresholding will not always produce reasonable results when applied to SAR images.

4.2.2 Region-Oriented Segmentation Methods

Region growing is one of the segmentation methods which is based on grouping pixels that have similar gray-levels or same other parameter, such as texture into regions. The process begins by finding the starting points for growing (seeds). The seeds start to grow until they form the shape of the regions. Due to the inhomogeneity of gray levels caused by speckle noise in SAR images which results in inaccurate object boundaries, gray level-based segmentation techniques are not appropriate for this type of images.

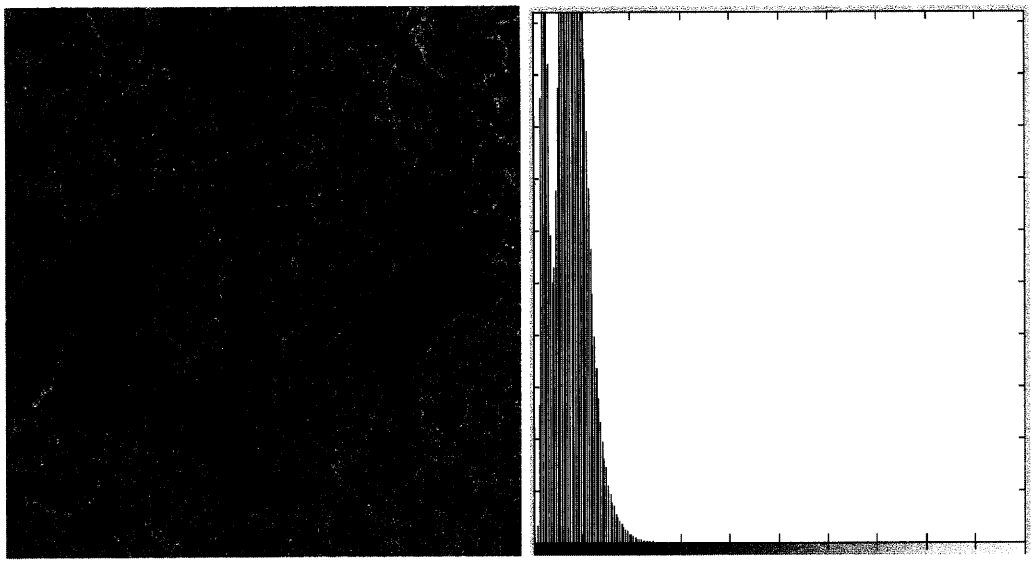

(a)SAR image (b)SAR corresponding histogram

Figure 4.1: SAR image and corresponding bimodal histogram

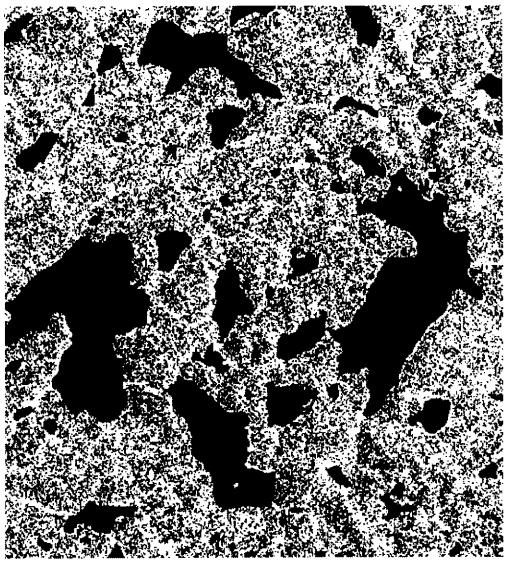

Figure 4.2: SAR thresholded image at grey level of 97

One example of a current SAR segmentation technique is Merge Using Moments (MUM) [21][27]. The MUM algorithm begins by over segmenting the image, by considering each pixel as a separate region and then merging neighbouring regions to produce a coarser segmentation . The merging technique uses the statistical moments of the regions to merge those that represent the same underlying cross-section. This process is then repeated as long as the possibility of merging still exists. The merging process can by controlled by manipulating a tuning parameter, p. If the probability that two neighbouring regions represent the same underlying cross-section is greater than 10^{-p}, the regions are merged. Figure 4.3 shows MUM being applied to a SAR image and the results are either over segmentation or under segmentation. This technique still needs user intervention to set the p value to reach the approximate segmentation. A research based on patch extraction used MUM for this purpose. The MUM parameter set manually to obtain the desired segmentation [35]. Although it is suggested by [35] to use brute force to estimate the parameter, the conclusion were the result is image dependent and selection of the parameter manually is quicker and more accurate.

From Figure 4.3, it is obvious that the resulting segmentation for the given image is not accurate if compared to the original image. For applications such as conducting search and rescue operation with RADARSAT, image accuracy is vital because this image represents a considerable area on the ground.

Existing segmentation techniques still do not give accurate results for segmenting remotely sensed images especially SAR images, because SAR images are distorted by speckle noise and have low signal to noise ratio. The existing segmentation techniques are mostly application dependent and there is no segmentation

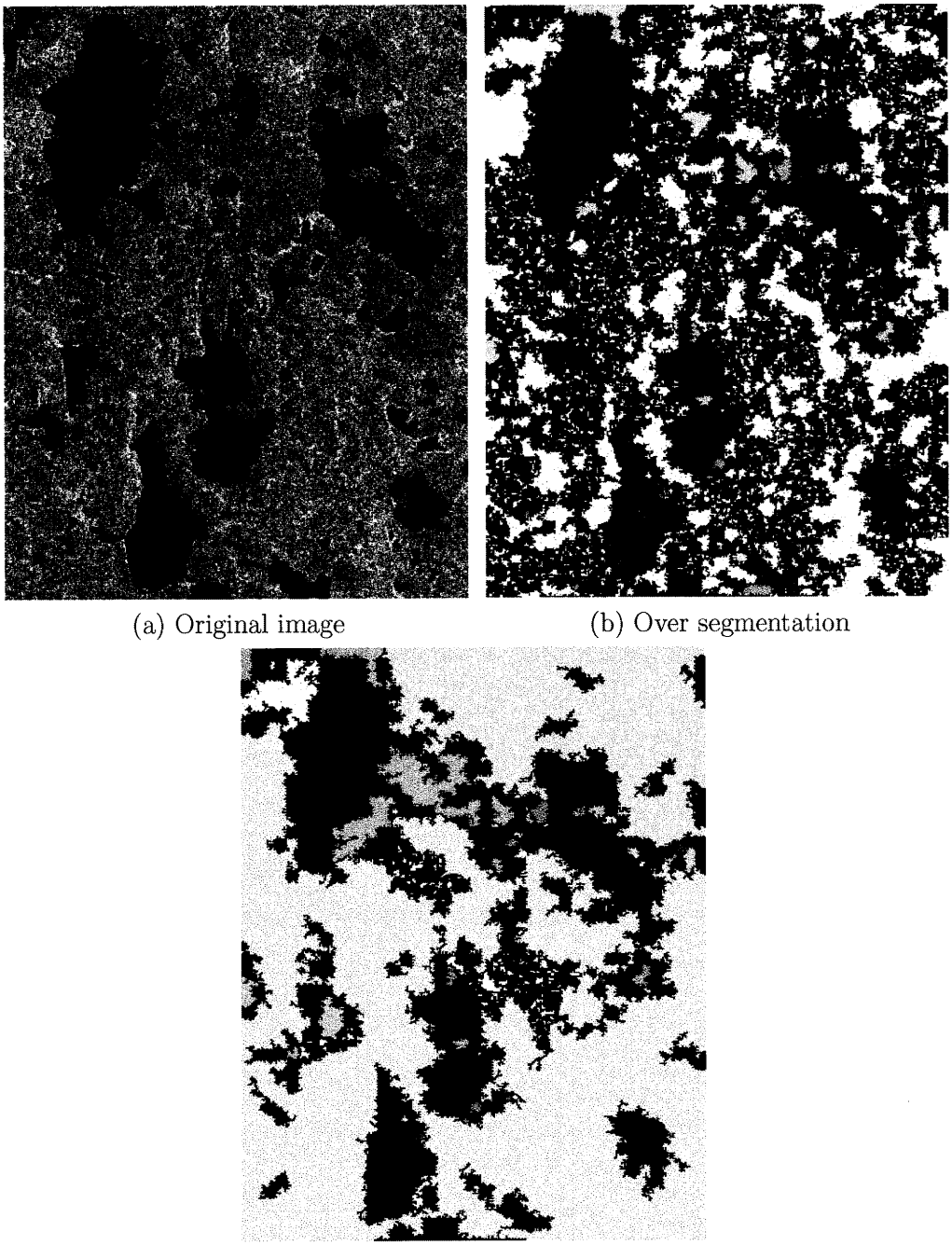

(a) Original image (b) Over segmentation

(c) Under segmentation

Figure 4.3: Using MUM segmentation technique with different parameter values on RADARSAT RS2 image

technique that can be applied to different applications.

4.2.3 Edge-Based Segmentation Methods

Because edges, contours, and boundaries represent many of the intrinsic structures of an image, they are frequently used as features. The main advantages of using the position of the edges in registration is speed to extract and invariance to many types of geometric distortion such as rotation and translation. Edge points, however, are not typically distinguishable; hence they are not appropriate candidates for point matching. Based on edge information, Maitre and Wu (1989) proposed a method for edge matching, and this method has been implemented by other researchers as in [97] [92] [132]. This method need approximate alignment between the image pair not more than five pixels. In general, the use of edges in segmentation requires a region-based similarity measure.

There are four main steps that can summarize the edge detection process [53]. First, noise filtering is important to improve the signal to noise ratio of the image, because edge detectors which use gradient operators are very sensitive to noise. There is always a trade-off between edge strength and noise reduction. This filtering operation can be embedded in the edge detector process or before applying the edge detector. Second, enhancement is used to emphasize the pixels with a significant change in local intensity by using a gradient operator. Third, detection is performed to label the edge points. Finally, estimation is performed to locate the edge with sub-pixel resolution.

Gradient Edge Detectors

These edge detectors work by applying some form of differential operator to

the image. This has the effect of measuring the spatial rate of change of the pixel intensities. Obviously, in the region of edges where the pixel intensities tend to be changing rapidly, there will be correspondingly large values of the first derivative. Edge detectors based on this concept are the Roberts [118], Prewitt [106] and Sobel [44]. Figures 4.4 (b), (c), and (d) reflect the effect of these filters on SAR images. The major difficulty encountered when using the first order gradient-based edge operator in segmentation is the fact that it is difficult to determine the actual location of the edge (i.e. the slope turnover point).

The gradient of image intensity is given by the vector;

$$\nabla f = [\frac{\partial f}{\partial x}, \frac{\partial f}{\partial y}]^t = [G_x, G_y]^t \tag{4.1}$$

and the magnitude and direction of the gradient are:

$$G = \sqrt{G_x^2 + G_y^2} \quad , \quad \Theta = \tan^{-1} \frac{G_x}{G_y} \tag{4.2}$$

This vector valued quantity can be intuitively thought of as pointing in the direction of the steepest descent (or alternatively, the steepest ascent) at each location (x, y). A large squared gradient magnitude indicates the image intensity is changing quickly, signifying that there is an edge. One of the drawbacks of applying the gradient operator is losing information about which side of the edge is brighter. Figure 4.5 demonstrates the effect of first and second order derivatives on a smoothed step edge.

Laplacian (Zero-crossing) Edge Detectors

Typically, Laplacian edge detectors [53] work by approximating the second

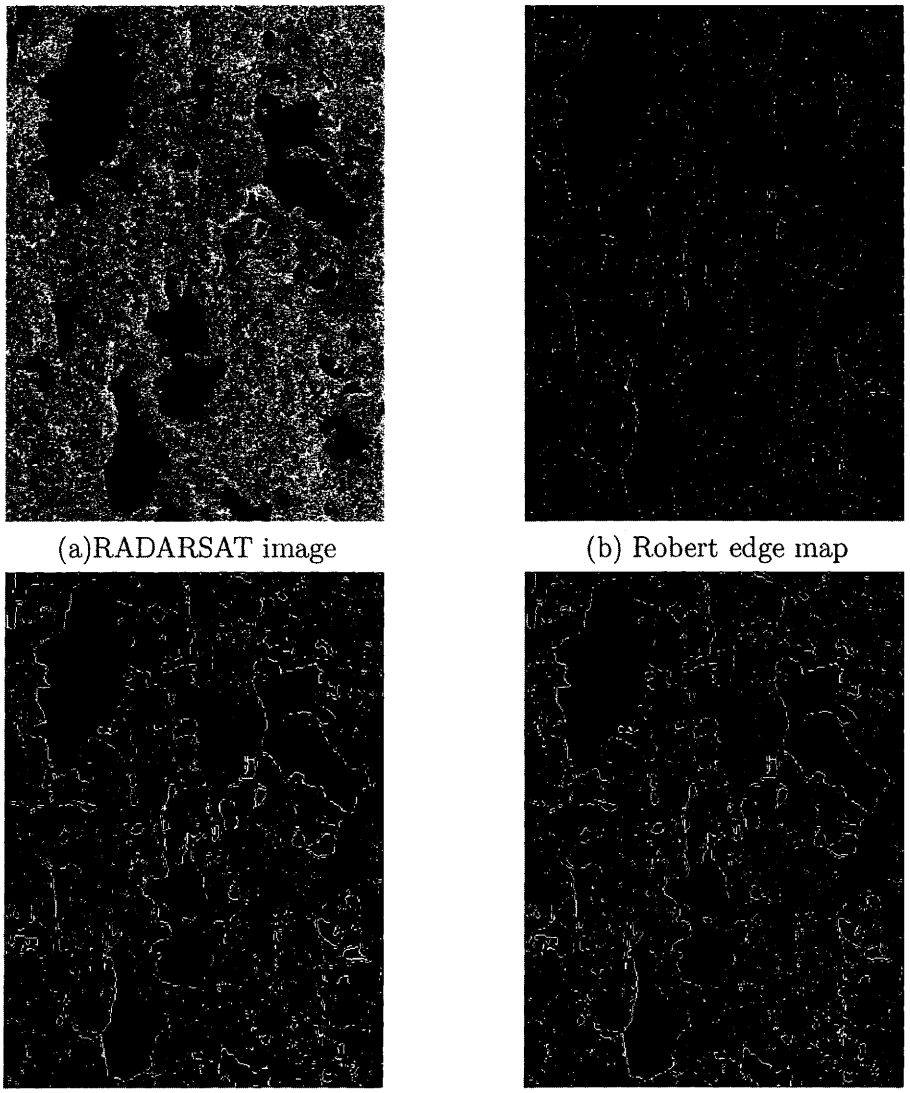

(a)RADARSAT image (b) Robert edge map

(c) Prewitt edge map (d)Sobel edge map

Figure 4.4: Elementary edge detectors

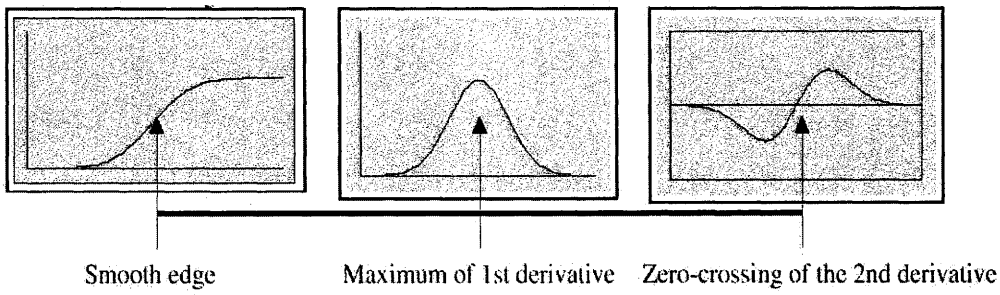

Figure 4.5: First and second derivative operation on smoothed step edge

derivative of the image in localized regions. Edges are characterized by zero-crossings corresponds to the second derivative. Edge detectors from the Laplacian category operate by detecting these zero-crossings. The Laplacian is defined as:

$$\nabla^2 f = \frac{\partial^2 f}{\partial x^2} + \frac{\partial^2 f}{\partial y^2} \tag{4.3}$$

This second derivative operator has the advantage of being isotropic. Moreover, it preserves the sign of the brightness difference across an edge. The Laplacian operator is more effective than the gradient operator for identifying the location of edges [53]. Marr-Hildreth [87] built an edge detector based on the Laplacian operator with some modification, and this will be discussed next.

Marr-Hildreth Edge Detector

The derivative operators previously presented are sensitive to noise. Marr and Hildreth proposed the Laplacian of Gaussian (LoG) edge detector. The idea is to use a Gaussian filter to filter the high frequency noise before enhancement. The Laplacian is then employed for edge detection. The detection criterion is the

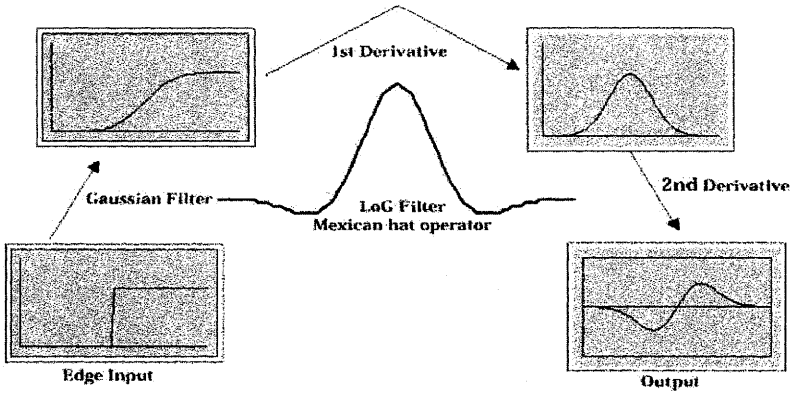

Figure 4.6: Illustration of Marr-Hildreth edge detector

presence of both a zero-crossing in the second derivative and a corresponding large peak in the first derivative. Interpolation can be used to estimate the edge location by employing sub-pixel resolution.

The different phases of the LoG filter (the Mexican hat operator) are illustrated in Figure 4.6. There are two ways to attain the final result. The first is to convolve with the Gaussian filter, and compute the Laplacian. The second is to convolve directly with the Laplacian of the Gaussian filter. The difference between the two Gaussians (DoG) can be used to approximate the LoG filter. The LoG function can be expressed in the following form with zero mean and Gaussian standard deviation σ:

$$LoG(x,y) = \frac{-1}{\pi\sigma^4}[1 - \frac{x^2+y^2}{2\sigma^2}]e^{\frac{-x^2+y^2}{2\sigma^2}} \tag{4.4}$$

The Marr-Hildreth process starts by computing the LoG corresponding to σ. Then, this LoG is applied to the image. The zero crossings of the result are then computed. All zero crossing pixels are labelled as edges. For refinement, there is

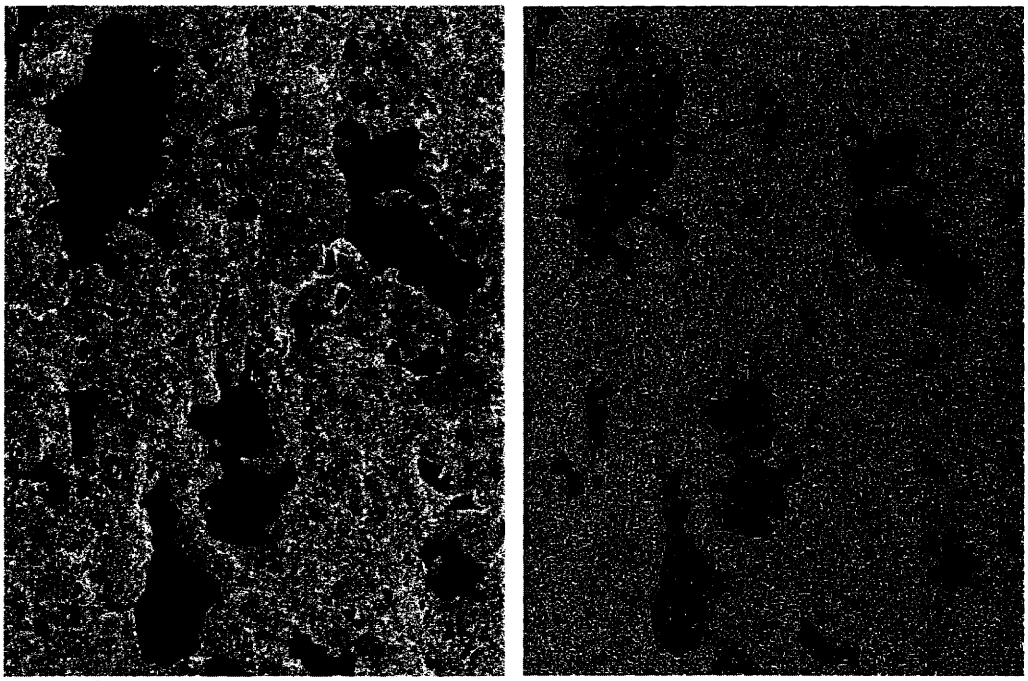

(a) RADARSAT RS2 image (b)Corresponding Edge Map

Figure 4.7: Applying Marr-Hildreth edge detector on a RADARSAT image

one more step that uses a threshold value T. If the gradient magnitude at that Zero-crossing point is above T then it considered an edge.

Zero-crossing in Marr-Hildreth edge detection has the advantage of always forming connected, closed contours. However, connectivity at junctions is always poor, and in general corners are rounded. Also, closed contours come at the expense of localization, especially for the larger values of σ. An application of Marr-Hildreth on RADARSAT RS2 image is illustrated in Figure 4.7.

Canny Edge Detector

The motivation for Canny's edge operator [24] was to derive an edge detector that minimizes the probability of detecting multiple edges, minimize the probability

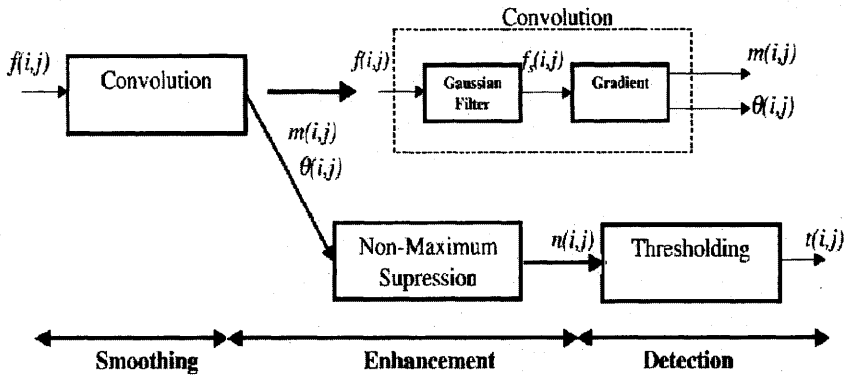

Figure 4.8: The Canny edge detector block diagram

of failing to detect an edge, and minimize the distance of the recorded edge from the true edge location. There is a trade-off between the detection, and the localization. The Canny edge detector works by first Gaussian smoothing the image and then computing the gradient. The squared gradient magnitude is determined and the local maxima of the gradient magnitude that are above some threshold are considered to be edges. This method is called non-maximum suppression. From the Canny block diagram Figure (4.8) the non-maximum suppression thins the ridges of the gradient magnitude $m(i, j)$ by suppressing all the values along the line of the gradient that are not peak values of the ridge. The $n(i, j)$ is then thresholded to reduce the number of false edges. Canny edge detector uses two threshold values on edge strength as a hysteresis mechanism to threshold out weak points but retain weak points with connected edges.

A new implementation of the Canny edge detector, instead of the using Matlab Canny edge detector, used in this research and has presented the best performance both visually and quantitatively, based on measures such as the mean square dis-

tance, error edge map, and signal to noise ratio [5]. The accuracy of Canny edge detector can be controlled by the width of the Gaussian kernel and the two threshold values. The Gaussian smoothing in the Canny edge detector can be used to control the amount of detail that appears in the edge map. Besides, Gaussian smoothing can also be used to suppress noise. Matlab's Canny edge detector sets this two thresholds as T_{max} and T_{min} such that T_{max} is greater than T_{min} by constant factor of forty percent to get rid of edge fragments. This may lead to miss some edges. The new implementation of the Canny edge detector included a parameter (α) that can control the two thresholds to obtain the accurate edges locations automatically. In the new implementation α has value greater than zero and less than one. The value of α is set such that the difference between the two threshold values become high, which leads to more edges to be detected. The level between the two threshold values is defined as: $(threshold\ \ level = \alpha * (T_{max} - T_{min}) + T_{min})$. Figure 4.9 shows a comparison between the implemented Canny edge detector and the Marr-Hildreth edge detector on a synthesized image created for this purpose. Figure 4.10 illustrates the application of the implemented Canny edge detector on RADARSAT RS2 image and Landsat LS2 image. From the Figure 4.10, the produced edge maps visually are more accurate than the other discussed methods.

The proposed RGCE feature extraction process in the ARTSO technique consists of two stages: edge extraction and object extraction. The success of the image registration process of developed ARTSO model depends mainly on feature extraction step. Following the ARTSO flow chart 2.3, the next step after image preprocessing is edge extraction. The edges are extracted using the implemented Canny edge detector.

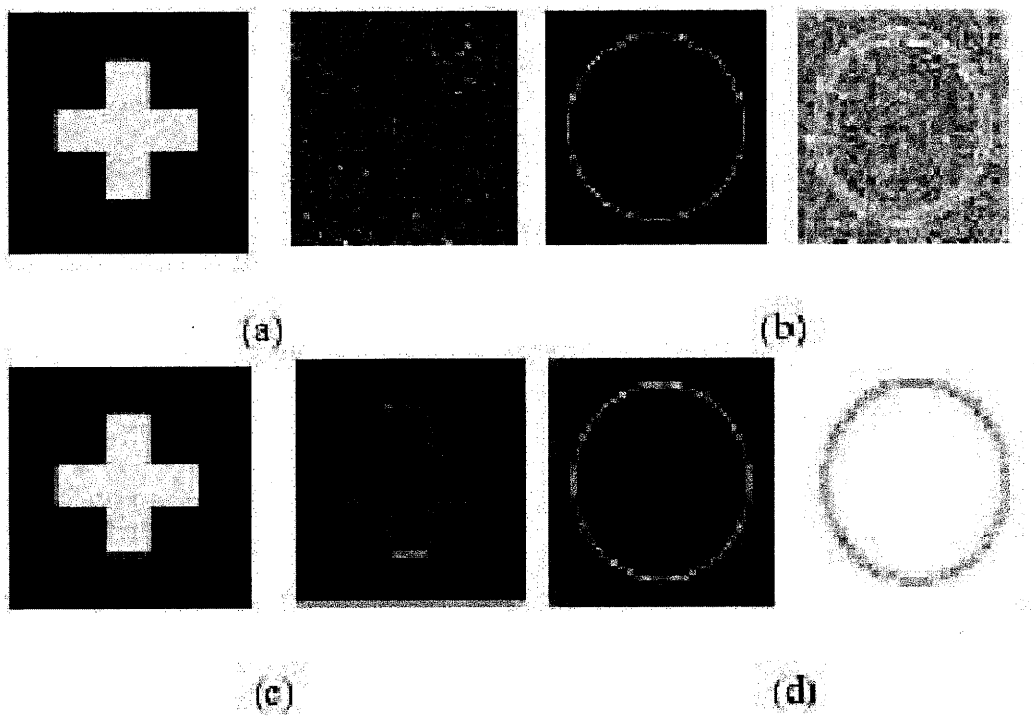

Figure 4.9: A comparison between implemented Canny and Marr-Hildreth edge detectors noisy image
(a) and (b) using Marr-Hildreth , (c) and (d) using implemented Canny

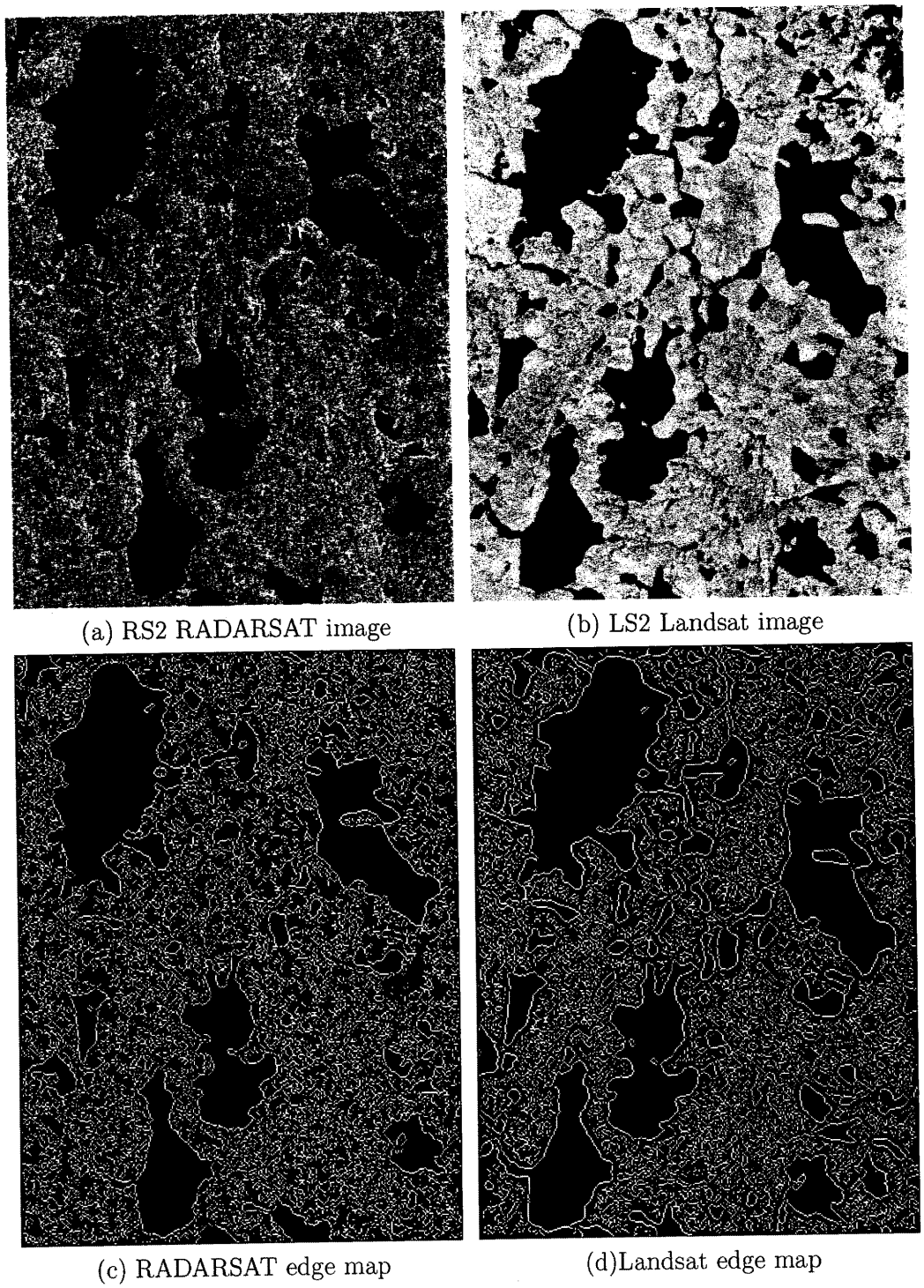

(a) RS2 RADARSAT image (b) LS2 Landsat image

(c) RADARSAT edge map (d)Landsat edge map

Figure 4.10: Applying implemented Canny edge detector on RADARSAT and Landsat images

4.3 New Automatic Technique for Image Segmentation

The objective of this research is to develop an automatic image registration model for SAR and visible-band images. This can be done by automating all the steps of the process. For the previously discussed techniques of feature extraction such as thresholding and segmentation, the most of the existing techniques produce poor results with the given data if the process is automated. For thresholding, the problem of the automatic accurate selection of the threshold value is still under investigation. Due to the complexity of remotely sensed images and the inhomogeneity of gray levels, especially in SAR images, segmentation can be used, but the intervention of the user is still required; otherwise, either under segmentation or over segmentation can occur. This can happen because of the improper selection of the segmentation parameter values. Also, for remotely sensed images, it is hard to determine accurate boundaries.

In light of all these problems, new segmentation techniques are needed to automatically perform feature extraction for remotely sensed images, while producing accurate results.

An algorithm for image segmentation and object extraction is proposed. The newly developed segmentation technique is region growing controlled by an edge map (RGCE). The algorithm depends on the extraction of an accurate edge map which, in this research, is the use of the modified Canny edge detector [5]. Since the contours within the edge map are often incomplete, some form of edge linking is necessary. Morphological operators are applied to obtain closed contours.

Morphological operators are often used with binary images, however, there are versions that can be applied to gray scale images. These operators, which can be either intersections, unions, inclusions or complements, are a combination of erosion and dilation. Dilation increases the size of the boundaries of the region of foreground pixels, that is dilation simply turns pixels "on" according to certain rules between the pixel based on its surrounding neighboring pixels. This operation is necessary for accurate object extraction.

In this thesis, the dilation operation is employed to fill the gaps of the imperfectly closed contours. The edge map is dilated with a window to achieve these closed contours. Figure 4.11 shows the result of edge linking by using a morphological dilation operation which fills in the gaps of the incomplete contours to close all the contours if possible. This technique removes clutters, while linking the gaps of the incomplete contours.

After edge linking, object extraction is performed to identify large homogeneous regions within the closed contours (Figure 4.12). The initial seed of the objects are obtained by scanning the edge map with a square mask its size is set by the minimum size of allowable object to be extracted. When this scanning mask is completely free of edge points then the centre of this mask is add to the seeds. The mask is moved pixel by pixel in X and Y direction of the image edge map. These initial regions are then grown until they meet the original edge location. This process identifies the large edge free regions while ignoring the smaller, less significant features. Figure 4.13 signifies the first step of region growing which represents the seeds of the regions. The regions continue to grow until they reach the original edge contours. Figure 4.14 shows the final extracted objects from RADARSAT

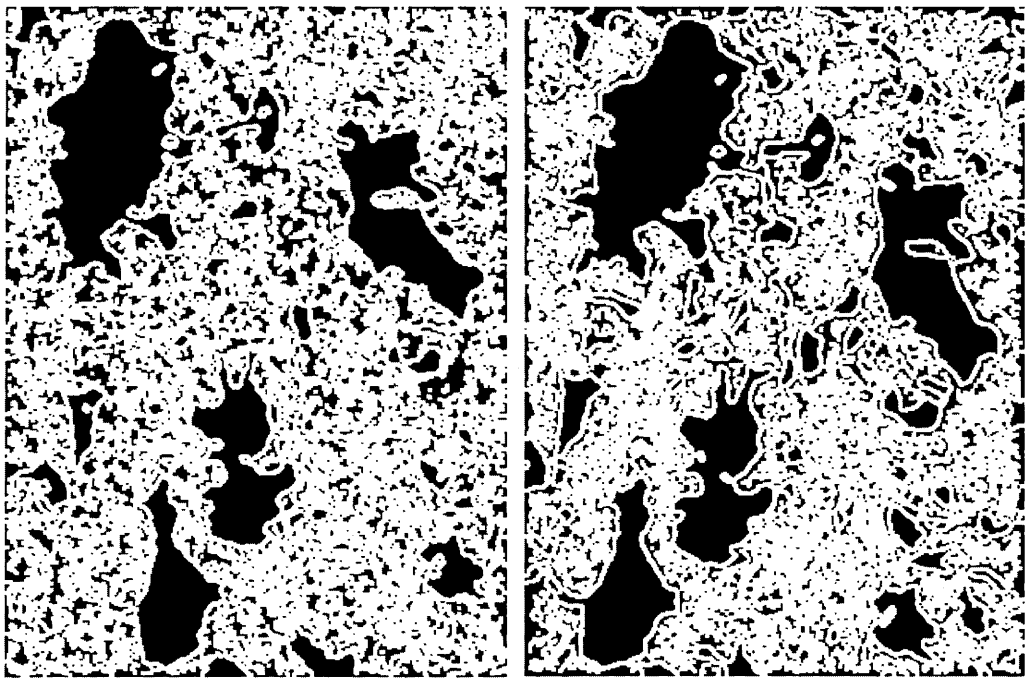

(a) Dilation of RADARSAT edge map (b)Dilation of Landsat edge map

Figure 4.11: Edge linking using morphological dilation operation

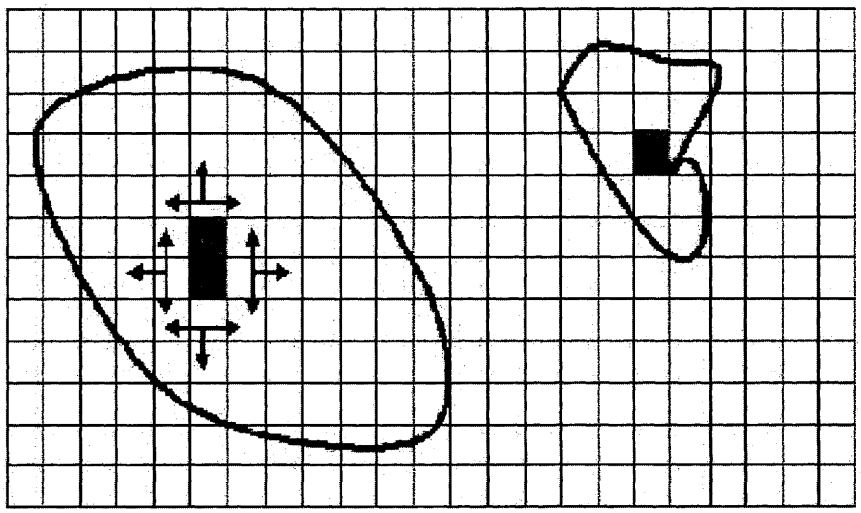

Figure 4.12: Region growing controlled by edge map scheme

and Landsat images by applying the RGCE process. Figure 4.15 reflects the robustness of the proposed technique for object extraction. The extracted objects are superimposed on the edge map.

To show that RGCE algorithm works with different types of images, in addition to the images shown above, RGCE was applied to two different images depicting field with lakes and an urban area. The results of applying RGCE to these two images are depicted in Figure 4.16. The results show that RGCE exhibits a high degree of robustness with different types of images. The original image in Figure 4.16 (a) is SPOT image covering one Kilo metre area in Belgium and CNES copyright, distributed by SPOT Image and produced by VITO Belgium (http://free.vgt.vito.be/). The second image in 4.16 (c) is captured from the website of "region of Waterloo Locator" (http://locator.region.waterloo.on.ca/Locator.htm).

(a)Start objects growing on RS2 image (b)Start objects growing on LS2 image

Figure 4.13: First step of objects growing using RGCM technique

(a)RADARSAT extracted objects (b)Landsat extracted objects

Figure 4.14: Extracted objects from RADARSAT and Landsat images

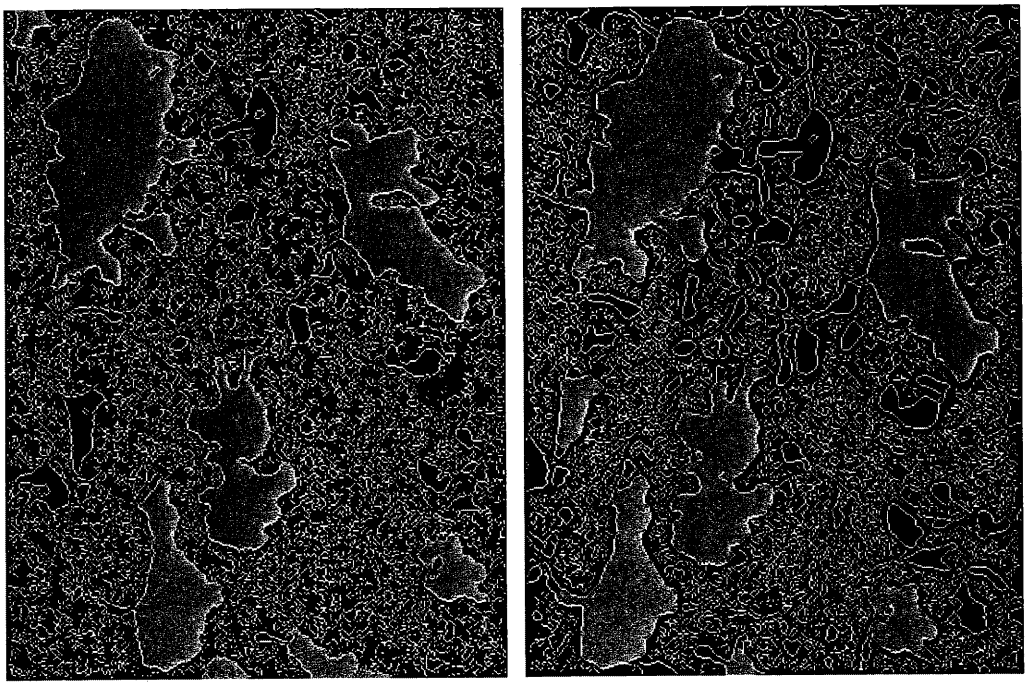

(a) RADASAT image Extracted objects (b) Landsat image Extracted Objects

Figure 4.15: The accuracy of extracted objects

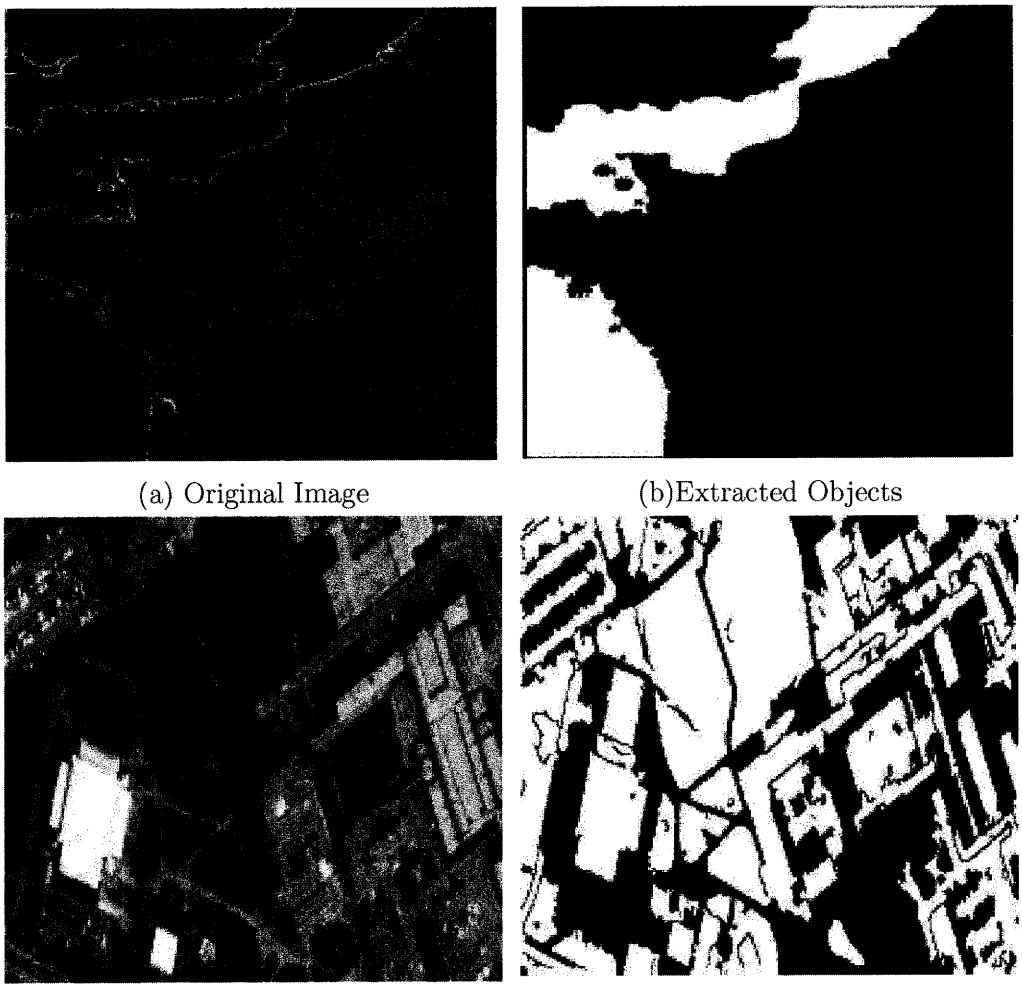

(a) Original Image (b)Extracted Objects

(c) Original image (d)Extracted Objects

Figure 4.16: Applying RGCE technique on different images

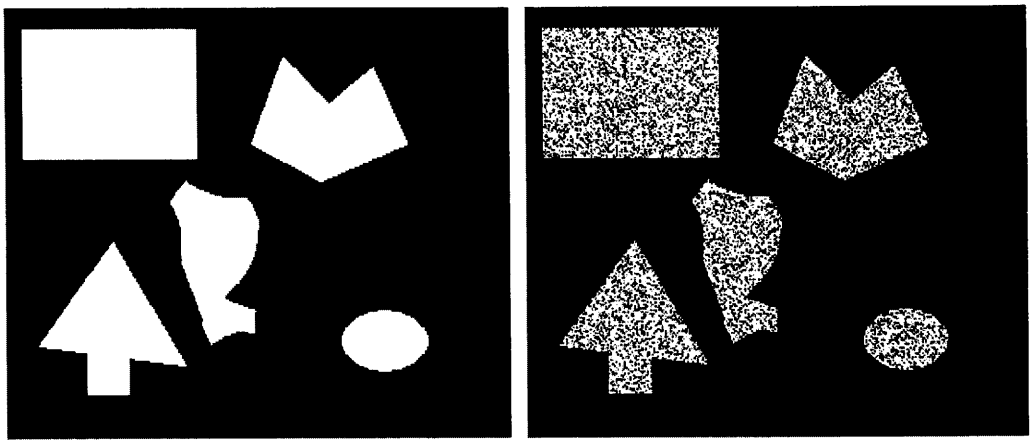

(a) Original synthesized image (b) Synthesized image after speckled

Figure 4.17: Synthesized image and its speckled version

4.3.1 Comparison with other Techniques

To evaluate the accuracy of RGCE object extraction technique, it was compared with two other techniques, thresholding and MUM. To be able to have reference results to which all techniques could be measured, the synthetic image in Figure 4.17 (a), was created. The image contained objects of different shapes and sizes. This image had no noise. Features were then extracted from the created image. The centroid coordinates (X and Y) of each extracted object were calculated.

To use the synthetic image to evaluate RGCE against others, it had to have some speckle noise similar to that found in remote sensing images. The image after adding much speckle noise is shown in Figure 4.17 (b).

The noisy image was then input to RGCE, thersholding and MUM. The mean square errors for the centroids coordinates for each technique were calculated. Table 4.1 shows the results for each technique. Figure 4.18 shows the segmented images

Table 4.1: Objects Extraction Mean Square Error

Technique	Centroid X MSE	Centroid Y MSE	Objects
RGCE	0.2714	0.1329	5
Thresolding	0.4940	0.1908	101
MUM	1.3703	0.7315	87

produced by each technique from which objects were extracted.

From Table 4.1 it can be clearly seen that RGCE resulted in the smallest mean square error (MSE). Many false objects were extracted by thresholding and MUM techniques, while RGCE extracted no false objects at all. This reflects the superiority of RGCE as an object extraction technique compared to the other two segmentation techniques.

4.4 Analysis of the Results

The new region growing controlled by the edge map (RGCE) object extraction method is a very efficient method for object extraction from both SAR and visible-band images, that produces the same level of accuracy, since it is applied on their binary images . One important thing for measuring the efficiency of the RGCE algorithm with respect to time is the selection of the seeds for the region growing. The size of the seed is big (produced from the scanning mask) which speeds up the growing process. To evaluate the RGCE algorithm it is applied on different remotely sensed images (illustrated in the next chapter), and the objects extracted by this technique are much more accurate in shape and dimension than thresholding, homogenous regions, and segmentation techniques. There are no limitations on

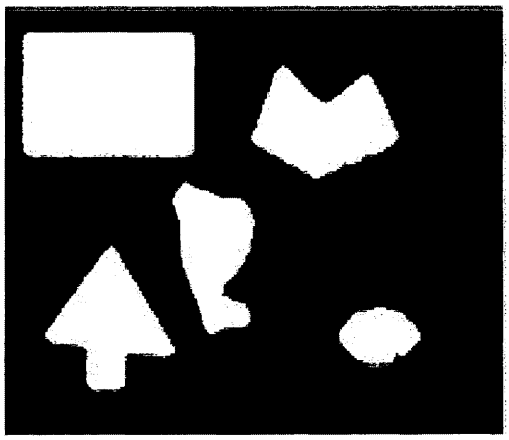

(a) RGCE extracted objects result

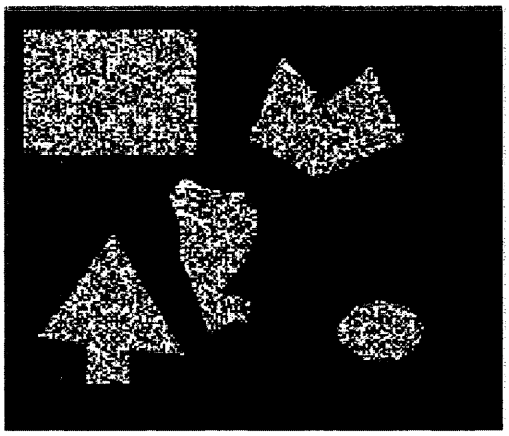

(b) Thresholding extracted objects result

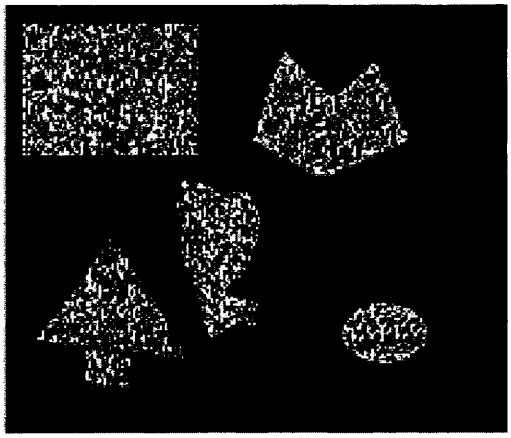

(c) MUM extracted objects result

Figure 4.18: RGCE, thresholding, and MUM extracted objects

shape or dimension of objects to be extracted, but for accuracy very small objects are not considered by setting an appropriate threshold value.

The results of the segmentation using thresholding indicates that the RGCE feature extraction method is more accurate, removes clutter, and retains significant objects. Compared to other segmentation techniques such as MUM, RGCE is more accurate. MUM also needs an operator to set up the parameters while producing under-segmentation or over-segmentation (a lot of clutters or undefined objects).

RGCE solves the problem of the low accuracy of boundary extraction of remotely sensed objects as shown in Figure 4.14 and Figure 4.15. From these Figures, the extracted objects are superimposed onto the edge map and the fit is accurate. RGCE object extraction method proved easy to implement, efficient and accurate.

More analysis about the quality of the extracted objects will be discussed in the next chapter with discussion of object matching process.

4.5 Summary

As explained before, this research effort is mainly concerned with the registration of different types of images acquired from different acquisition systems (SAR and visible-band images). This indicates that a feature-based registration approach is necessary. Feature extraction is a very important task in image registration, especially in feature-based image registration. Successful feature extraction can lead to accurate image registration. This chapter has presented the different algorithms of feature extraction, and a new method for image segmentation. This method can be viewed as region growing controlled by accurate edge map with the following

objectives:

- RGCE extracts as many objects as possible. This leads to a higher accuracy of the matching process.
- RGCE provides high accuracy in terms of the shape and the boundary of the object, which is particularly important in certain applications such as search and rescue and coastal detection.

The edge linking operation reduces the possibility of merging objects, and thus, increases the number of individually detected objects.

Besides preventing the merging of regions, the closed contours edge map ensure that each region is grown within the proper limits which makes for more accurate object extraction.

In the next chapter, object matching process of the extracted objects will be investigated with the use of an evaluation function. The chosen transformation function will be applied using the extracted GCPs to produce the registered image after resampling.

Chapter 5

ARTSO Objects Matching and Registration

5.1 Introduction

After object extraction, the next step in the image registration process is object matching to establish the corresponding GCPs of the two images. In general, the matching process goal is to find the absolute orientation between the input image and the reference image.

In object matching, three choices must be made: the evaluation function to compare between the extracted objects, the transformation model to obtain the geometric difference between the two images objects, and resampling to obtain the geometrically corrected image. Evaluation function selection is one of the essential tasks in object matching. The quality and the sensitivity of the evaluation function determines the accuracy of the matching process.

5.2 Matching Function

For feature-based image registration techniques, the matching process depends on the comparison between extracted features. Of the many image features (points, lines, regions), regions are the best. Many more attributes can be extracted from regions such as perimeter, convex hull, area, solidity, axis length and bounding box, than from points and lines. Matching by utilizing lines and points is possible, but the accuracy of matching may be below the level that can be reached using region. The matching using points and line should have certain approximation of alignment between the reference and the input image not more few pixels to obtain acceptable results of registration [35]. The regions have different attributes that can be used in the matching evaluation function.

There exist two types of evaluation functions that compare similarities of two objects. Distance measure (evaluation function) and a merit function, both involving mainly comparison of pairs of object property values [14]. The distance measure (distance function) is to be minimized and the merit function is to be maximized. In case of the two sets of object attributes, the evaluation function of similarity between objects A_i and B_j is usually defined as the sum of the absolute or square value differences, or even as the square root of the sum of the square value differences of all object attributes.

The image object attributes are computed. The main criterion for selecting these attributes is invariance under linear transformations (translation, rotation, and scaling) and possibly non-linear distortions.

Let set $R = (R_1, R_2, ..., R_{k1})$ *and* $I = (I_1, I_2, I_3, ..., I_{k2})$ such that R and I represent

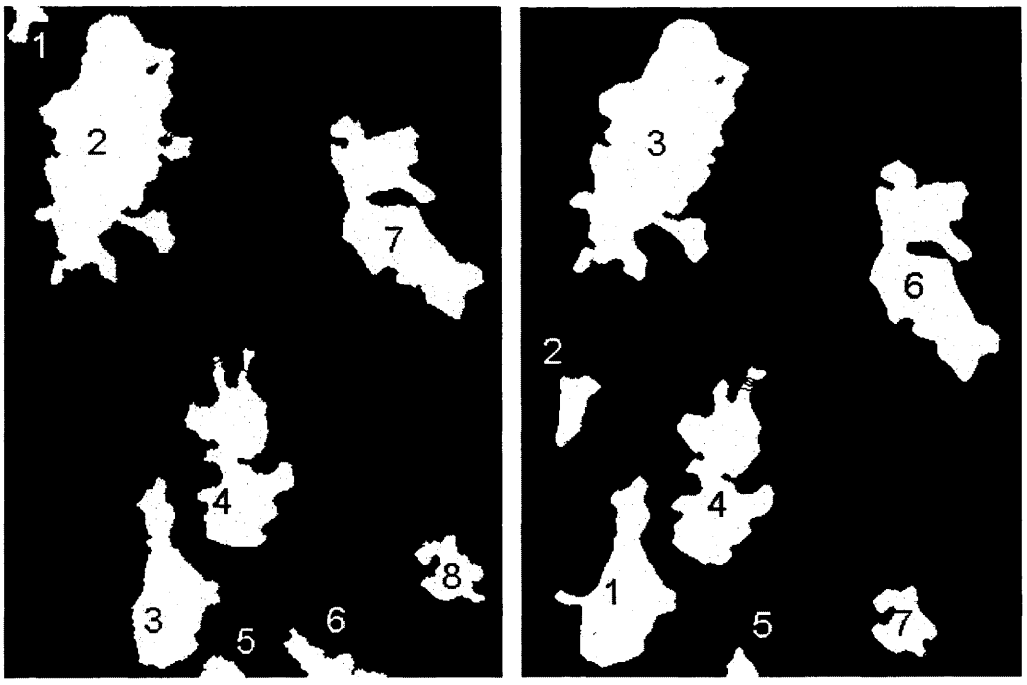

(a)Extracted objects from SAR Image (b)Extracted objects from Landsat Image

Figure 5.1: Extracted objects from RADARSAT and Landsat images before matching

the extracted objects in the reference image and input image, where $k1$ and $k2$ are the number of objects in each (in general, $k1$ is not equal to $k2$). The matching procedure is complete when k objects ($k \leq min(k1, k2)$) are found in both the images being matched.

By applying the feature extraction step of the ARTSO technique, the objects are extracted and ready for matching. Figure 5.1 illustrates the extracted objects from RADARSAT and Landsat images that result from applying the RGCE algorithm. Each object is labelled for separation and the object attributes, such as area, convex hull, and bounding box, are calculated.

Table 5.1: Chosen Attributes Definitions

Object Attribute	Description
Area	The number of pixels belonging to the object
Major Axis Length Minor Axis Length Orientation	Find the ellipse that has the same second order moments as the object. Compute the axis lengths and orientation of the ellipse
Centroid	Graphical center [Mean (rows), Mean(Column)]
Solidity	Area/Convex area
Perimeter	Number of pixels on the object's contour
Bounding Box	Min(Column) Min(Rows) Width Height

The matching process takes the objects attributes that have been calculated to generate a set of GCPs. There has to be a one-to-one correspondence between the GCPs so that each point in the reference image can be matched only with one point in the input image, and vice versa. If a pair of objects are matched, a single pair of GCPs could be generated from the centroids of the objects.

The attributes of the objects which are used in the matching procedure are encoded. They include Area, Centroid, Major Axis Length, Minor Axis Length, Orientation, Solidity, Perimeter and Bounding Box (Table 5.1). An example of some calculated attributes of objects extracted from one of the SAR images is given in Table 5.2.

A cost function for image matching was described by both Morgado and Dowman [92] and Abbasi-Dezfouli and Freeman [2]. However authors found that there were some problems associated with this cost function implementation. This problem was that their evaluation function did not differentiate between the correct matches and the incorrect matches. This occurred because incorrect matches some-

times give a low value for the evaluation function, while correct matches sometimes give high values. Therefore, more information has to be used to improve the matching results.

The evaluation function used by Morgado and Dowman [92] is as follows:

$$\Gamma = \frac{1}{2}|a_1 - a_2| + |p_1 - p_2| + |c_1 - c_2| + |d_1 - d_2| + ... \tag{5.1}$$

where Γ is the value of the evaluation function, a_i is the area of object i, p_i is the perimeter length, and c_i and d_i are the height (in row pixels) and width (in column pixels) of the bounding rectangle.

Dare and Dowman [35] found that there is a problem with this evaluation function. The area component has more influences on the evaluation function than the other components. Therefore, to ensure this is not the case, they proposed to normalized the differences in the components, removing the half value and take the square root for the area component to make sure that all components have the same order and represented as follow.

$$\Gamma = |\frac{a_1 - a_i}{a_1 + a_i}|^{\frac{1}{2}} + |\frac{p_1 - p_i}{p_1 + p_i}| + |\frac{r_1 - r_i}{r_1 + r_i}| + |\frac{c_1 - c_i}{c_1 + c_i}| \tag{5.2}$$

where a, p, r and c represents area, perimeter, centroid row coordinate and centroid column coordinate of extracted patches. There are some comments on Dare and Dowman evaluation function; the square root value for the area component is not appropriate since the square root for a component less than one (due to normalization) is magnified not decreased and the evaluation function should be minimized. The concept that the area component has different order is not accurate since the

area here is represented by the number of pixels that cover this region. Thus, the final form of evaluation function used in this thesis is expressed as follows:

$$Min(C_i) = |\frac{at_1 - at_i}{at_1 + at_i}| + |\frac{bt_1 - bt_i}{bt_1 + bt_i}| + |\frac{ct_1 - ct_i}{ct_1 + ct_i}| + |\frac{dt_1 - dt_i}{dt_1 + dt_i}| + ... \quad (5.3)$$

where at, bt, ct, dt are the attributes of the extracted objects.

Objects A from the first image and B from the second image are selected as a matched pair if the following conditions are satisfied:

(a) $C_{AB} \leq C_{AB'}$ *i.e.* B$'$ includes all the objects with similar shapes to object$A$

(b) $C_{AB} < T$ *i.e.* If the minimum cost function is above the threshold , T (set to 1) , there is no match.

The process is "pairwise exhaustive". Each object in the input image is compared to all objects in the reference image using the evaluation function. Two objects are said to be matched when the value of the evaluation function C is minimal. In the situation where an object from the input image has been matched with two different objects from the reference image, the match with the lowest match function is accepted as the correct one. The result is that all the objects in the input image have been matched, but not necessarily all of the objects in the reference image. This matching process is repeated between the reference image and the input image to ensure matching. Figure 5.2 summarizes the matching procedure.

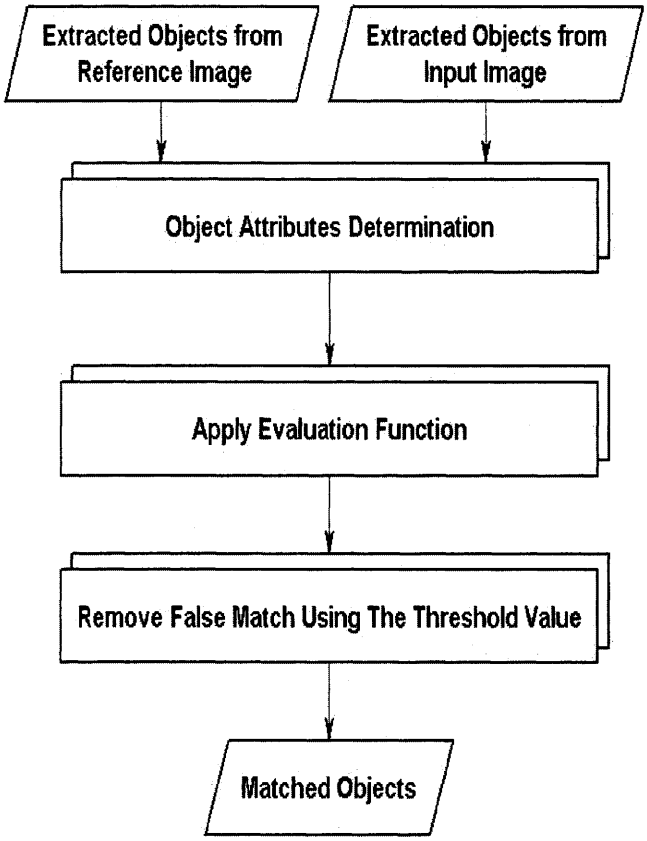

Figure 5.2: Flow chart summarizing the object matching procedure

Table 5.2: Calculated Attributes (in pixels) of Objects in RS2 SAR Image

Object Number	Area	Centroid X Coordinate	Centroid Y Coordinate	Major Axis Length	Minor Axis Length
1	349	158	11.3	31.1	17.5
2	9677	68	92.6	171.6	81.1
3	3525	105.2	386.5	121	46.1
4	4212	148.7	301.5	128.3	52.5
5	275	138.2	437.8	26.5	14.8
6	776	202.1	432.3	62.2	20.7
7	5494	248	140.1	149.3	60.4
8	1077	280.7	373	48.3	33.9

5.3 Object Attributes Determination and Matching

The attributes of the extracted objects from SAR images and Landsat images in Figure 5.1 are determined, and the calculation of the objects attributes is illustrated in Table 5.2. The value of the evaluation function is determined between each object in the reference image and all the objects in the input image to obtain the minimum one. The result of applying the evaluation function C to obtain the best match between the SAR and Landsat objects are presented in Table 5.3. From Table 5.3 and Figure 5.1, it is obvious that the objects in the SAR image are assigned to the objects in the Landsat image correctly. The incorrect matches are removed automatically by the evaluation function threshold. The evaluation function threshold L is set to achieve an accuracy in the matching between objects. If an object in the SAR image is assigned to more than one object in the Landsat image, the minimum evaluation function of the assigned matched objects is chosen

Table 5.3: The Evaluation Function between SAR and Landsat Objects

SAR Extracted Objects	Landsat Extracted Objects						
	1	2	3	4	5	6	7
1	3.6717	2.1099	3.8434	3.8683	2.6919	4.1594	3.2498
2	1.5003	2.9630	0.2552	1.5572	3.7345	1.4628	3.1371
3	0.4865	2.3491	1.8032	0.5003	2.5199	1.3778	1.6117
4	0.6813	2.5184	1.7800	0.3471	2.6757	0.9714	1.7620
5	3.8614	3.0508	4.5870	3.6634	1.4865	4.2114	2.8208
6	3.8613	3.1192	5.0129	3.7097	2.9085	3.8108	2.2898
7	1.6222	3.1422	1.4912	1.1238	3.2290	0.2518	2.0322
8	2.1389	1.7620	3.1983	2.0161	1.9518	2.0162	0.2748

to give the best match.

The centroid of the matched objects is taken as the automatic accurate ground control points as seen in Figure 5.4. The centroid of the object is considered as accurate GCP since it has subpixel coordinate. For this example 5 distributed GCPs collected which can be considered sufficient since the affine transformation need at least 3 distributed GCPs. The matched objects from the SAR and Landsat images are presented in Figure 5.3. For LS1 and RS1 image pair sixteen GCPs are collected as shown in Figure 5.5.

5.4 Image Registration

After discussing the first step of object matching in the previous section, the second and third steps are transformation and resampling to complete the registration pro-

Figure 5.3: Matched objects from RADARSAT and Landsat images

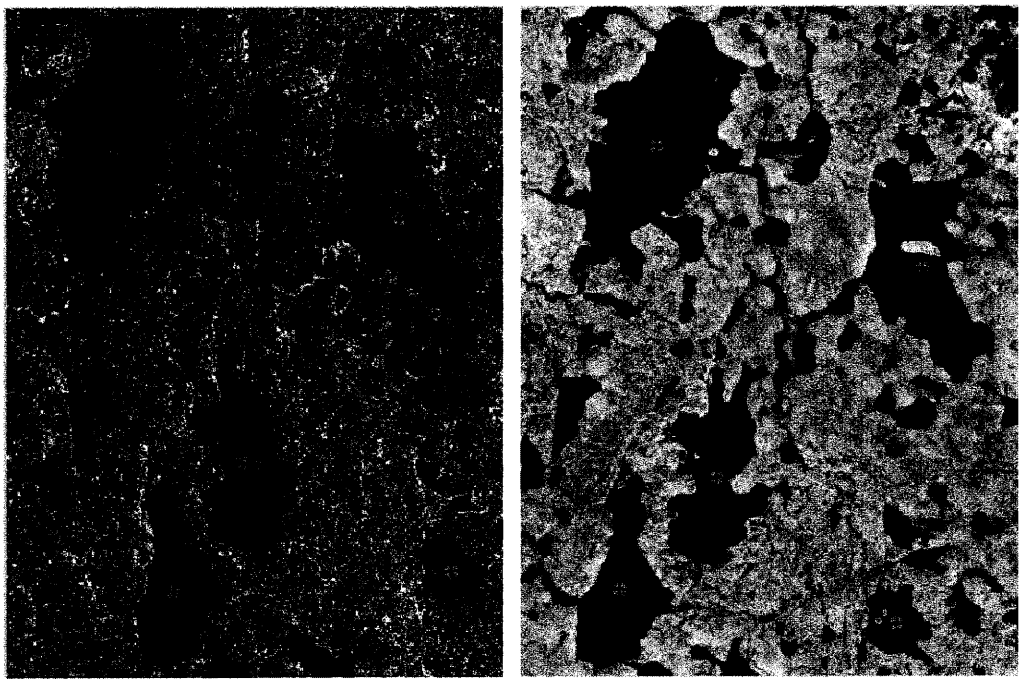

Figure 5.4: Centroid of matched objects on RADARSAT and Landsat Images

cess. The automatic selection of the GCPs has been performed using the evaluation function. Now, the transformation is applied to correct the geometric distortion. The GCPs coordinates are used in the transformation function to determine the transformation coefficients. These coefficients are used to correct the input image with respect to the reference image. In this thesis, the given images assumed to have general linear affine geometric distortion, so the general affine transformation is used to ensure that all affine distortions are considered. The affine transformation is commonly used for registering Earth observation images [34]. However, for images with non-uniform scaling and shearing, the affine transformation will not preserve angles or lengths. For each image pair, the affine coefficients are determined and applied to the input image to obtain the registered image pixels coordinates, such that, for each pixel (X', Y') in the reference image, the (x, y) pixel coordinates of the registered image can be determined as follows:

$$X' = \grave{a}x + \grave{b}y + \grave{c}$$

$$Y' = \grave{d}x + \grave{e}y + \grave{f}$$

where $(\grave{a}, \grave{b}, \grave{c}, \grave{d}, \grave{e},$ and $\grave{f})$ are the general affine transformation coefficients that represent the different distortions. The determined coefficients from LS1 and RS1 image pair, LS2 and RS2 image pair and LS3 and RS3 image pair are illustrated in Table 5.4.

From this table, it can be noticed that the image pairs have different rotation, scaling and the translation is significantly not small. These affine coefficients were used to register the image pairs.

The last step of image registration is resampling. One of the resampling technique is applied to obtain the registered image. The registered image after trans-

Table 5.4: Determined Affine Coefficients

Coefficient	LS1 and RS1 images	LS2 and RS2 images	LS3 and RS3 images
$\grave{a}$	0.9879	0.9793	0.9465
$\grave{b}$	0.1871	0.2034	0.1759
$\grave{c}$	-68.4868	-35.0536	-18.0825
$\grave{d}$	-0.1786	-0.1969	-0.1940
$\grave{e}$	0.9862	0.9834	0.9575
$\grave{f}$	52.4152	19.1498	61.7672

formation and resampling is given in Figure 5.5 using cubic resampling.

5.5 ARTSO Experimental Results

The application of the ARTSO technique to several image pairs has been examined. Each image pair consists of a Landsat image as a reference image, and a RADARSAT image as an input. The RADARSAT image must be registered. Figures 5.6, 5.7 and 5.8 show the results of applying the ARTSO technique to these image pairs. From these figures it can be seen that the RGCE feature extraction method accurately extracts objects from these images. The application of the object matching evaluation function leads to successfully generating the GCPs in the images automatically. The results demonstrate the accuracy of the proposed ARTSO technique using the given images.

Analyzing the available data sets and applying the ARTSO technique on the data reveals the following.

First, from the image pairs, it can be recognized that the two images do not exactly cover the same area nor have exactly the same objects exactly . The

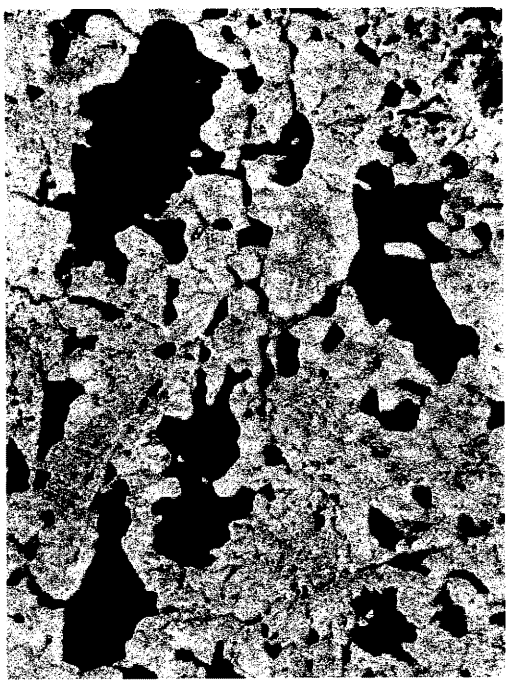

(a)Reference Landsat Image (LS2

(b)Input RADARSAT image (RS2)

(c)Registered RADARSAT image

Figure 5.5: Original reference and input images and the registered image

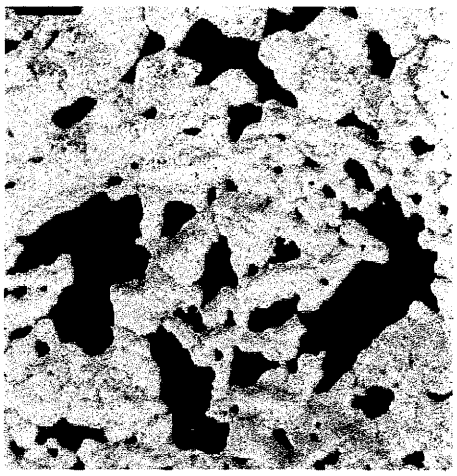

(a)Reference Landsat image LS1

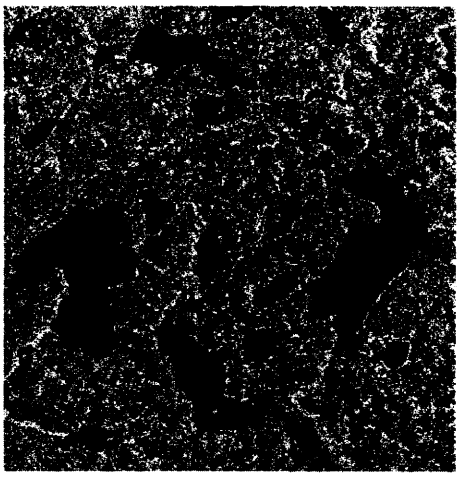

(b)Input RADARSAT image RS1

(c)Landsat edge map

(d)RADARSAT edge map

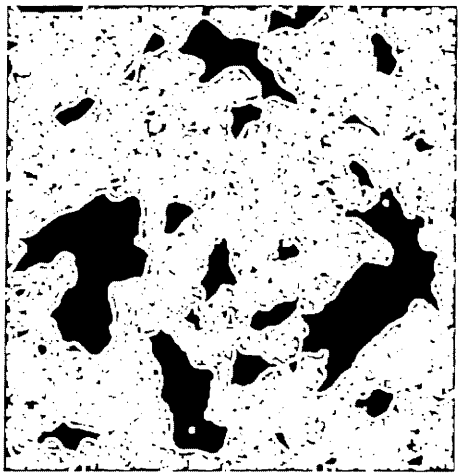

(e)Dilated Landsat edge map

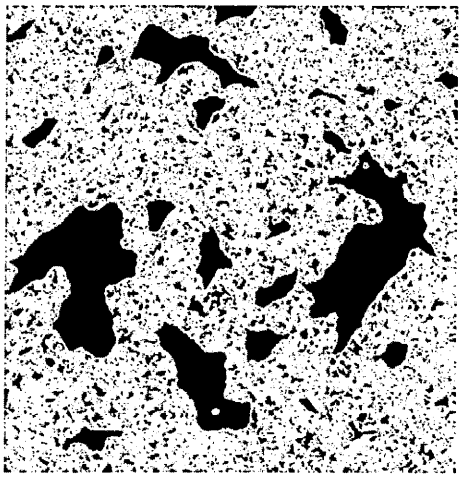

(f)Dilated RADARSAT edge map

(g)Extracted Landsat objects

(h)Extracted RADARSAT objects

(i)Matched Landsat Objects

(j)Matched RADARSAT objects

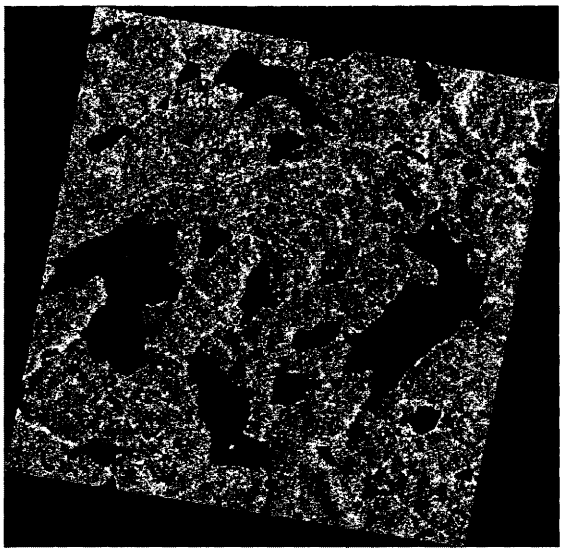

(k)Registered RADARSAT RS1 image

Figure 5.6: Applying ARTSO on Landsat LS1 and RADARSAT RS1 images

images must have visually apparent objects to apply any automatic registration system. Next, the number of objects extracted from the RADARSAT images are not equal to the number of objects extracted from the Landsat images. Thirdly, the translation in the x and Y directions and the rotation are visually clear, which allows the efficiency and the quality of the developed registration process to be measured. The newly developed system can be applied on different data sets such as visible-band image pairs which is even easier than its application to SAR and visible-band image pairs. To verify that, an LS2 reference image is rotated and shifted to become input image and the ARTSO is applied to reference image LS2 and the shifted and rotated LS2 image. The result is shown in Figure 5.10. The distorted image is perfectly registered to the reference image. Another example is illustrated in Figure 5.11. The LS2 image was rotated by 90 degree to prove that

(a)Reference landsat image LS3

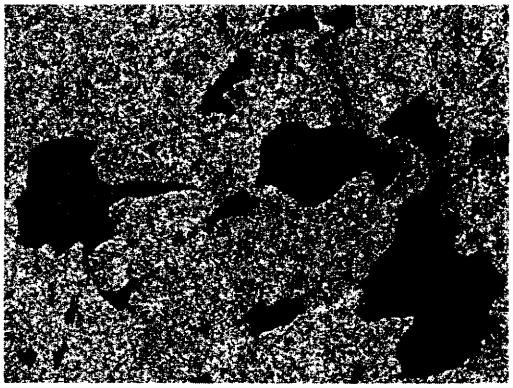

(b)Input RADARSAT image RS3

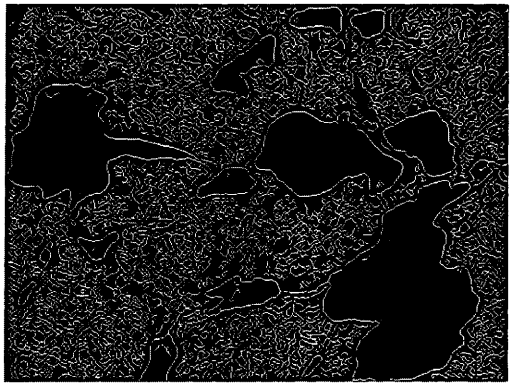

(c)Landsat edge map

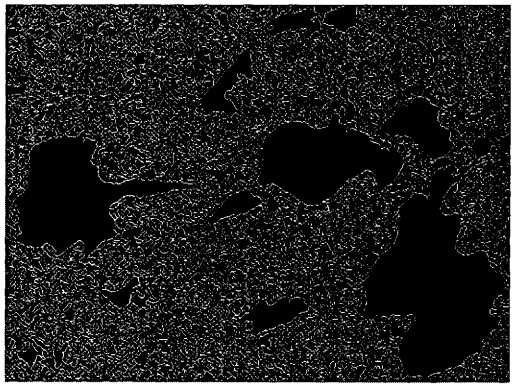

(d)RADARSAT Edge Map

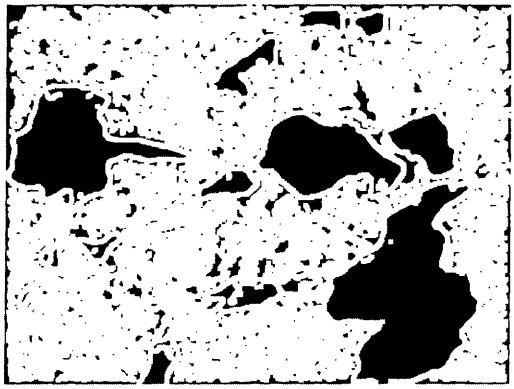

(e)Dilated Landsat edge map

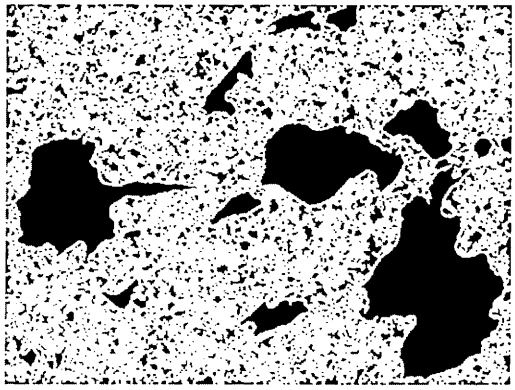

(f)Dilated RADARSAT edge map

(g)Extracted Landsat objects

(h)Extracted RADARSAT objects

(i)Matched Landsat objects

(j)Matched RADARSAT objects

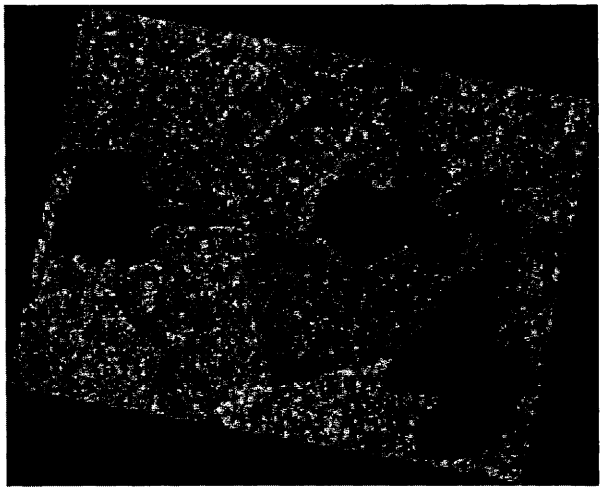

(k)Registered RADARSAT RS3 image

Figure 5.7: Applying ARTSO on landsat LS3 and RADARSAT RS3 images

ARTSO technique can handel the gross distortion in rotation.

Judging the accuracy of the registration process is difficult. The registration accuracy is usually accessed by the root mean square error [81]. Another measure is using the variance component and the variance-covariance matrix. For the evaluation purpose, a quantitative evaluation to the accuracy of the ARTSO is illustrated in Table 5.5 and Table 5.6. Table 5.5 shows the error difference in X and Y directions between the input image and the reference image before the registration and the distance error difference in X and Y directions between the reference and the registered images.

For a comparison between the manual image registration and the developed ARTSO model accuracy, SAR and Landsat images are registered manually by different operators and the RMSE is measured for all trials. The RMSE range was between two and four pixels with selection of enough distributed GCPs collected

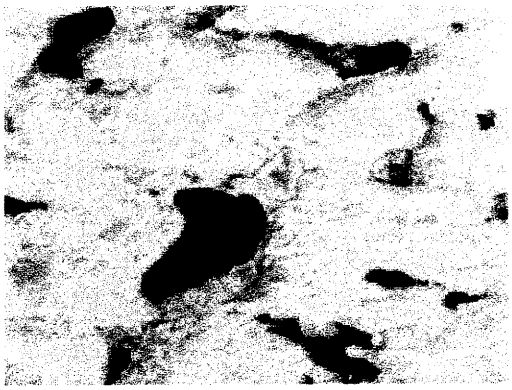

(a)Reference Landsat image LS4

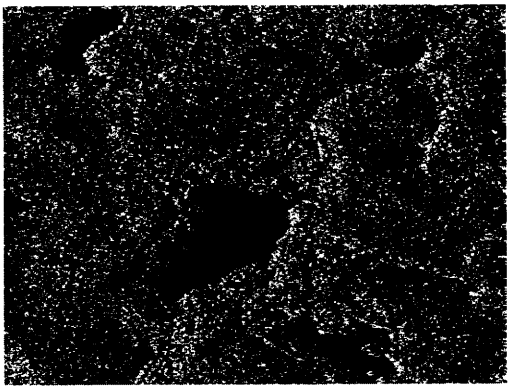

(b)Input RADARSAT image RS4

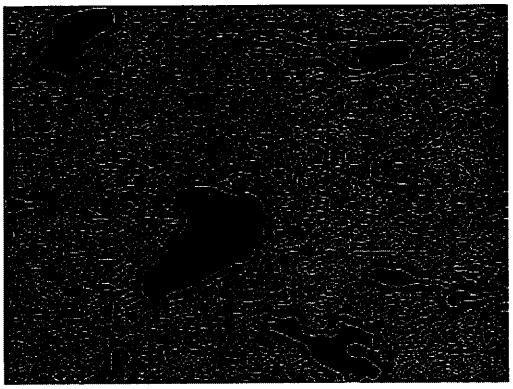

(c)Landsat edge map

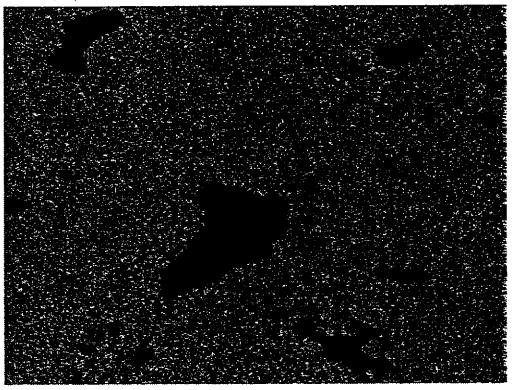

(d)RADARSAT edge map

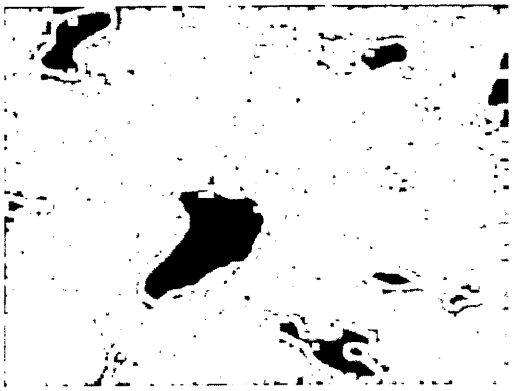

(e)Dilated Landsat edge map

(f)Dilated RADARSAT edge map

(g)Extracted Landsat objects

(h)Extracted RADARSAT Objects

(i)Matched Landsat objects

(j)Matched RADARSAT objects

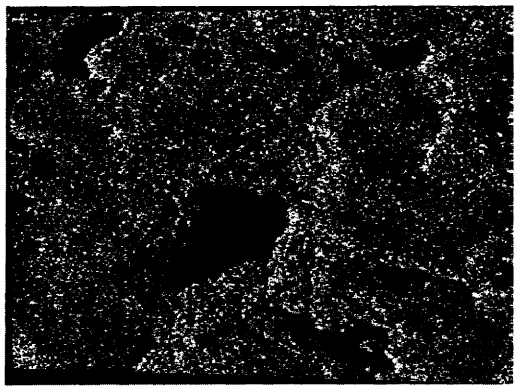

(k)Registered RADARSAT RS4 image

Figure 5.8: Applying ARTSO on Landsat LS4 and RADARSAT RS4 images

Table 5.5: The Evaluation of Registration of RADARSAT and Landsat Images

Landsat LS2 GCPs		RADARSAT RS2 GCPs		Registered image R		Error between LS2 and RS2		Error between LS2 and R	
X	Y	X	Y	X	Y	X	Y	X	Y
22.8285	293.581	37.2101	293.815	23.0205	294.0764	14.1896	0.234	0.192	0.4954
37.7836	219.4899	80.672	208.8169	36.4904	220.7093	42.8884	10.673	1.2932	1.2194
167.3544	81.0704	179.9401	47.5106	166.8622	81.6385	12.5857	33.5598	0.4922	0.5681
151.6274	315.5244	212.7146	280.3544	151.8853	315.7571	61.0872	35.17	0.2579	0.2327

Table 5.6: The Evaluation of the Registration of Landsat and Synthesized Landsat Images

Landsat LS2 GCPs		RADARSAT RS2 GCPs		Registered image R		Error between LS2 and RS2		Error between LS2 and R	
X	Y	X	Y	X	Y	X	Y	X	Y
22.8285	293.581	37.2101	293.815	23.0205	294.0764	14.1896	0.234	0.192	0.4954
37.7836	219.4899	80.672	208.8169	36.4904	220.7093	42.8884	10.673	1.2932	1.2194
167.3544	81.0704	179.9401	47.5106	166.8622	81.6385	12.5857	33.5598	0.4922	0.5681
151.6274	315.5244	212.7146	280.3544	151.8853	315.7571	61.0872	35.17	0.2579	0.2327

by different operators. The manual image registration result between RS2 and LS2 image pair is shown in figure 5.9.

These results are evident that the automatic registration process sometimes is very efficient than the manual method. This is depending on the nature of the images to be registered. In our case the automatic registration model gives more accurate results since the error is sub-pixel in most cases.

From Table 5.6, the synthesized Landsat image LS2 as an input image is registered to the reference LS2 Landsat image and the accuracy of registration is presented. Table 5.5 and Table 5.6 present how the developed system has high accuracy and proves that the ARTSO system can be applied on different image types.

In Chapter 4 it was shown that the object extraction process (RGCE) of ARTSO was superior to thresholding and MUM. Since thresholding and MUM exhibited a larger mean square error than RGCE (Table 4.1), the obtained GCPs are not

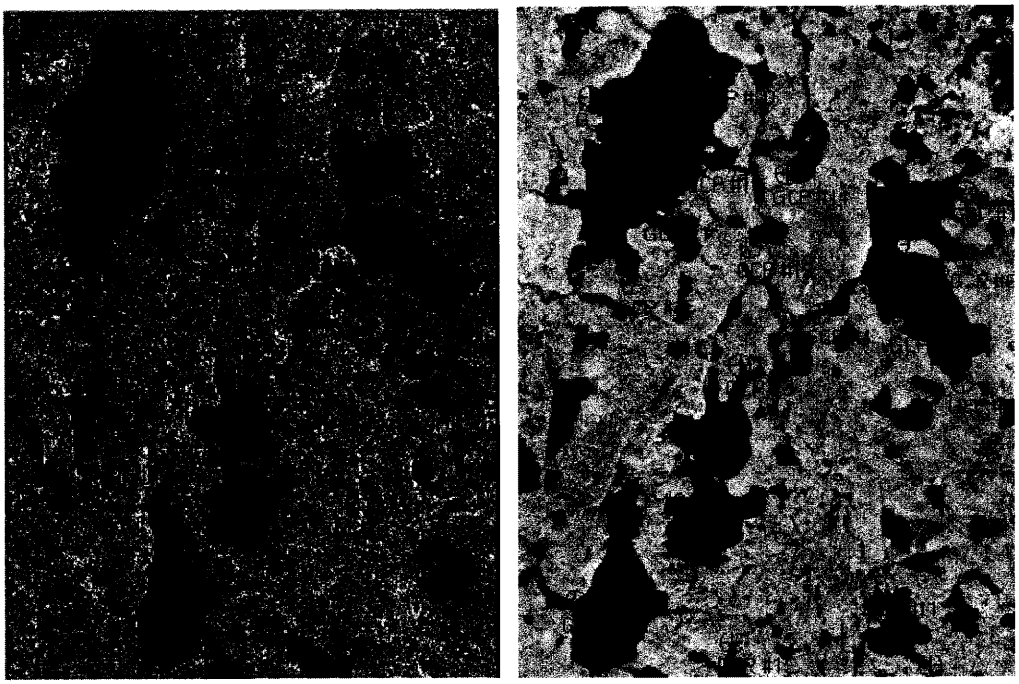

(a)Input RADARSAT image RS2 (b)Reference Landsat image LS2

(c)Manually registered RS2

Figure 5.9: Manual registration between RADARSAT RS2 and Landsat LS2 images

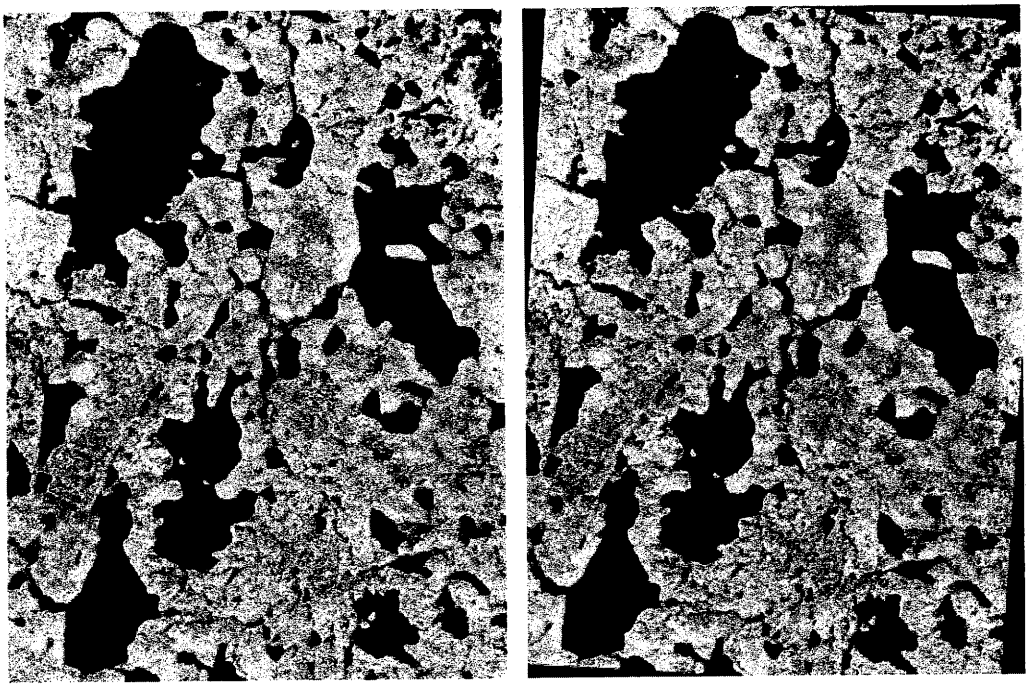

(a)Original Landsat image LS2 (b)Synthesized Landsat LS2

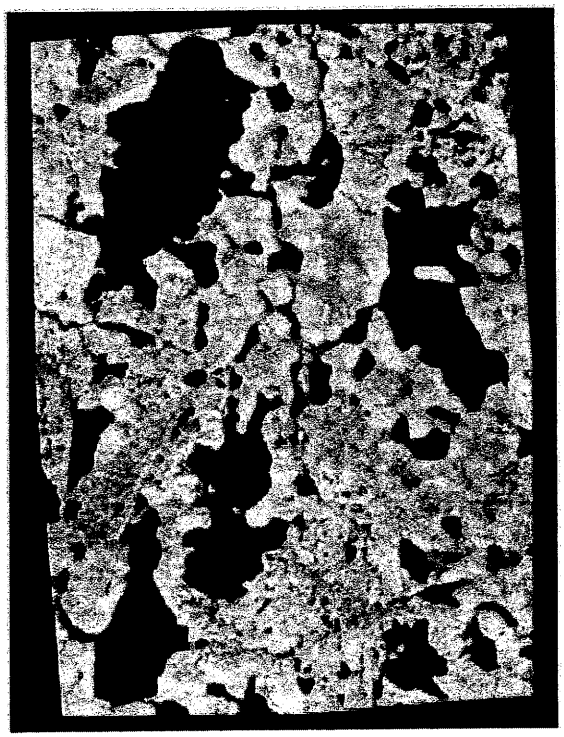

(c)Registered synthesized LS2 image

Figure 5.10: Applying ARTSO on Landsat LS2 and a synthesized LS2 images

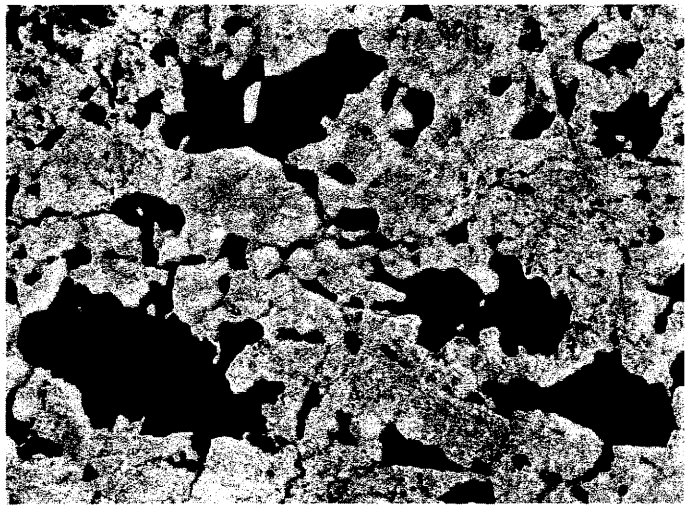

(a)Rotated LS2 by 90°

(b)Extracted objects from Rotated LS2 by 90°

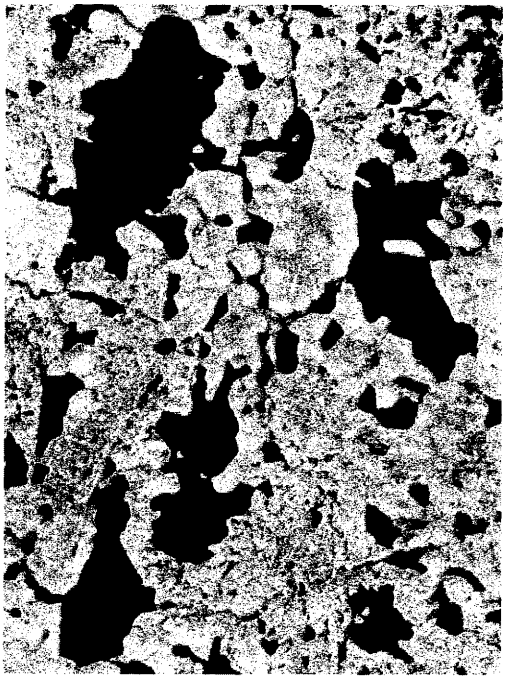

(c)Original Landsat image LS2

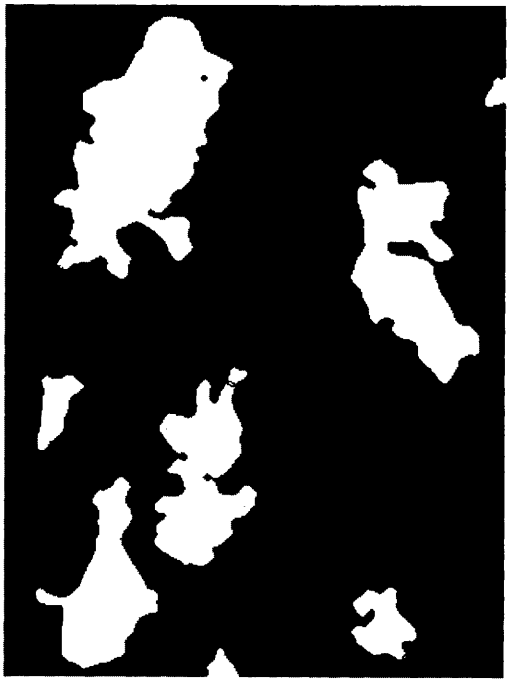

(d)Extracted objects from LS2 image

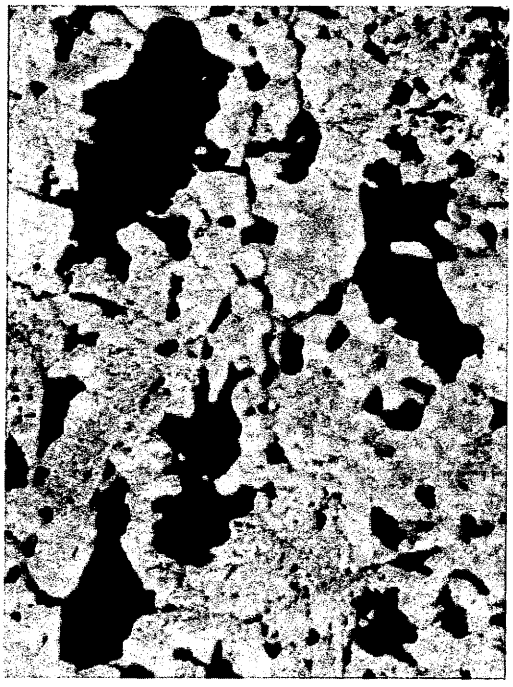

(e)Registered rotated LS2 image

Figure 5.11: Applying ARTSO on image pair has gross rotation distortion

expected to be as accurate as those obtained based on RGCE. Knowing that the matching process is based on the determined GCPs, it is obvious that the matching based on the flawed GCPs obtained from threshoding and MUM is going to be less accurate than that done by RGCE.

5.6 Discussion

This chapter has presented methods for matching objects extracted from SAR and visible-band imagery. The achieved results have been shown. A feature matching algorithm based on the RGCE feature extraction algorithm discussed in the previous chapter was presented. It was taken in consideration while designing the feature extraction that it should produce accurate and reliable results automatically, which is very important in the automatic image registration system. The object matching method using the evaluation function, matches all the objects extracted from input image to the objects extracted from the reference image for the given data. Using the evaluation function, all multiple matches can be removed. The affine transformation is applied using the automatically extracted GCPs to calculate the affine coefficients to transform the input image to the reference image grid. The perfect matches were arrived from the well selection of the object attributes used in the evaluation function. These attributes are invariant to translation, rotation, and scaling. This allows ARTSO technique to be more reliable, since it can handle a wide range of geometric differences between the input image and the reference image.

To further increase the matching accuracy, the algorithm rejects matches that

result in an evaluation function value that exceeds a certain threshold. The GCPs from the non-considered objects are not used in the calculation of the transformation matrix coefficients.

Chapter 6

ARVS Model and Applications

6.1 Introduction

The ARTSO technique described in the previous chapters requires that the objects in the reference and input images be extractable. This means that the signal to noise ratio is high and the regions are visually apparent. In this case the regions can be extracted as approximately closed contours. In some cases, the closed boundaries of objects may not be extractable due to the poor quality of the original image or the incomplete capturing of some of the objects in the image.

In this chapter, an automatic technique for handling these exceptional cases is proposed. It is called the automatic registration of visible-band and SAR images (ARVS). One of the examples where ARVS algorithm proves very useful is with aerial InSAR and photo images. The reason is that InSAR images are typically of a relatively poor content quality which makes extracting closed edge objects very difficult in many cases, even if these objects do exist in the image (e.g., buildings

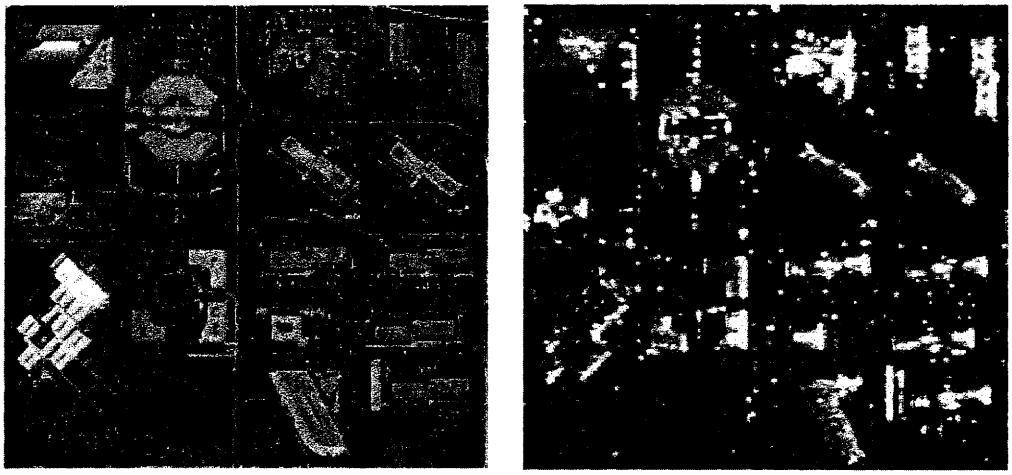

(a)Reference aerial image (b)Input InSAR image

Figure 6.1: Reference aerial optical image and input aerial InSAR image

and field boundaries) as shown in Figure 6.1.

6.2 Automatic Registration of Aerial Visible-Band and InSAR images

The ARVS model consists of two main parts: feature extraction and feature matching. For feature extraction, since the gray level characteristics are totally different between the InSAR image and visible-band image, gray levels intensities are not considered for similarity measuring. Considering the characteristics of aerial InSAR images and aerial photo images (Figure 6.1), it was not easy to decide which kind of features need to be extracted and matched. Applying a segmentation method is not suitable for feature extraction. The problem with the segmentation was the low quality of the InSAR images that prevent the production of an acceptable level

of segmentation. Finally, the edges are employed as the features in the feature extraction process.

Usually, for measuring the similarity between the edge maps, the cross correlation technique is used. However, one drawback of this technique is that it only handles translation errors. This is definitely not suitable for use with remotely sensed images which are typically characterized by other types of geometric distortions as well. Invariant moments [68] are selected as a similarity measure in the ARVS model to handle the different types of geometric distortions in the image pairs.

The ARVS model involves the following steps and is illustrated in Figure 6.2:

Noise removal: The main objective of this step is to reduce image noise without significantly modifying the pertinent features. The techniques used for noise removal have been discussed in Chapter 3. Because the used InSAR images in this thesis are the combination of two phase images, so the noise model is characterized by additive noise model [79] and simple mean filter are applied to reduce the effect of noise in InSAR images.

Image detail selection: Due to the high level of detail in optical images and low level of detail in SAR images, this step is very important for the success of this algorithm. This procedure controls the extraction of high detail from optical images to create a balance between the extracted edges from optical and SAR images to increase the accuracy of the matching step.

Edge extraction: Different edge extraction algorithms are considered as described in Chapter 5. The implemented Canny edge detector is considered the best in this case.

Search window selection: The edge maps of both images are divided into rectangular sub-images of equal size.

Affine invariant moments (AIM) determination: Hu [68] provided a set of moments called invariant moments. This set of moments are invariant to translation, rotation, and scale. They are applied to binary images which represent the edge map in the ARVS model.

Sub-image matching: By an exhaustive comparison between the AIMs of the sub-images of the reference image and input image, the ARVS algorithm obtains the best matched sub-images.

Image channel selection, sub-image separation, and AIM determination are discussed in more detail in the following subsections.

6.2.1 Image Detail Selection

Edge maps from visible-band and InSAR images are extracted. In visible-band images, due to the high signal to noise ratio, a large number of edges can be extracted; due to the low signal ratio in InSAR images, a small number of edges can be extracted. As a result, a method to reduce the number of extracted edges from visible-band images is suggested. A Gaussian smoothing filter in frequency domain with a preferred cut-off frequency σ was applied to the InSAR image as illustrated in Figures 6.3, 6.4, 6.6 and 6.7. From these figures, it is evident that the edge numbers and quality can be controlled by the cut-off frequency σ. With a high σ, more details can be extracted and vice-versa. The accepted details from the InSAR image are obtained first using different σ in the frequency domain. The corresponding details from the visible-band image is performed automatically by using the obtained σ

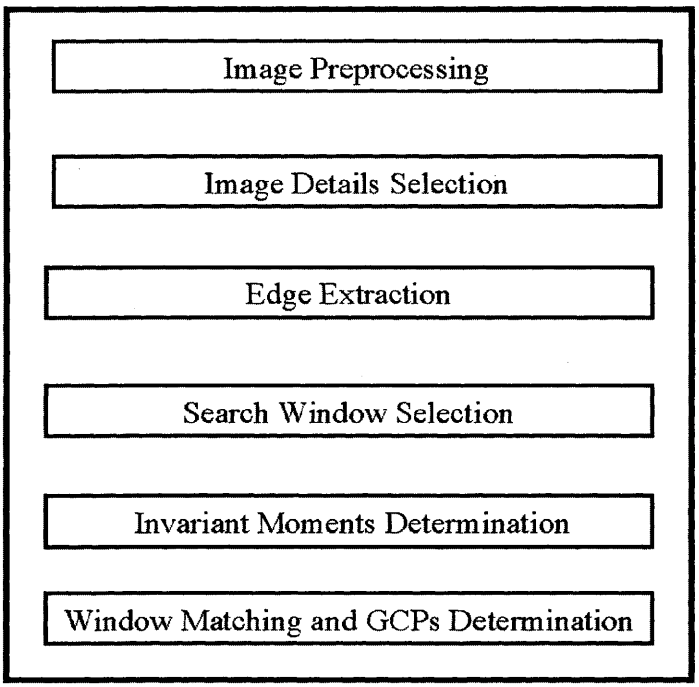

Figure 6.2: Automatic registration of visible-band and InSAR images ARVS algorithm

from InSAR image as the initial σ. The algorithm then proceeds by incrementing this σ by one each time and determining the corresponding windows AIMs between the two images to be minimized.

The edge maps are extracted using the implemented Canny edge detector. The implemented Canny edge detector is applied on the smoothed images, Figure 6.5 and Figure 6.8.

6.2.2 Search Window Selection

The features to be compared between the reference image and the input image are the edge map contents inside rectangular sub-images with the size (MxN). The image edge map is divided into equal rectangular sub-images. The two images should be approximately registered for few pixels to apply this method. Figure 6.9 exhibits the edge maps after being partitioned.

6.2.3 Invariant Moments Determination

The moments provide an important representation to the shape of the objects. Here, the use of moments as features of an object f(x,y) is presented. The moments are derived from raw measurements and can be used to achieve scale invariant and translation (or position) invariant but the rotation is variant [68].

The centralized moments are translation invariant and can be normalized with respect to changes in scale. However, to enable an invariance to rotation, the moments require reformulation. Hu [68] derived invariant moments computed from normalized centralized moments up to order three.

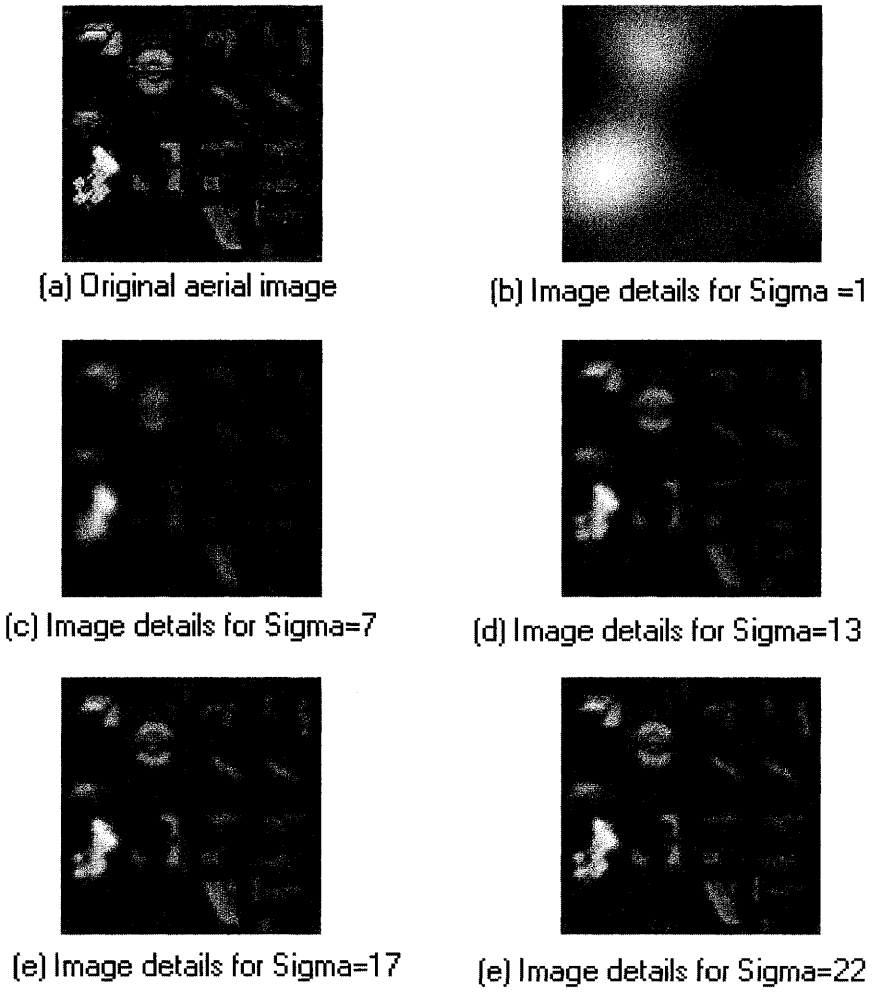

Figure 6.3: Original aerial visible-band image and corresponding image details with different σ

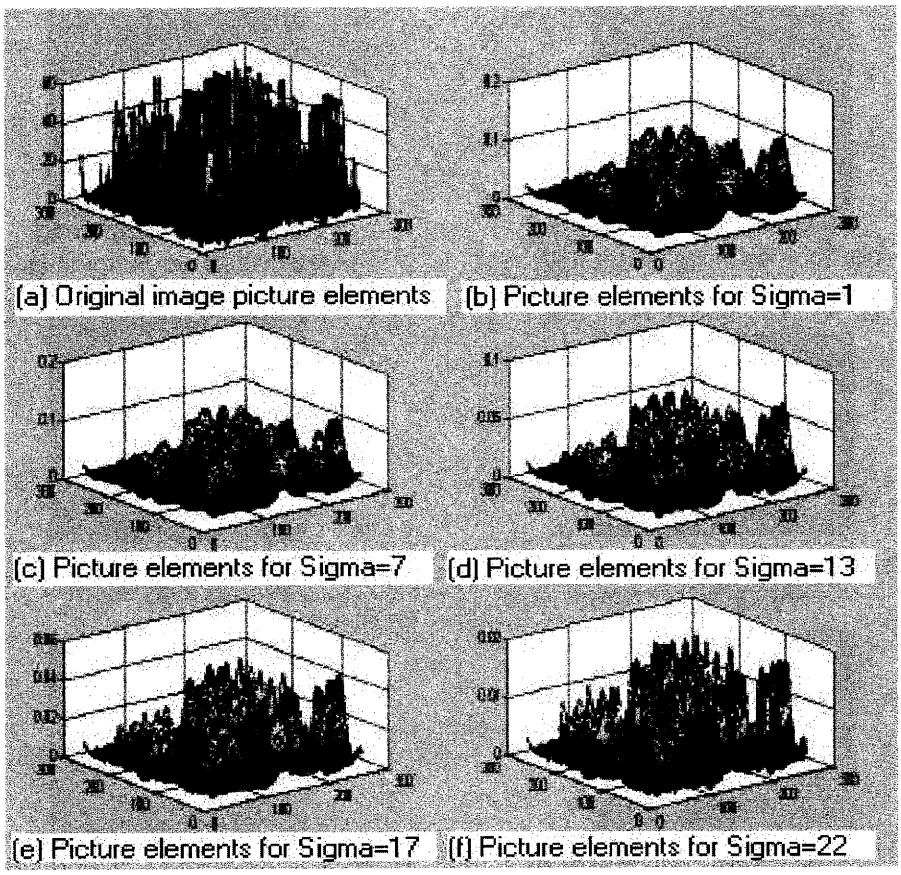

Figure 6.4: Gaussian smoothing with different σ and corresponding picture elements applied to aerial photo image

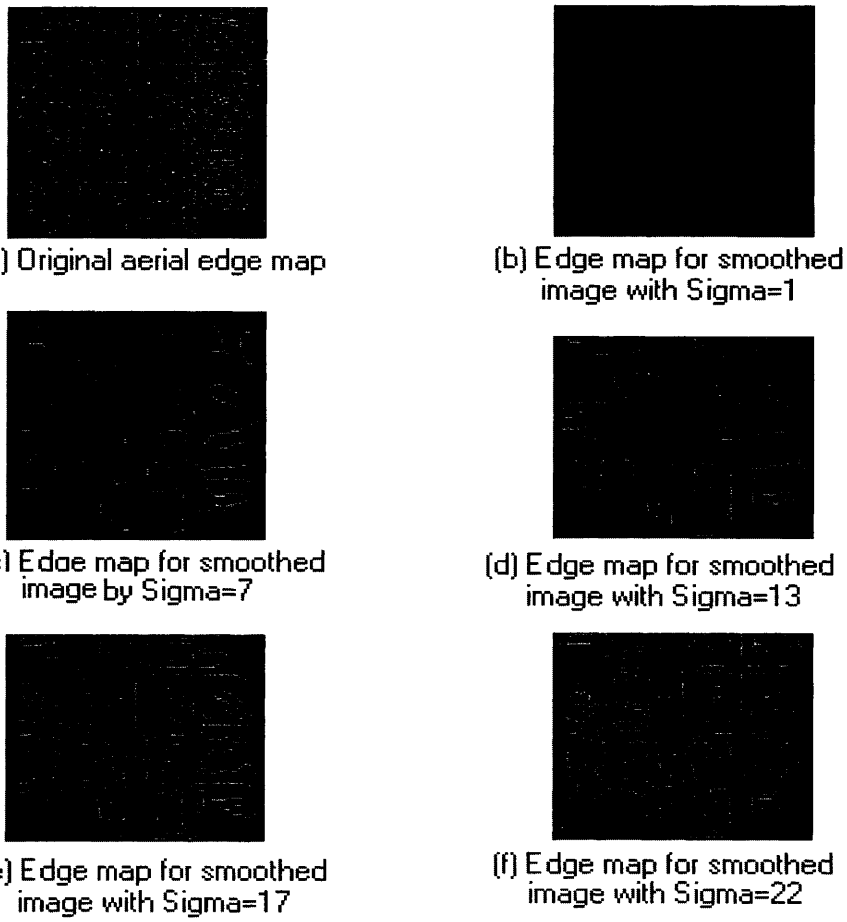

Figure 6.5: Edge map of original aerial visible-band image and corresponding edge maps of images of different Gaussian σ

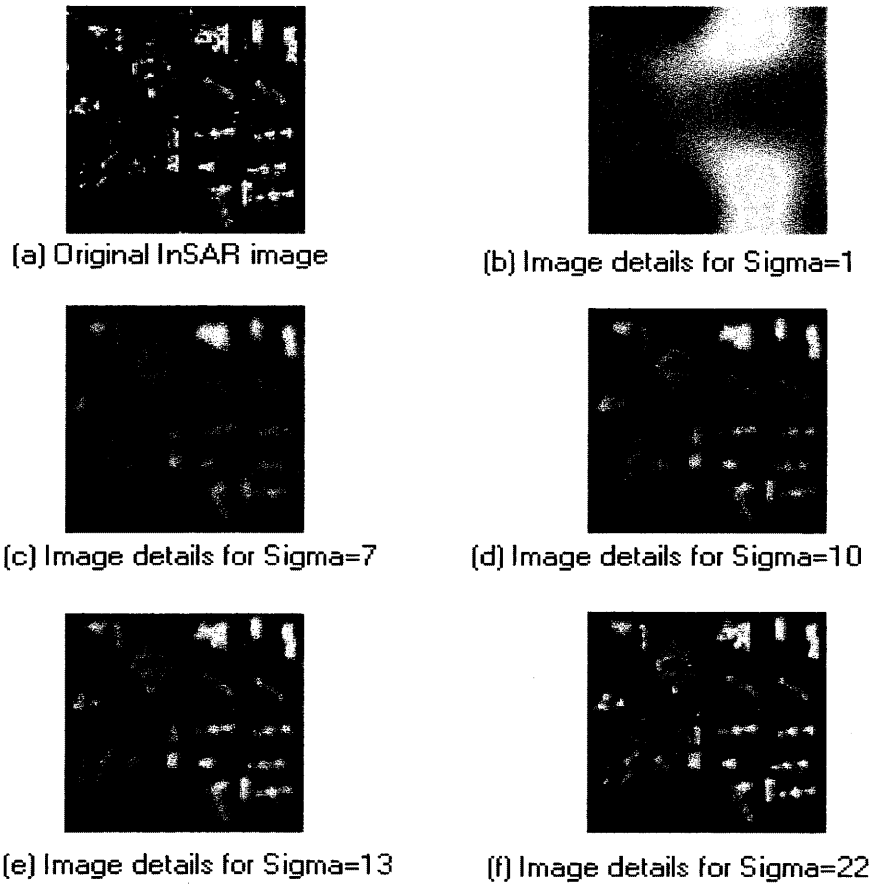

Figure 6.6: Original aerial InSAR image and corresponding image details with different Gaussian σ

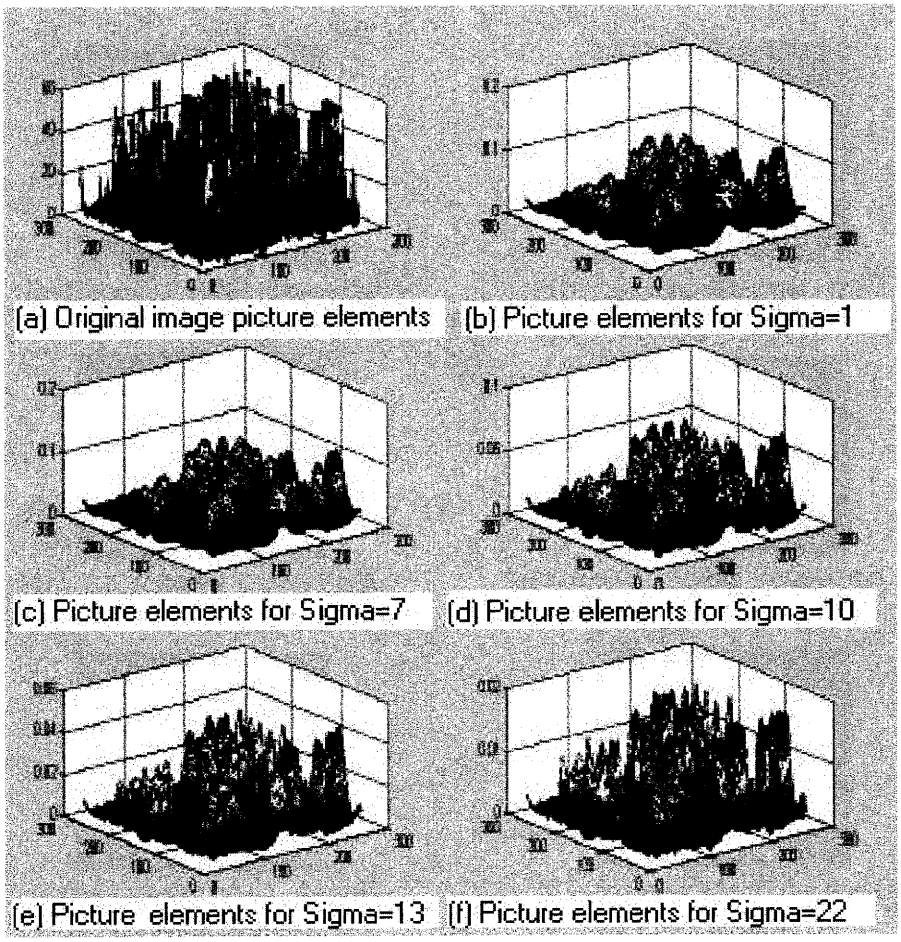

Figure 6.7: Gaussian smoothing with different σ and corresponding picture elements applied to aerial InSAR image

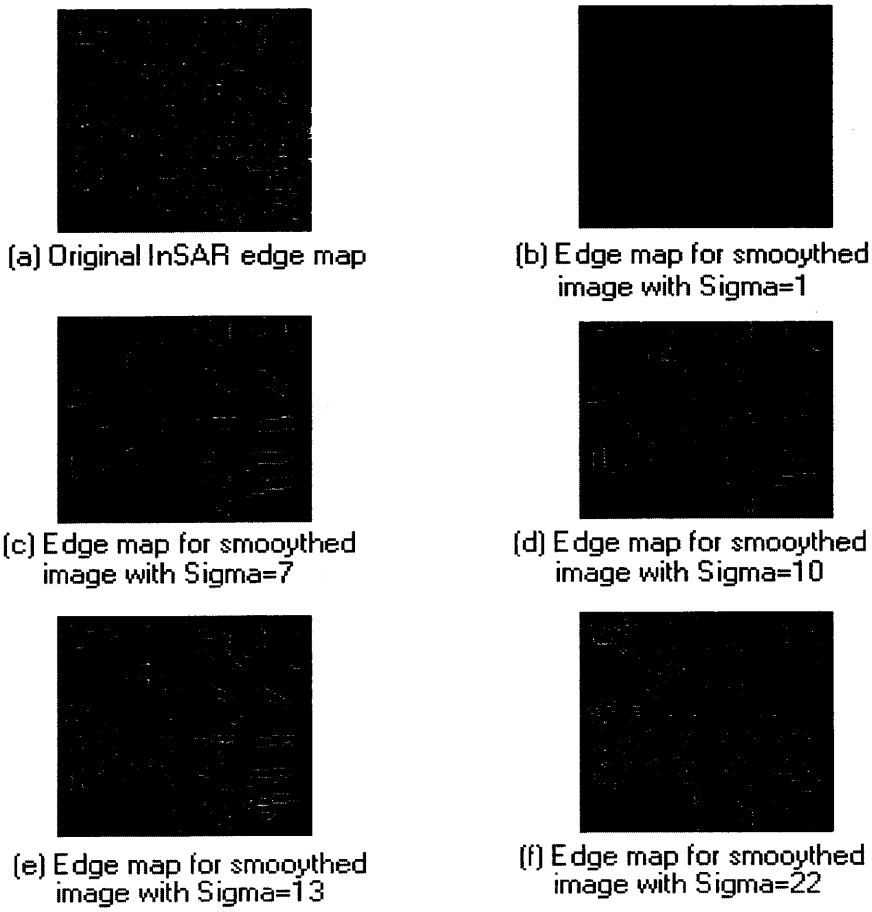

Figure 6.8: Edge map of original aerial InSAR image and corresponding edge maps of images of different Gaussian σ

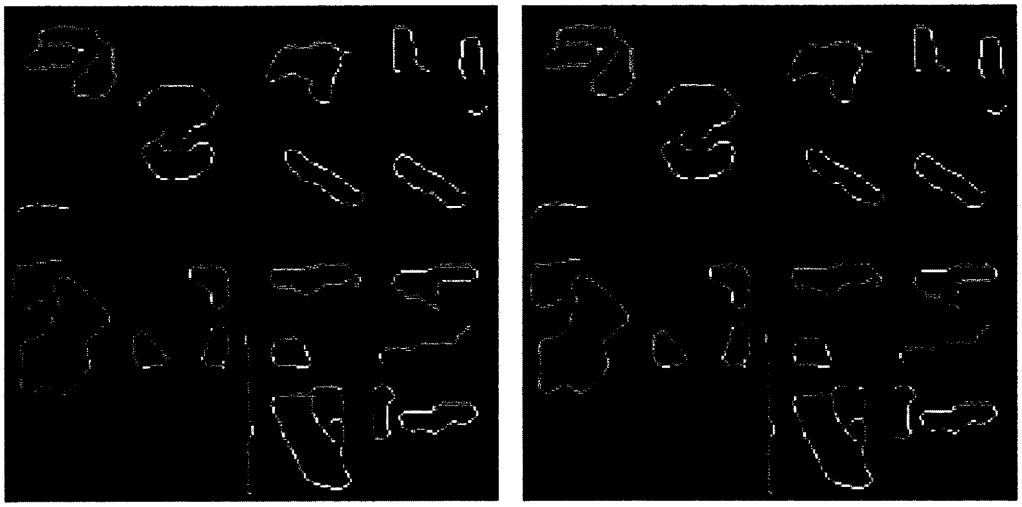

(a)aerial edge map windows (b)InSAR edge map windows

Figure 6.9: Edge maps partitioned into equally sized windows

The moment of order (p+q) of a discrete function $f(x, y)$ is defined as

$$m_{pq} = \sum x^p y^q f(x, y) \qquad p, q = 0, 1, 2, ..., \infty \tag{6.1}$$

where the summation is over a domain that includes all the nonzero values of the function. The central moments are translation invariant moments and can defined by

$$\mu_{pq} = \sum (x - \overline{x})^p (y - \overline{y})^q \quad f(x, y). \tag{6.2}$$

The normalized central moment of order (p+q) can be calculated by dividing the central moment of the same order by a normalization factor. Normalized central moments are scale and translation invariant. The normalization factor is a function

of p and q such that,

$$\eta_{pq} = \frac{\mu_{pq}}{\mu_{00}^{\gamma}} \tag{6.3}$$

where $\gamma = 1 + \frac{p+q}{2}$

The seven Hu invariant moments to scale, translation and rotation are defined as follows:

$$I_1 = \eta_{20} + \eta_{02}$$

$$I_2 = (\eta_{20} - \eta_{02})^2 + 4\eta_{11}^2$$

$$I_3 = (\eta_{30} - 3\eta_{12})^2 + (3\eta_{21} - \eta_{03})^2$$

$$I_4 = (\eta_{30} - + \eta_{12})^2 + (3\eta_{21} + \eta_{03})^2$$

$$I_5 = (\eta_{30} - 3\eta_{12})(\eta_{30} + \eta_{12})[(\eta_{30} + \eta_{12})^2 - 3(\eta_{21} + \eta_{03})^2] + (3\eta_{21} - \eta_{03})(\eta_{21} + \eta_{03})[3(\eta_{30} + \eta_{12}) - (\eta_{21} + \eta_{03})^2]$$

$$I_6 = (\eta_{20} - \eta_{02})[(\eta_{30} + \eta_{12})^2 - (\eta_{21} + \eta_{03})^2 + 4\eta_{11}(\eta_{30} + \eta_{12})(\eta_{21} + \eta_{03})]$$

Finally the skew invariant moment is

$$I_7 = (3\eta_{21} - \eta_{03})(\eta_{30} + \eta_{12})[(\eta_{30} + \eta_{12})^2 - 3(\eta_{21} + \eta_{03})^2] + (\eta_{30} - 3\eta_{12})$$

$$(\eta_{21} + \eta_{03})[3(\eta_{30} + \eta_{12}) - (\eta_{21} + \eta_{03})^2]$$

6.2.4 GCPs Determination

After the determination of the AIMs for each window in both images, each window in the input image is compared to all the windows in the reference image. The matching process is "pairwise exhaustive"; that is, the process repeats for the second, third and all subsequent windows in image 1 until they have all been matched with the windows in image 2. Two windows are said to be matched when the difference value of their AIMs is minimal. In the situation where a window from image 2 has been matched with two different windows from image 1, the matching value corresponding to the lowest AIM difference is accepted as the correct one. The result is that all the windows in image 1 have been matched, but not necessarily all of the windows in image 2 have been matched. A threshold value is set to obtain high accuracy while selecting the GCPs. The difference between the matched windows AIMs should be below the threshold value which is set to one.

6.3 ARVS Experimental Results

In order to demonstrate the performance of the proposed ARVS technique using AIMs, the following experiment is carried out:

Data

Different image pairs from microwave band and visible-band aerial images used for testing. Aerial photo and InSAR images are used for this purpose. For the regis-

tration purpose, image pairs of size (252x252) pixels have been cut from the full scene images. The images were converted to the frequency domain using the fast fourier transform (FFT).

Feature Extraction

Step one to step four of the ARVS model are applied to both images; and then, AIMs I_1 to I_7 were determined for each image edge map. The experiment parameters were set as follows: the Gaussian smoothing σ for InSAR image that brought the desired details was set to 13 while the obtained suitable σ for the optical image was 17. Each image was divided into 16 windows of size (63x63) pixels.

Matching Scheme

The matching of windows (sub-images) are performed by the minimum difference between the AIMs of the windows. The matching process was controlled by the threshold value which was set to one.

Results

The graphical centroids (mean x and mean y) of the matched edge windows which satisfy the threshold value are considered to be the GCPs. Nine GCPs were automatically obtained. To obtain the registered image, the affine transformation was selected (since the image pair suffer from linear distortions) and cubic resampling method was applied. Figure 6.10 illustrates the application of the ARVS algorithm on aerial InSAR and photo image pair. The InSAR image is registered to the reference photo image. A quantitative evaluation to the ARVS model is given in Table 6.1. The difference in pixels between the registered image and the reference image in X direction is in the range of one pixel and in Y direction is in sub-pixel. The results show the high accuracy of the registration using ARVS technique, consid-

Table 6.1: The Evaluation of the Registration of Aerial Visible-Band and InSAR Images

Aerial photo GCPs		Registered InSAR image GCPs		Error determined in pixels	
X	Y	X	Y	X	Y
4.4425	58.9018	5.9476	58.6985	1.5051	0.2033
68.4724	6.47	69.5212	5.6211	1.0488	0.8489
130.1349	54.6332	131.5774	55.4408	1.4425	0.8076
121.5079	4.8468	122.5622	4.5339	1.0543	0.3129

ering that the images are 1 and 2.5 metre resolution. The registration error might not be due to lack of accuracy of the registration process, rather, there are other reasons that may cause such an error, such as high speckle noise and inaccurate edge location.

One of the registration techniques discussed in Chapter 2 was proposed by Dai [33]. Dai used affine invariant moments to register Landsat TM pairs of images. Dai's technique can not applied to the data sets we deal with for a number of reasons. First, Dai's technique is designed to deal with similar images that have very low noise levels. In our thesis the main objective is to register images obtained from different sensors. InSAR images, one of the image pair used in this thesis, are noisy by nature as explained in chapter 3. Second, Dai extracts closed boundary objects from Landsat image pair which is not a difficult task since the image pair is optical. The ARVS edge extraction step is depending on the sub-image contents whatever represent closed or open boundaries. Finally, Dai used chain code to extract objects which is very noise sensitive method and produces very inaccurate results if used with noisy images. This makes it is difficult for Dai's technique to be applied to InSAR images.

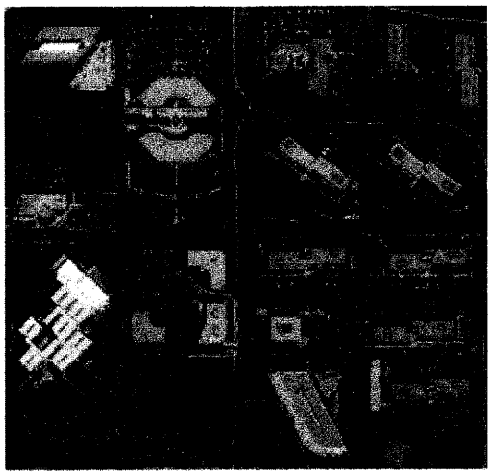

(a)Reference aerial image

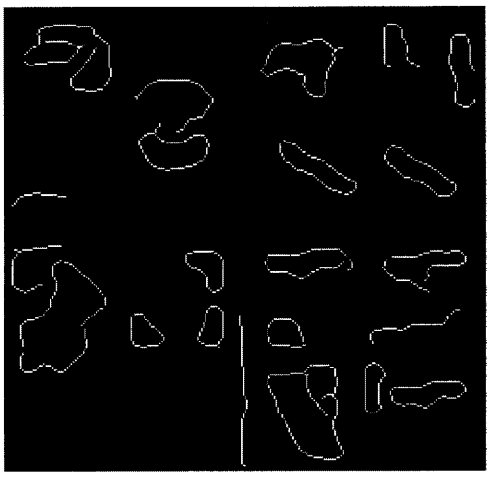

(b)aerial image edge map

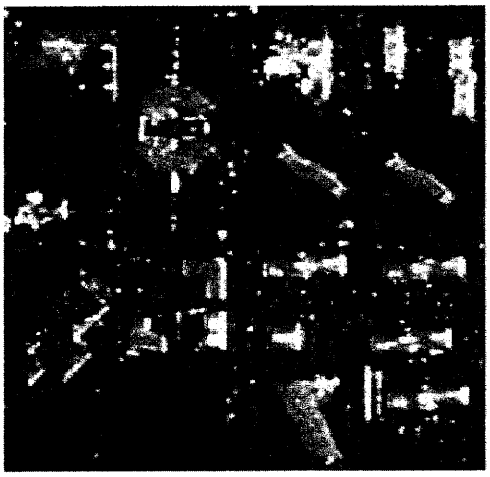

(c)Input InSAR image

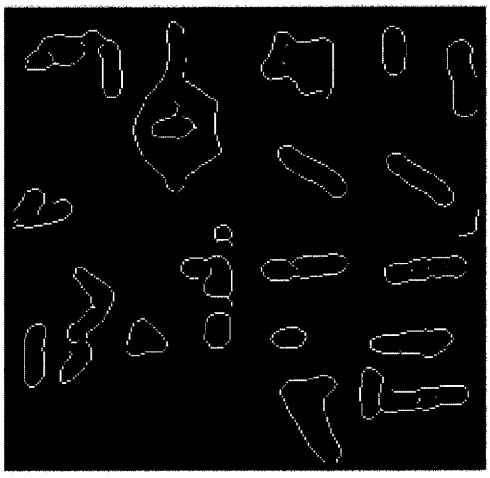

(d)InSAR image edge map

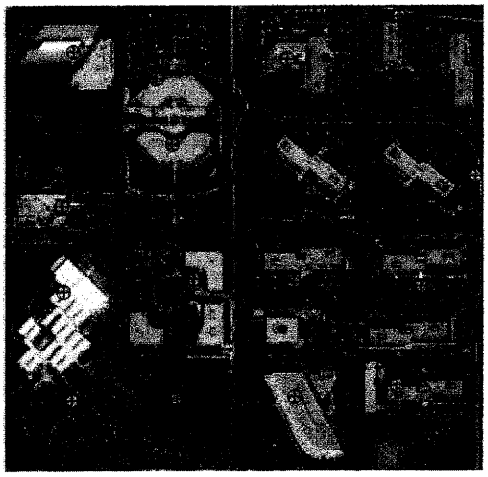

(e)Automated selected GCPs

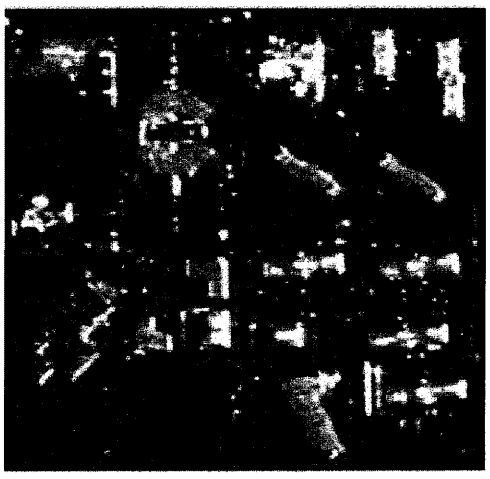

(f)Registered InSAR image

Figure 6.10: Applying ARVS technique on aerial and InSAR images

6.4 Discussion

In this chapter, ARVS technique has been developed to handle the registration of high-resolution aerial InSAR images and visible-band images. High resolution aerial InSAR images are characterized by a low quality of object appearance. To register such images with aerial photos is challenging. No automatic registration technique is known that can be used for automatic registration of InSAR images with other type of images, while ARVS developed technique proves that the possibility of automatic registration.

To overcome the problem that the two images are different in their gray level characteristics, both of them were converted into binary images (edge maps) where it is easier to apply the similarity measure. The developed technique uses the affine invariant moments for the similarity measure between the features of the edge maps. The fact that the affine invariant moments are invariant to translation, rotation, and scaling made for accurate matching results. To enable both images to have a comparable level of detail, a low pass filter was utilized with a preferred σ pixels. Otherwise, it would be difficult to match the objects in the two images. The automatic collected GCPs were applied to the transformation function that led to accurate registration results. The resampling process, as the final operation of image registration, is applied to the input image with the guidance of the affine transformation coefficients to perform the registered image.

Chapter 7

Conclusion

7.1 Summary

This thesis has investigated techniques for automatic image registration of different sensor type remote sensing, in particular, of visible-band images and SAR images. After the two (ARTSO, ARVS) automatic registration techniques are developed, each algorithm is tested by using real remotely sensed images.

The first chapter of this thesis introduced the subject of digital image registration and the importance of remotely sensed image registration and its applications. It is evident that there are difficulties with automatic image registration, especially for different types of sensor images such as RADARSAT and Landsat. As a result, two techniques for automatic image registration are developed. The first technique, ARTSO, is based on extracting and matching objects from an image-pair. It is demonstrated to be successful in automatically registering the given RADARSAT and Landsat images with sub-pixel accuracy for the given data.

The literature review in chapter two has shown that very little work has been done in automatic registration of different sensor remotely sensed images especially RADARSAT and Landsat. Therefore, this thesis is to provide a thorough investigation of some developed techniques for automatic registration with applications to different sensor type remotely sensed images.

Chapter three has presented RADARSAT and Landsat data acquisition and their properties. After the SAR, InSAR and visible-band images were presented, the basic concepts and principles were discussed and different sources of geometric distortions were considered. The preprocessing of SAR images, such as using different speckle reduction filters, are applied to the test data with different kernels. The modified speckle reduction filters are an improvement on the existing Lee, Kuan and Frost filters.

Different existing feature extraction algorithms such as edge detection, thresholding and segmentation are explained and applied to the test data in Chapter four. A new segmentation technique for feature extraction and its application to the test data is discussed. The accuracy of the object extraction process is depending on the accuracy of the edge map. The quality of the extracted edge map from the SAR images is depending on the preprocessing step using speckle reduction filters. While the application of the modified filters do not give much an improved visual results compared to the original speckle reduction filters, it is quantitatively proved that the edge retention and SNR are higher when applying the modified filters. In general this leads to accurate edge map and accurate object extraction. However, for the used SAR images in this thesis, ARTSO patch quality outcome and matching accuracy may not be influenced much when using the speckle reduction filters or

the modified speckle reduction filters. At least the objective of developing speckle reduction filters which could aid the feature extraction process for the feature-based image registration has been achieved.

The object matching procedure and automatic extraction of the GCPs are described in Chapter 5. The experimental results of applying the ARTSO technique to data sets demonstrate the accuracy that automatic registration can achieve.

Chapter six proposed a technique for the automatic image registration of aerial InSAR and aerial photo images using AIMs as the features that can be extracted from both images. After each edge map is divided into rectangular equal windows, the AIMs are determined for each window. Automatic GCPs can be extracted by the comparison of the AIMs of the window edge map of each image and considering the centroid of matched windows as GCPs.

7.2 Thesis Findings and Contributions

The research work described in this thesis has reached a number of important findings and made contributions in the area of the automatic image registration of different types of sensor images.

Comparison to the existing algorithms described in Chapter 2, ARTSO technique has overcome most of the shortcomings shown in Table 2.2. The most of shortcomings concentrated on the performance of feature extraction process. The developed RGCE segmentation process has high ability to extract correct objects from images.

According to Dare technique [34], which is one of the important researches

that dealt with automatic registration of SAR and optical remotely sensed images, ARTSO overcome its shortcomings such that ARTSO does not require manual collection of GCPs for approximate alignment. The object extraction in ARTSO (RGCE) is performed automatically in one step while in Dare technique needs two steps. Registration refinement using edge matching is essential step for Dare registration technique to produce enough and accurate GCPs. This refinement step is to overcome the drawback of the low accuracy of patch extraction step. This step can be excluded from ARTSO technique while produce sub-pixel accuracy. Dare recorded that his technique has 1.5 pixel accuracy while ARTSO achieved sub-pixel accuracy.

This research has:

- Provided a new technique that can be applied to SAR and visible-band remotely sensed images to perform automatic registration with a high accuracy by using a new segmentation technique.

- Proposed an improvement to the existing Lee, Kuan, and Frost speckle reduction filters. The existing idea of replacing the mean algorithm by the median algorithm is applied to original Lee, Kuan, and Frost speckle reduction filters. These improvement filters were tested and found to achieve speckle reduction, while preserving the image details.

- Developed a segmentation technique that facilitates feature extraction from SAR and optical remotely sensed images with accurate object extraction.

- Implemented a technique for the automatic registration of high resolution

interferometric SAR and aerial photos which shows that the GCPs can be automatically extracted from high resolution InSAR and aerial images.

The objectives from this research have achieved. The investigation of automatic registration of microwave and visible band images with different image pairs were presented. However, this area of research requires more research to investigate the automatic image registration of different data sets of visible-band sensors and different SAR sensors combinations. A general procedure for measuring the accuracy of any image registration technique is needed to be investigated. Moreover, the area of developing the optimal SAR speckle reduction filters need an extensive work.

Bibliography

[1] M. Abbasi-Dezfouli and T. Freeman. "Stereo-Image Registration Based on Uniform Patches". *International Archives of Photogrammetry and Remote Sensing*, 30(3):1–8, 1989.

[2] M. Abbasi-Dezfouli and T. Freeman. "Patch Matching in Stereo-Images Based on Shape". *International Archives of Photogrammetry and Remote Sensing*, 30(3):1–8, 1994.

[3] M. Ali and D. Clausi. "A New Automatic Registration Technique for Multi-Sensor Remote Sensing Images". *Proceedings of 2Nd Annual UW Graduate Students Research Conference, Waterloo, Canada*, 1-4 April 2002.

[4] M. Ali and D. Clausi. "Automatic Registration of Visible-Band and InSAR Aerial Remotely Sensed Images (ARVS)". *Proceedings of 3Rd Annual UW Graduate Students Research Conference, Waterloo, Canada*, 2-4 April 2003.

[5] M. Ali and D. Clausi. "Using the Canny Edge Detector for Feature Extraction and Enhancement of Remote Sensing Images". *IEEE, International Geoscience and Remote Sensing Symposium, IGARSS*, 2001.

[6] M. Ali and D. Clausi. "Feature Extraction and Enhancement of Remote Sensing Images". *Proceedings of Geomatics for Informed Decision, GEOIDE, Fredericton, Canada*, 21-22 June,2001.

[7] M. Ali and D. Clausi. "Robust Automatic Registration Technique for Multi-Sensor Remote Sensing Images". *Proceedings of Geomatics for Informed Decision, GEOIDE, Toronto, Canada*, 22-24 May 2002.

[8] M. Ali and D. Clausi. "Automatic Registration of Multisensor Remote Sensing Images". *IEEE, International Geoscience and Remote Sensing Symposium, IGARSS*, 24-28 June 2002.

[9] M. Ali, D. Clausi, and Ed. Jernigan. "Improved Non Linear Speckle Reduction Filters for Synthetic Aperture Radar Images". *Proceedings of 3rd Annual UW Graduate Students Research Conference, Waterloo, Canada*, 2-4 April 2003.

[10] American Society of Photogrammetry and Remote Sensing. "ASPRS Interim Accuracy Standards for Large-Scale Maps". *Photogrammetric Engineering and Remote Sensing*, 55(7):1038–1040, 1989.

[11] J. Astola and P. Kuosmanen. *"Fundamentals of Nonlinear Digital Filtering"*. Boca Raton, Fl: Crc, 1997.

[12] D.H. Ballard and C.M. Brown. *"Computer Vision"*. Prentice–Hall, New Jersey, 1982.

[13] M. Barbieri, R. Biasutti, and G. Calabresi. "Monitoring the Summer 1997

Floods in North-Eastern Europe Through Earth Watching". *Earth Observation Quarterly*, 56-57:6–13, 1997.

[14] H. G. Barrow and R. J. Popplestone. "Relational Description in Picture Processing". *Machine Intelligence*, 6:377–396, 1971.

[15] V. Berzins. "Accuracy of Laplacian Edge Detector". *Computer Vision, Graphics, and Image Processing*, 27:195–210, 1984.

[16] D. Boardman, I. Dowman, A. Chamberlain, D. Fritsch, and W. Newton. "An Automated Image Registration System for SPOT Data". *International Archives of Photogrammetry and Remote Sensing*, 31(4):128–133, 1996.

[17] A. C. Bovik, T. S. Huang, and D. C. Munson. "A Generalization of Median Filtering Using Linear Combinations of Order Statistics". *IEEE Transactions on Acoustics, Speeck and Signal Processing*, ASSP-31(6):1342–1350, 1983.

[18] L. G Brown. "A Survey of Image Registration Techniques". *ACM Computer Surveys*, 24(4):325–376, 1992.

[19] A. Buongiorno, O. Arino, C. Zehner, P. Colagrande, and P. Goryl. "ERS-2 Monitors Exceptional Fire Event in South-East Asia". *Earth Observation Quarterly*, 56-57:1–5, 1997.

[20] P. Burrough. *"Principles of Geographical Information Systems for Land Resources Assessment"*, page 193. Oxford University Press, 1986.

[21] Caesar. "Caesar SAR Image Processing Toolset User Guide". 2.4a, N. A.:70, 1996.

[22] Canadian Space Agency. "http://www.espace.gc.ca/asc/eng/default.asp".

[23] J. Canny. "A Computational Approach to Edge Detection". *IEEE Transactions on Pattern Analysis and Machine Intelligence*, PAMI-8(6):679–698, 1986.

[24] J. F. Canny. "A Computational Approach to Edge Detection". *IEEE Trans. Pattern Analysis and Machine Intelligence*, 8:679–698, 1986.

[25] E. De Castro and C. Morandi. "Registration of Translated and Rotated Images Using Finite Fourier Transforms ". *IEEE Transactions on Pattern Analysis and Machine Intelligence*, 9(5):700–703, 1987.

[26] Hsi-Min Chao and John C. Trinder. "Feature Extraction in Residential Areas By Knowledge Modelling" *Http://www.Gisdevelopment.Net/Aars/Acrs/2000/Ts9/Imgp0016.Shtml*, 2000.

[27] R. Cook, I. Mcconnell, C. Oliver, and Welbourne E. "MUM (Merge Using Moments) Segmentation for SAR Images". *SAR Data Processing for Remote Sensing*, SPIE 2316:92–103, 1994.

[28] T. R. Crimmins. "Geometric Filter for Reducing Speckle". *Optical Engineering*, 25(5):651–654, 1986.

[29] R. F. Cromp and W. J. Campbell. "Data Mining of Multidimensional Remotely Sensed Images". *2nd Int. Conference of Information Knowledge Management, Washington, Dc*, pages 471–480, 1993.

[30] J. Curlander, R. Kwok, and S. Pang. "A Post Processing System for Automated Rectification and Registration of Spaceborne SAR Imagery". *International Journal of Remote Sensing*, 8(4):621–638, 1987.

[31] J. C. Curlander and R. N. Mcdonough. *"Synthetic Aperture Radar, Systems and Signal Processing"*. John Wiley and Sons, New York, 1990.

[32] X. Dai and S. Khorram. "Development of a Feature-Based Approach to Automated Image Registration of Multisensor and Multitemporal Remotely Sensed Imagery". *IEEE Geoscience and Remote Sensing Symp.(IGARSS), Singapore*, pages 243–245, 1997.

[33] X. Dai and S. Khorram. "A Feature-Based Image Registration Algorithm Using Improved Chain Code Representation Combined with Invariant Moments". *IEEE Transactions on Geoscience and Remote Sensing*, 37(5):2351–2362, 1999.

[34] P. M. Dare. "New Techniques for the Automatic Registration of Microwave and Optical Remotely Sensed Images". *Ph.D. Thesis, University of London*, 1999.

[35] P. M. Dare and I. J. Dowman. "Automated Procedures for Multi-Sensor Registration and Orthorectification of Satellite Images". *International Archives of Photogrammetry and Remote Sensing, IGARSS, Hawaii,*, 32(7-4-3 W6):37–44, 1999.

[36] P. M. Dare and I. J. Dowman. "Automatic registration of SAR and optical imagery based on multiple feature extraction and matching". *IEEE, Interna-*

tional Geoscience and Remote Sensing Symposium, IGARSS, Hawaii,, 24-28 July 2000.

[37] L. S. Davis and A. Rosenfeld. "Noise Cleaning By Iterated Local Averaging". *IEEE Transactions on Systems, Man and Cybernetics*, SMC-8:705–710, 1978.

[38] T. Day and J. P. Muller. "DEM Production By Stereo Matching SPOT Image Pairs: A Comparison of Algorithms". *Image and Vision Computing*, 7(2):95–101, 1989.

[39] R. Devore, W.l Shao, J. Pierce, E. Kaymaz, B.-T. Lerner, and W. Campbell. "Using Non-Linear Wavelet Compression to Enhance Image Registration". *Wavelet Applications IV*, SPIE 3078:539–551, 1997.

[40] J.-P. Djamdji, A. Bijaoui, and R. Maniere. "Geometric Registration of Images: the Multi-Resolution Approach". *Photogrammetric Engineering and Remote Sensing*, 59(5):645–653, 1993.

[41] I. Dowman. "Automated Procedures for Integration of Satellite Images and Map Data for Change Detection: the Archangel Project". *International Archives of Photogrammetry and Remote Sensing*, 32(4):162–169, 1998.

[42] I. Dowman, Twu Z.-G., and P.-H. Chen. *"DEM Generation from Stereoscopic SAR"*. Canadian National Defense, 1997. Cd-Rom.

[43] I. J. Dowman, D. Boardman, and W. Newton. "A System for Automatic Registration of Two SPOT Images". volume 704, pages 169–175, Durham, 1996.

[44] R. O. Duda and P. E. Hart. *"Pattern Classification and Scene Analysis"*. Johan Wiley and Sons, New York, 1973.

[45] European Commission. *"Technical Specifications for Remote Sensing Control of Surface Subsidized Arable and Forage Areas"*. European Commission, Brussels, 1997.

[46] A. N. Evans and M. S. Nixon. "Speckle Filtering in Ultrasound Images for Feature Extraction". *Acoustic Sensing and Imaging, Conference Publication No. 369*, 1993.

[47] J. Flusser. "An Adaptive Method for Image Registration". *Pattern Recognition*, 25(1):45–54, 1992.

[48] J. Flusser and Suk T. "A Moment Based Approach to Registration of Images with Affine Geometric Distortion". *IEEE Transactions on Geoscience and Remote Sensing*, 32(2):382–387, 1994.

[49] L. Fonseca, B. Manjunath, and C. Kenney. "Automatic Registration of Satellite Imagery". volume 366, pages 13–27, Nasa Goddard Space Flight Center, Maryland, 1997.

[50] L. Fonseca and B. S. Manjunath. "Registration Techniques for Multisensor Remotely Sensed Imagery". *Photogrammetric Engineering and Remote Sensing*, 62(9):1049–1056, 1996.

[51] L. Fonseca and B. S. Manjunath. "Registration Techniques for Multisen-

sor Sensed Imagery". *Photogrammatic Engineering and Remote Sensing*, 62(9):1049–1056, 1996.

[52] H. Freeman. *"Boundary Encoding and Processing"*, pages 241–266. Academic Press, New York, 1961.

[53] H. Freeman. *"Gonzalez, R. C. and R. E. Woods"*, page 716. Addison-Wesley, Reading, Massachusetts, 1992.

[54] V. S. Frost, J. A. Stiles, K. S. Shanmugan, and Holtzman J. C. "A Model for Radar Images and Its Application to Adaptive Digital Filtering of Multiplicative Noise". *IEEE Transactions on Pattern Analysis and Machine Intelligence*, PAMI-4(2):157–165, 1982.

[55] W. Frstner and E. GLch. "A Fast Operator for Detection and Precise Location of Distinct Points, Corners and Centres of Circular Features". volume 437, pages 281–305, Interlaken, 1987.

[56] A Goshtasby. "Registration of Images with Geometric Distortions". *IEEE Transactions on Geoscience and Remote Sensing*, 26(1):60–64, 1988.

[57] J. Gredel and H. Schrter. "Dfd Data Product Guide", 1997. Dlr.

[58] D. Gugan. "Practical Aspects of Topographic Mapping from SPOT Imagery". *Photogrammetric Record*, 12(69):349–355, 1987.

[59] D. Gugan and I. Dowman. "Accuracy and Completeness of Topographic Mapping from SPOT Imagery". *Photogrammetric Record*, 12(72):787–796, 1988.

[60] B. Gunilla. "Hierarchical Chamfer Matching: A Parametric Edge Matching Algorithm". *IEEE Transactions on Pattern Analysis and Machine Intelligence*, PAMI10(6):849–865, 1988.

[61] A. De Haan. "Contribution of the 'Politecnico Di Milano' to the Oeepe Test on Triangulation with SPOT Data". *Oeepe Official Publication*, 26:93–107, 1991.

[62] R. M. Haralick and L. G. Shapiro. "Image Segmentation Techniques". *CVGIP*, 29(1):100–132, 1985.

[63] R.M. Haralick and L.G. Shapiro. *"Computer and Robot Vision"*. Addison-Wesley, 1992.

[64] R Harris. "Trends in Remote Sensing". volume 129, pages 5–6, 1997.

[65] C. Heipke. "Automation of Interior, Relative and Absolute Orientation". *ISPRS Journal of Photogrammetry and Remote Sensing*, 52:1–19, 1997.

[66] F. Henderson and A. Lewis. *"Principles and Applications of Imaging Radar"*, page 866. John Wiley and Sons, New York, 1998.

[67] P. V. C. Hough. "Methods and Means for Recognizing Complex Patterns". *U.S. Patent 3 069*, 654, 1962.

[68] M-K. Hu. "Visual Pattern Recognition By Moment Invariants". *IRE Trans. on Information Theory*, IT-8:179–187, 1962.

[69] M. Irani and S. Peleg. "Improving Resolution by Image Registration". *Computer . Vision, Graphics Image Processing*, 53(3):213–239, 1991.

[70] John R. Jensen. *"Principles of Geographical Information Systems for Land Resources Assessment"*, page 544. Prentice Hall; 2nd Edition, 2000.

[71] R. Jha and M. E. Jernigan. "Edge Adaptive Filtering: How Much and Which Direction". *Proceedings of IEEE International Conference on Systems, Man, and Cybernetics*, pages 364–366, 1989.

[72] L. Kai and J.-P. Muller. "Segmenting Satellite Imagery: A Region Growing Scheme".

[73] J. N. Kapur, P. K. Sahoo, and A. K. C. Wong. "A New Method for Gray-Level Picture Thresholding Using the Entropy of the Histogram". *Computer Vision, Graphics, and Image Processing*, 29:273–285, 1985.

[74] D. T. Kuan, A. A. Sawchuk, T. C. Strand, and P. Chavel. "Adaptive Noise Smoothing Filter for Images with Signal Dependent Noise". *IEEE Transactions on Pattern Analysis and Machine Intelligence*, PAMI-7(2):165–177, 1985.

[75] D. T. Kuan, A. A. Sawchuk, T. C. Strand, and P. Chavel. "Adaptive Restoration of Images with Speckle". *IEEE Transactions on Acoustics, Speech and Signal Processing*, ASSP-35(3):373–382, 1987.

[76] J. S. Lee. "Speckle Analysis and Smoothing of SAR Images". *Computer Graphics and Image Processing*, 17:24–32, 1981.

[77] J. S. Lee. "A Simple Speckle Smoothing Algorithm for SAR Images". *IEEE Transactions on Systems, Man and Cybernetics*, SMC-13(1):85–59, 1983.

[78] J. S Lee. "Speckle Suppression and Analysis for Synthetic Aperture Radar". *Optical Engineering*, 25(5):636–643, 1986.

[79] Jong-Sen Lee and K.P. Papathanassiou. "A New Technique for Noise Filtering of SAR Interferometric Phase Images". *IEEE, Transaction on Geoscience and Remote Sensing*, 36(5):1456–1465, 1998.

[80] Y. H. Lee and S. A. Kassam. "Generalized Median Filtering and Related Nonlinear Filtering Techniques". *IEEE Transactions on Acoustics, Speeck and Signal Processing*, ASSP-33(3):672–683, 1985.

[81] Henry Li and Yi-Tong Zhou. "Automatic Visual/IR Image Registration". *Optical Engineering*, 35(2):391–400, 1996.

[82] J. S. Lim. *"Two Dimensional Signal and Image Processing"*. Prentice Hall, Englewood Cliffs, New Jersey, 1990.

[83] A. Lopes, R. T ouzi, and E. Nesby. "Adaptive Speckle Filter and Scene Heterogeneity". *IEEE Transactions on Geoscience and Remote Sensing*, 28):992–1000, 1987.

[84] T. Loupas, Mcdicken W. N., and Allan P. L. "An Adaptive Weighted Median Filter for Speckle Suppression in Medical Ultrasonic Images". *IEEE Transactions on Circuits and Systems*, 36(1):129–135, 1989.

[85] B.D. Lucas and T. Kanade. "An Iterative Image Registration Technique with an Application to Stereo Vision". *Proceedings of Imaging Understanding Workshop*, pages 121–130, 1981.

[86] Li Manjunath and S. K. Mitra. "A Contour Based Approach to Multisensor Image Registration". *IEEE Transactions on Image Processing*, 4(3):320–334, 1995.

[87] D. Marr and E. Hildreth. "Theory of Edge Detection". volume B207, pages 187–217, 1980.

[88] D. Massonet. "Satellite Radar Interferometry". *Scientific American*, pages 32–39, 1997.

[89] I. Mcconnell and C. Oliver. "Comparison of Annealing and Iterated Filters for Speckle Reduction in SAR". *Microwave Sensing and Synthetic Aperture Radar*, SPIE 2958:74–85, 1996.

[90] N. Mcfarlane and M. Thomas. "Speckle Reduction Algorithms and Application to SAR Images". *Proceedings of the Annual Conference of the Remote Sensing Society, Reading*, 449:391–398, 1984.

[91] C. Mcglone. "Sensor Modelling in Image Registration". pages 110–127, Washington Dc, 1994.

[92] A. Morgado and I. Dowman. "A Procedure for Automatic Absolute Orientation Using Aerial Photographs and a Map". *ISPRS Journal of Photogrammetry and Remote Sensing*, 52:169–182, 1997.

[93] P. Mueller and R. Hoffer. "Low Pass Spatial Filtering of Satellite Radar Data". *Photogrammetric Engineering and Remote Sensing*, 55(6):887–895, 1989.

[94] M. Nagao and T. Matsuyama. "Edge Preserving Smoothing". *Computer Graphics and Image Processing*, 9:394–407, 1979.

[95] Rao P. V. Narasimha, M. S. S. R. Vidyadhar, Rao T. Ch. Malleswara, and Venkataratnam L. "An Adaptive Filter for Speckle Suppression in Synthetic Aperture Radar Images". *International Journal of Remote Sensing*, 16(5):877–889, 1995.

[96] National Aeronautics and Space Administration "http://www.nasa.gov/home/index.html".

[97] W. Newton, C. Gurney, D. Sloggett, and I. Dowman. "An Approach to the Automatic Identification of Forests and Forest Change in Remotely Sensed Images". *International Archives of Photogrammetry and Remote Sensing*, 30(3):607–614, 1994.

[98] C. Oliver, D. Blacknell, I. Mcconnell, and R. White. "Optimum Edge Detection in SAR". *Synthetic Aperture Radar and Passive Microwave Sensing*, SPIE 2584:152–163, 1995.

[99] F. Orti. "Optimal Distribution of Tie Points to Minimize Landsat Image Registration Errors". *Photogrammetric Engineering and Remote Sensing*, 47:101–110, 1981.

[100] G. Otto and T. Chau. "A Region Growing Algorithm for Matching Terrain Image". *Image and Vision Computing*, 7(2):83–94, 1989.

[101] F. G. Peet. "The Use of Invariants in the Transformation and Registration of Images". *The Canadian Surveyor*, 29(5):501–506, 1975.

[102] I. Pitas and A. N. Venetsanopoulos. *"Nonlinear Digital Filters, Principles and Applications"*. Kluwer Academic Publishers, Boston, 1990.

[103] C. Pohl and Genderen J. L. Van. "Multisensor Image Fusion in Remote Sensing: Concepts, Methods and Applications". *International Journal of Remote Sensing*, 19(5):823–854, 1998.

[104] W. K. Pratt. *"Digital Image Processing, 2nd Edition"*, page 698. John Wiley and Sons, New York, 1991.

[105] N. Prechtel and O. Bringmann. "Near Real Time Road Extraction from Satellite Images Using Vector Reference Data". *International Archives of Photogrammetry and Remote Sensing*, 32(2):229–234, 1988.

[106] J. M. S. Prewitt. *"Picture Processing and Psychpictorics"*. Academic Press, New York, 1970.

[107] G. M. Qu'Enot. "Image Matching Using Dynamic Programming: Application to Stereovision and Image Interpolation". *Communication, Bordeaux, France*, 1996.

[108] L. Renouard and F. Perlant. "Geocoding SPOT Products with Ers-1 Geometry". pages 653–658, Hamburg, 1993.

[109] J. A. Richards. *"Remote Sensing Digital Image Analysis"*. Springer-Verlag, 1986.

[110] E. Rigno, R. Kwok, J. Curlander, and S. Pang. "Automated Multisensor Registration: Requirements and Techniques". *Photogrammetric Engineering and Remote Sensing*, 57(8):1029–1038, 1991.

[111] R. Rogers and L. Wood. "The History and Status of Merging Multiple Sensor Data: an Overview". *Image Processing and Remote Sensing, ACSM- Annual Convention*, 4:352–360, 1990.

[112] A. Rosenfeld. *"Picture Processing By Computer"*. Academic Press, New York, 1969.

[113] R. Ruskon and I. Dowman. "Segmentation Design for an Automatic Multisource Registration". *Integrating Photogrammetric Techniques with Scene Analysis and Machine Vision III*, SPIE 3072:307–317, 1997.

[114] P.K. Sahoo, S. Soltani, and A.K.C. Wong. "A Survey of Thresholding Techniques". *Computer Vision, Graphics, and Image Processing*, 41:233–260, 1988.

[115] A. Sanfeliu and K. S. Fu. "A Distance Measure Between Attributed Relational Graphs for Pattern Recognition". *IEEE Transaction on Systems, Man and Cybernetics*, 13(3):353–362, 1983.

[116] M. Satter and A. Goshtasby. "Registration of Deformed Images". pages 221–231, Nasa Goddard Space Flight Center, Maryland, 1997.

[117] A. Schistad-Solberg, A. Jain, and T. Taxt. "Multisource Classification of

Remotely Sensed Data: Fusion of Landsat TM and SAR Images". *IEEE Transactions on Geoscience and Remote Sensing*, 32(4):768–778, 1994.

[118] Robert A. t Schowengerd. *"Remote Sensing, Models and Methods for Image Processing"*. 1997.

[119] R. A. Schowengerdt. *"Remote Sensing, 2nd Eddition"*. Academic, San Diego, 1997.

[120] G. Schrier. *"SAR Geocoding: Data and Systems"*. Karlsruhe, Germany, 1993.

[121] L. G. Shapiro and R. M. Haralick. "Structural Descriptions and Inexact Matching". *IEEE Transactions on Pattern Analysis and Machine Intelligence*, PAMI-3(5):505–519, 1981.

[122] A. Sowter. "The Automatic Extraction of DEM Data from Stereo RADARSAT Pairs Over the Tropics". *International Archives of Photogrammetry and Remote Sensing*, 32(2):291–298, 1998.

[123] G. Stockman, S. Kopstein, and S. Benett. "Matching Images to Models for Registration and Object Detection Via Clustering". *IEEE Transactions on Pattern Analysis and Machine Intelligence*, 4(3):229–241, 1982.

[124] G. Stockman and C. Page. "A Region Based Approach to Digital Image Registration with Subpixel Accuracy". *IEEE Transactions on Geoscience and Remote Sensing*, 24(3):390–399, 1986.

[125] R. Suoranta and K. P. Estola. "Robust Median Filter with Adaptive Win-

dow Length". *Proceedings of IEEE International Conference on Circuits and Systems*, 1991.

[126] D. Toll. "Analysis of Digital Landsat MSS and Seasat SAR Data for Use in Discriminating Landcover At the Urban Fringe of Denver, Colorado". *International Journal of Remote Sensing*, 6(7):1209–1229, 1985.

[127] T. Toutin. "IntGration Des DonnEs Multisources: Comparison De Methodes GeomTriques et RadiomTriques". *International Journal of Remote Sensing*, 16(15):2795–2811, 1995.

[128] R. Touzi, A. Lopes, and P. Bousquet. "A Statistical and Geometrical Edge Detector for SAR Images". *IEEE Trans. Geoscience and Remote Sensing*, 26:764–773, 1988.

[129] Y. Tseng, J. Tzen, K. Tang, and S. Lin. "Image to Image Registration by Matching Area Features Using Fourier Descriptors and Neural Networks". *Photogrammetric Engineering and Remote Sensing*, 63(8):975–983, 1997.

[130] F.T. Ulaby, R. Moore, and A. Fang. Khorram. "In Microwave Remote Sensing: Active and Passive". *Artech House, Dedham, Mass*, 3:1848–1892, 1986B.

[131] A. Ventura, A. Rampini, and R. Schettini. "Image Registration By Recognition of Corresponding Structures". *IEEE Transactions on Geoscience and Remote Sensing*, 28(3):305–314, 1990.

[132] V. Vohra and I. Dowman. "Automated Extraction of Large Buildings from

High Resolution Satellite Images for Registration with a Map". *International Archives of Photogrammetry and Remote Sensing*, 31(3):903–908, 1996.

[133] V. Vohra and I. Dowman. "Automatic Extraction of Significant Features from High Resolution Satellite Images for Registration with a Map". volume 126, pages 23–29, London, 1997.

[134] P. D. Wendt, E. J. Coyle, and N. C. Gallagher. "Stack Filters". *IEEE Trans. Acoust., Speech, Signal Processing*, ASSP-34:898–919, 1986.

[135] T. Westin. "Precision Rectification of SPOT Imagery". *Photogrammetric Engineering and Remote Sensing*, 55(3):311–316, 1990.

[136] J. Weszka. "A Survey of Threshold Selection Techniques". *Computer Graphics and Image Processing*, 7:259–265, 1978.

[137] R. White. "Change Detection in SAR Imagery". *International Journal of Remote Sensing*, 12(2):339–360, 1991.

[138] P. Wolf. *"Elements of Photogrammetry 2nd Edition"*. Mcgraw-Hill, New York, 1983.

[139] R. Y. Wong. "Sensor Transformations". *IEEE Transactions on Syst. Man Cybernetzes*, SMC-7(12):836–840, 1977.

[140] D. Yuan, C. D. Elvidge, J. G. Lyon, and R. S. Lunetta. "North America Land Cover Change Detection Using Historical MSS Data: Three Pilot Studies". *In Proc. Eco Rio'94, Int. Symp. Resource and Environmental Monitoring, Rio De Janeiro, Brazil*, 1994.

[141] Q. Zheng and R. Chellappa. "A Computational Vision Approach to Image Registration". *IEEE Trans. on Image Processing*, 1993.